Structural analysis of the Jebel Fadeloun anticline, Tunisia: Impact of fractures and faults on the petrophysical properties of carbonate rocks

Master Thesis in Petroleum/Structural Geology

Fredrik Sebastian Kjelkenes

Department of Earth Science

University of Bergen

June, 2015

ABSTRACT

Recognizing the structure, evolution and fluid flow within the earth's crust is a critical issue for both academic and applied geoscience. This study presents structural analysis of an anticline, which aim is to elucidate the **(1)** structure and evolution of the fold, as well as the associated faults and fractures, **(2)** to better investigate how tectonics have impacted the microstructural character of the host rock, and **(3)** to discuss possible implications for petrophysical properties and fluid flow in carbonate reservoir rocks.

The topography and geology of northern Tunisia bears a strong imprint of the Atlassic/Alpine collision between Eurasia and Africa, which resulted in the formation of a series of NE-SW trending elongate mountains and basins across the region. A complex tectonic history in Pre-Atlassic times, involving elements of compression, rifting, inversion, strike-slip, vulcanisme and diapirism, also contributes to a complex present-day structural framework. The front of the Tunisian Atlas Mountain Belt ends into a relatively undeformed and stable geological region, known as the Pelagian Province, which comprises the areas of eastern Tunisia, northwestern Libya and extends to offshore Malta and Italy. The study area is located in the boundary between these two geological regions.

For the structural and petrophysical characterization of the host rocks and fault rocks in the study area, a variety of methods were used, including i) field mapping and structural cross-sections, ii) outcrop analysis (e.g. fracture density scanlines), iii) thin section analysis, iv) in-situ mechanical strength measurements using a rebound hammer, v) seismic interpretation.

This study investigates the structure and evolution of the Jebel Fadeloun anticline, which is located in northeastern Tunisia, near the Gulf of Hammamet. Jebel Fadeloun is a 350 m high hill, formed by a NE-SW trending anticline. The core of the fold uncovers Aptian Limestone. Moving away from the centre, the lithologies, which all pre-date folding, comprise alternating units of limestone and marl, and show youngest formation of Eocene age. Several sets of faults dissect the fold, showing offsets within seismic resolution. Calcite growth and striations in the fault slip planes, indicate dominant normal sense of displacement, occasionally with a component of strike-slip. Fault analyses reveal that fracture frequencies and fault rocks are heterogeneously distributed within the fault zones. Deformed rocks display a variety of microtectonic structures, including brecciation, fracturing, calcite twins and pressure solutions seams. In general, the faulting accounts for enhanced porosities in the carbonate rocks, ranging up to 20 times higher than the host rock porosity.

The findings of this study indicates that the Jebel Fadeloun anticline corresponds to a buried structure, formed- and aligned parallel with the Tunisian Atlas structures in Late Miocene-Pliocene. Its proposed origin is contractional ramp-related folding. It is suggested that the faults developed either contemporaneous or subsequent to the folding, and relates to similar stress states. Based on the fault analyses and microscopy analyses it is proposed that the fault zones represent combined conduit-barrier systems for fluid flow.

ACKNOWLEDGEMENTS

First and foremost I would like to express my sincere thanks to my awesome supervisors Atle Rotevatn and Thibault Cavailhes for guidance, discussions, and some good laughs during this project. They have truly been inspiring and encouraging, with an overall "no problem" attitude. Thanks for very helpful feedback and reviews on my work. Special thanks go to Atle for motivations.

I would also to express my gratitude to DNO International and the Department of Earth Science at University of Bergen, especially Ståle Monstad, Gunnar Sælen and Atle Rotevatn for including me in this project, and further thanks to DNO International for funding it. Also thanks to Atef Ben Kahla for advices and organizing the fieldwork in Tunisia. I want to thank Bjarte Lønøy, a true "RocknRolla", for some unforgettable memories from the field as well as Alhambra "base camp". Further I want to thank Atef Ben Kahla, Mohamed Riadh Chebbi, Faycel Elferhi and Ahmed Klibi for good field assistance and company. *Shukran*. Thanks to Uni CIPR for allowing me to use their equipment, and especially Eivind Bastesen for good help and discussions.

I truly want to thank my fellow students and friends at the University of Bergen for five incredible years and unforgettable memories at the university, field trips and bars. A special thanks to my "chalcopirates", Heidi, Mette, Merethe, Elin, Thomas, Andreas, Oskar and Ims. Thank you for making these years the time of my life.

I would like to thank my family and friends who have been patient and supportive during my "leave of absence" from life at times. Finally, I would like my one and only Heidi Synnøve for endless help and inspiration.

Bergen 1th of June 2015

Fredrik Sebastian Kjelkenes

TABLE OF CONTENTS

1. INTRODUCTION

This study forms part of a collaborative project between DNO International, ETAP and the University of Bergen. The project, funded and organised by DNO International, aims to map and characterise structural and stratigraphic aspects of the Jebel Fadeloun anticline, Tunisia, with emphasis on Aptian carbonate rocks exposed in its core. Whereas this study focuses on structural analysis, a sister MSc project by Bjarte Lønøy focuses on reservoir characterisation. Data presented are mainly derived from two field seasons, in total of four weeks, carried out in March and September 2014 at Jebel Fadeloun anticline, Tunisia.

1.1 RATIONALE

Carbonate reservoirs are estimated to account for approximately half of the today's hydrocarbon production (Akbar et al., 2000; Ferrill and Morris, 2008). A considerable portion of the reservoirs are enclosed within fold-and-thrust belts, including the prolific Zagros belt of Iran and Iraq (e.g. McClay et al., 2004). Precise analyses of fold and thrust structures, based on surface and subsurface data, often show that apparently simple structures are far more complex than expected (e.g. Poblet and Lisle, 2011). An accurate structural analysis may thus be of major implications in terms of reservoir distribution and hydrocarbon systems.

A common challenge associated with oil production from carbonates, is to cope with the wide range of heterogeneities, including depositional, diagenetic and structural (Akbar et al., 2000). Faulted and fractured reservoirs represent somewhat of a paradox: fractured reservoirs form some of the largest, most productive oil fields, yet on the other hand, some of the poorest, low recovery rate reservoirs on Earth (Bratton et al., 2006). The lack of comprehension of faulted carbonates, and their hydraulic behaviour, has led to an increased focus on the subject (Schlumberger, 2007; Agosta et al., 2010). Studies have shown that fault zones, depending on fault architecture, may serve as combined conduits-barrier systems for fluid flow in the upper crust (Caine et al., 1996; Micarelli et al., 2006; Agosta, 2008). Despite recent advances in the study of faulted carbonates, there is still uncertainties, especially concerning the microscopic processes that are involved and their significance on fluid flow properties (Billi, 2010).

Accordingly, outcrop analogue studies of carbonate reservoirs may (1) significantly improve the understanding of fold-, fault- and fracture characteristics, and (2) provide details that are essential in order to build up predictive models of fault permeability (Wennberg et al., 2006; Agosta et al., 2010). The Jebel Fadeloun anticline provides, therefore, an excellent opportunity to advance the knowledge of carbonate reservoirs in thrust belt settings.

1.2 AIMS AND OBJECTIVES

There are three primary aims of this thesis: 1) to conduct a structural analysis of the Jebel Fadeloun anticline, including characterisations of the fold, as well as the associated faults and fractures, 2) to better investigate how tectonics have impacted the microstructural character of the host rock, and 3) to discuss possible implications for petrophysical properties and fluid flow in carbonate reservoir rocks. The study attempts to achieve these aims with the following objectives:

- Investigate and characterise the large-scale structures in the study area, i.e. fold and faults, by field and seismic observations.
- Analyse fault zones, in terms of (i) structural architecture, (ii) displacement sense, (iii) fracture patterns, (iv) mechanical strengths, and (v) spatiotemporal relationship between the fold, faults, and fractures.
- Study and compare the microscopic structures and petrophysical properties of the fault rocks, relative to the host rock.

1.3 STUDY AREA

The Tunisian Atlas Mountain Belt covers most parts of the northern and central Tunisia, and embodies the Atlassic/Alpine collision between Eurasia and Africa during the Miocene-Pliocene. The study area of this thesis, Jebel Fadeloun (JF), is located in the northeast Tunisia, 25 km west of Gulf of Hammamet (see Figure 1.1). This area represents the boundary between the front of the Tunisian Atlas Mountain Belt and a relatively undeformed geological region, known as the Pelagian Platform, which comprises the areas of eastern Tunisia, northwestern Libya and extends to offshore Malta and Italy.

JF is essentially formed by an outcropping anticline, extending 8 km in length, 5 km in width, and reach 350 meters above sea level at its highest point. The fold exposes Aptian Limestone in its core, and encompass several sets of dissecting faults and fractures. Few studies have investigated the JF anticline: it is partly described by the French-language PhD theisis of Saadi (1990), as well as included in a regional geological map (Rabhi, 2003). Accordingly, the nature of the JF anticline and its faults remains unclear. Details about the geological setting of Tunisia and the study area will be presented in Chapter 3 and Chapter 4.

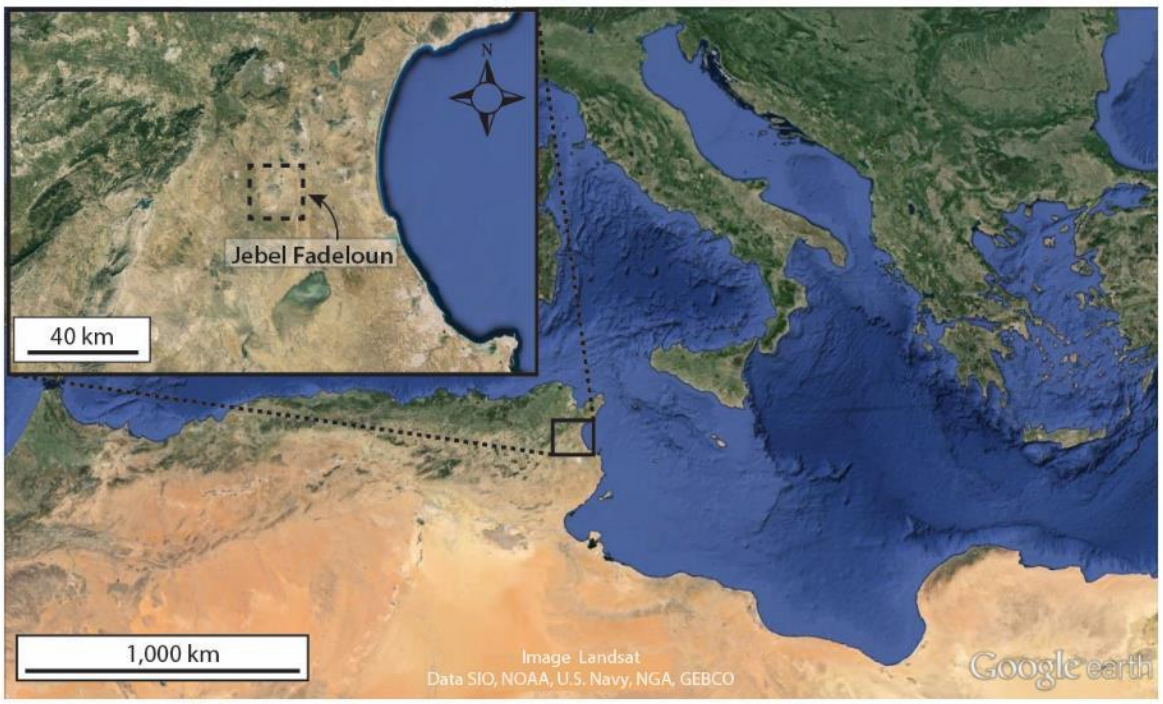

Figure 1.1 – Satellite image of the Western and Central Mediterranean sea. Inset image shows location of the study area.

1.4 METHODS

The study of this thesis is largely based on collected data from fieldwork in March and September 2014, in Tunisia. The applied methods were mostly conventional, including structural- and stratigraphic mapping, and seismic interpretation. Additionally, some less established quantitative methods and tools were applied in outcrop analyses, such as manual rebound hammer and topology scanlines. All the collected field data have been sorted, analysed and presented using software such as Adobe Illustrator CS6, Excel 2013, Stereonet 9.2, ImageJ and Google Earth.

STRATIGRAPHIC MAPPING

Selected parts of the stratigraphy were logged, and classified according to the Dunham (1962) and Embry and Klovan (1971) classification systems. The concept relates to classifying carbonate limestone primarily by depositional textures, such as mud content and abundance of grains (Dunham, 1962; Wright, 1992). These features may be recognised by eye or hand-lens in the field, which allows for adequate field descriptions.

Thickness estimations of unlogged stratigraphy were performed by applying pre-existing, geological map data (1:50 000 scaled) and map thickness equations (eq. 1.1 and 1.2). For a topographic slope and unit of equal dip-directions, the equation is

$$t = |w \sin(\alpha) - h\, cos(\alpha)|\,, \qquad \text{(eq. 1.1)}$$

where |…| annotates absolute values. For a layer and slope of opposite dip-directions:

$$t = w\, sin(\alpha) + h\, cos(\alpha)\,, \qquad \text{(eq. 1.2)}$$

where t = true stratigraphic thickness, w = horizontal distance along a line between the upper and lower unit boundary, α = true dip of the unit, h = elevation difference between end points of the measured line. The equations are modified from Groshong (2006), and assume that measurements are parallel with unit dip-directions, i.e. perpendicular to bedding strike. When estimating stratigraphic thicknesses from map measurements, there are three sources of error, the measured length, dip data, and the contact locations. For instance, a single millimetre on the map corresponds to 50 m, thus thickness errors in the order of ± 10's of meters are likely.

STRUCTURAL MAPPING

Cross sections

In order to perform a structural mapping, measurements of strike and dip orientations were recorded on bedding-, fracture-, and fault planes. The measurements were collected by traditional compass and GPS tracker, or by using a smartphone Android App called "Rocklogger v1.9". The latter method was quality checked with the former and displayed an adequate fit. To create structural cross sections, measurements and lithological observations were carried out along straight paths, parallel and perpendicular to the fold axis. These data were subsequently integrated into a topographical profile over the path, drawn on millimetre-paper, and imported into Adobe Illustrator for graphic optimisations.

Seismic interpretation

Seismic data is widely used by the industry and academia to image subsurface geology. Screenshots of a 2D seismic line, provided by DNO International, was used to interpreted the subsurface expression of the study area. Well ties were not available; hence, stratigraphic key units were recognised by (1) outcropping relationships, i.e. correlating outcrop field data with seismic reflectors, and (2) characteristic, strong reflectors, associated with specific horizons. Limitations of the seismic data need to be acknowledged: Firstly, only a single 2D seismic section is interpreted. Secondly, the 2D seismic section is only available in a picture format, and allows no adjustments. Furthermore, the seismic survey trace is curved, which contributes to additional uncertainties. In addition, the seismic quality varies, showing particularly poor and noisy expressions within the JF anticline, and with increasing depths. Inadequate seismic

imaging is a common problem in thrust belts (Alaei and Pajchel, 2006), as the seismic signal is often distorted by the significant complexities associated with such structural settings. These includes subsurface problems, e.g. steeply dipping fold-, and fault geometries, but also surface issues, such as rough topography and exposed high-velocity rocks (e.g. carbonates).

OUTCROP ANALYSIS

Selected localities were prone to detailed outcrop studies, to investigate the fault architecture and measure the properties of the fault rock. Fault zone descriptions involved qualitative observations (e.g. architecture, appearance, textures) and quantitative measurements (fracture frequency, fault/fracture dimensions and mechanical rock strength). Fracture studies were also performed at sites located away from faults, to capture background fracturing.

Fracture characterisation

To examine the fracture frequency, fractures were recorded along scanlines, oriented either fault-perpendicular, or bed-parallel, depending on the outcrop. All the recorded fracture and fault orientations are presented in equal area, lower-hemisphere stereonets, and plotted as either great circles or directional vectors (half rose diagram). The latter is useful to elucidate orientation trends, as illustrated in Figure 1.2, especially for fractures that tend to have unexposed plane.

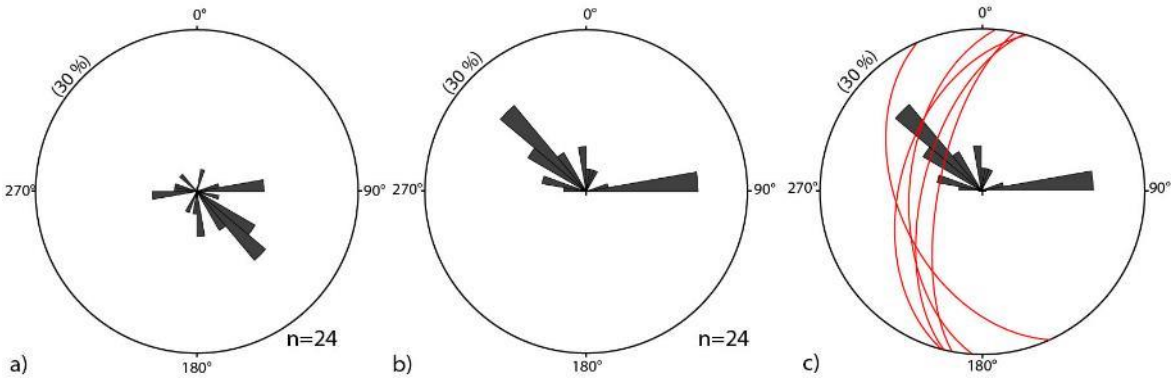

Figure 1.2 – Schematic illustrating the concept of stereonet plots. (a) Standard rose diagram, with directional vectors showing the distribution of fracture orientations. (b) Half rose diagram, where the plots are confined to a half circle, which may elucidate the strike orientations, E-W and NW-SE in this case. (c) Hybrid great circle/half rose diagram. In this example, faults are plotted as great circles, whereas the fracture population as half rose diagram.

Topological analysis (e.g. Nixon, 2013) was used to further characterise the fracture network. The concept is used to classify the topological properties of fracture networks, in order to better understand fracture network connectivity. This is done by classifying the fractures and fracture terminations as branches and nodes (see Figure 1.3). To categorise by fracture nodes,

isolated fracture tips are recorded as I-nodes, linked tips as Y-nodes, and crosscutting intersections as X-nodes. The branches themselves may be categorised into three groups: I-I branches, I-C branches and C-C branches. This classification is based on describing branches by their node at each end (e.g. I-I, I-Y, X-Y), and generalise the nodes as either connected (C), for Y- and X-nodes, or isolated (I) for I-nodes. Thus, the topological analysis is suitable to assess the connectivity of fracture networks (Nixon, 2013).

Whereas topological nodes provide areal frequency (per x^2), most conventional scanlines represents linear frequency (x^1). To compare the two, one may convert nodes, via geometrical relations (eq XX), to linear frequency. Since the I-nodes and Y-nodes represents tip of one line, the number of lines is given by:

$$N_L = ½(N_I + N_Y) \quad \text{(eq. 1.3)}$$

Furthermore, the linear fracture frequency (FF) is deduced from the following:

$$FF = N_L L_C / A \quad \text{(eq. 1.4)}$$

Where LC is the characteristic (average) line length. Equations after Sanderson and Nixon (2015).

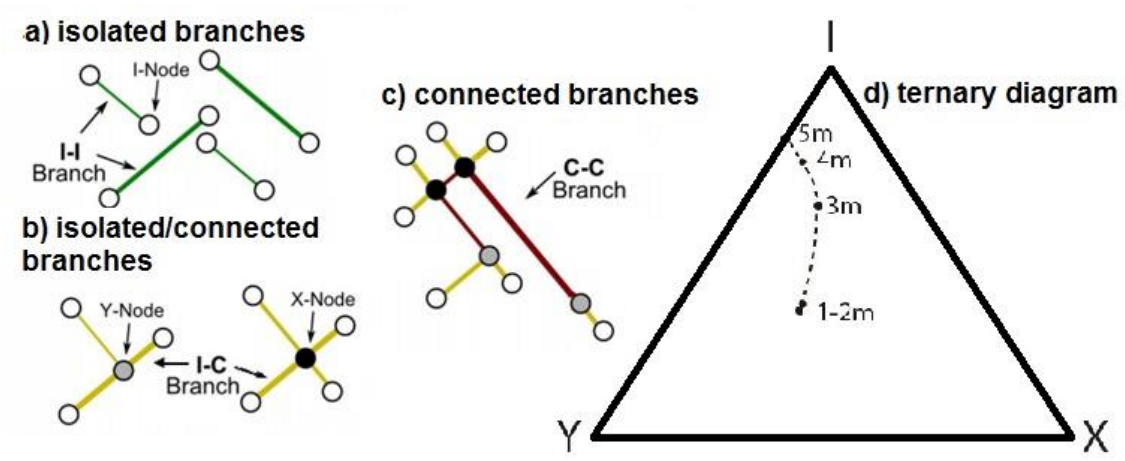

Figure 1.3 – Schematic diagram illustrating the topological classification system, and plotted data in a ternary diagram. Note that each colour relates to a fixed type of node or branch. (a) Isolated branches; composed of unconnected fractures with isolated ends, i.e. i-nodes. (b) Isolated/connected branches; partly linked fracture systems of i-nodes, y-nodes and/or x-nodes. (c) Connected branches; well linked fractures where both nodes terminates in another fracture. (d) The recorded node data may be plotted in a ternary diagram, which in this example illustrates a connectivity profile with distance from a fault. In general, the connectivity increases away from the I-node corner of the triangle. Modified from Nixon (2013).

Mechanical rock strength

To estimate the *in-situ* rock strength within fault zones, a manual rebound hammer (WM250, Type N, by NDT James) was used at selected localities. Essentially, the hammer consists of a spring-loaded piston, which releases once pressed against a surface. The strength of the rock surface is reflected by the piston rebound (the harder the rock, the greater the rebound), expressed by the rebound value (R). Field measurements were taken along a line, oriented perpendicular to the fault plane, covering both the footwall and hangingwall. Each sample consists of at least five strikes, within an area of c. 30 cm^2, where the average corresponds to the rebound number. All measurements were positioned vertically downwards, on top of the bedding plane.

Some influencing factors should be considered: consolidation, weathering, moisture, anisotropy and discontinuities (fractures). All the listed parameters above may attribute to scattered R-values. Preferably, the tests should be conducted on: (i) well-cemented rocks (ii) uniform rocks in terms of weathering and moisture degree, (iii) smooth surfaces, (iv) intact units; avoid loose/highly fractured areas (Aydin, 2015).

The R-values were converted, via empirical correlations, to uniaxial compressive strength (UCS). Several studies address this subject, proposing normalised equations with various parameters, as summarised by Aydin and Basu (2005). For this thesis, the R-values are correlated according to eq. 1.5 after Katz et al. (2000), a relationship frequently used for carbonates (e.g. Morris et al., 2009). The equation is

$$\sigma_{UCS} = 2.21 * e^{(0.07*R)} \qquad \text{(eq. 1.5)}$$

where σ_{UCS}= Uniaxial compressive strength, R=Rebound value.

MICROSCOPIC ANALYSIS

Thirteen samples were collected and prepared for microstructural analysis as polished thin sections, impregnated with blue epoxy. The latter enhance the empty pore space in the samples, and allows for measurements of 2D-porosity (φ_{2D}). An optical microscope with digital camera was used to analyse the thin sections and capture digital images. The use of optical microscopy allows for microstructural characterisation, e.g. deformation structures, fill and pore-types. Microfracture frequencies were obtained by counting the numbers of fractures intersecting a scanline, spanning from each margin of the thin-section, and oriented normal to the predominant fracture trend.

Image-based porosity analysis

The porosity is an important petrophysical property, not only in terms of reservoirs (e.g. aqueous or CO2-storage) but also for the mechanical behaviour of rocks. In order to quantify rock porosities, a number of methods exist, such as thin-section point counting and mercury/helium plug injections. Unfortunately, these methods are time consuming and/or expensive. For this reason, a recently developed method called digital images analysis (DIA) is used. The DIA combines digital images and computer software, in this case ImageJ, and represents an efficient and easy to use method that has gained increasing popularity amongst modern researchers (e.g. Grove and Jerram, 2011; Ghiasi-Freez et al., 2012; Antonellini et al., 2014).

Digital images of the thin sections were acquired by using an Olympus BX51 microscope, on the lowest magnification available (4x), with a Olympus DP72 digital camera set to the highest resolution (Tif-file). Six images were captured in each thin section, representing high-case and low-case porosity. The successive steps of the DIA are summarised and illustrated in Figure 1.4.

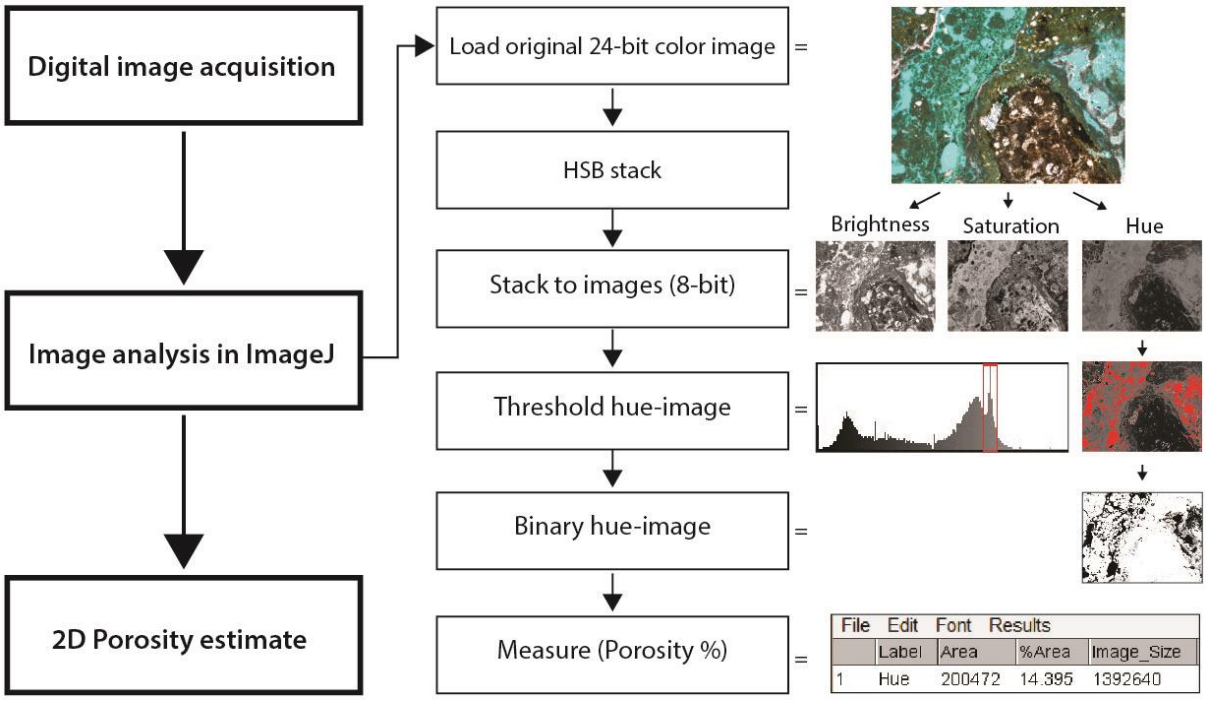

Figure 1.4 - Schematic flow chart of the digital image analysis (DIA). The method measures the 2D-porosity in a thin section image by pixel counting a binary image, thresholded after colour (hue).

2. THEORETICAL BACKGROUND

2.1 FOLD AND THRUST BELT TERMINOLOGY

Fold and thrust (FAT) belts occur worldwide in a variety of tectonic settings, and represents one of the most common modes for accommodating crustal shortening (Poblet and Lisle, 2011). They reflect the result of orthogonal, oblique or transform convergence and collision. Many belts, including the prolific Zagros belt in the Middle East, represent major hydrocarbon resources, and therefor been subject to significant attention ever since the beginning of the oil era. The following section aims to introduce the essential terms associated with FAT belts.

THE CLASSIC FAT BELT MODEL

The classic collisional orogens (Figure 2.1) are doubly-vergent and asymmetric, composed by a uplifted metamorphic core, bounded by two oppositely oriented thrust belts (McClay et al., 2004). The core represents an intensely deformed and metamorphosed region, commonly referred to as the "axial zone", or simply "hinterland". Successively, thrust belts flank the axial zone, characterised by a wedge-shaped framework of thrust faults, folds and related structures. Thrust belts impose an additional crustal load that may result in subsidence and formation of flexural foreland basins in distal parts of the wedge. The term "foreland" refers to the less deformed portions of FAT belts and adjacent continental interior.

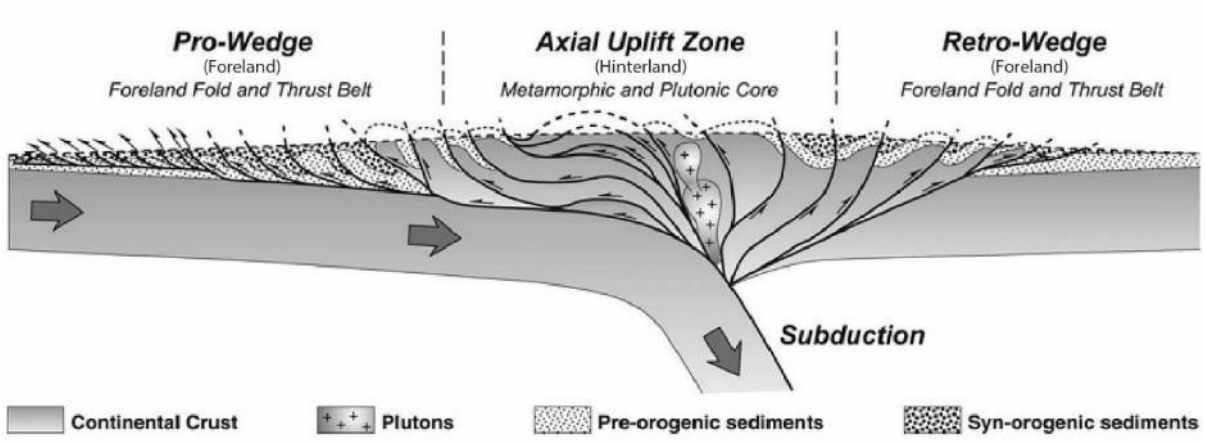

Figure 2.1 – Conceptual illustration of a collisional orogen with doubly-vergent fold and thrust belts, and internal domains. Modified from McClay et al. (2004).

BASEMENT INVERSION

Contractional reactivation of former rift-margins has been recognised in a number of FTB, e.g. the Pyrenees and the Alps (McClay, 2004; Van der Pluijm and Marshak, 2004). The basement inversion model implies that deep-seated extensional faults are reactivated as thrusts, and invokes pre-existing basement fabrics as a fundamental control on the FTB architecture (McClay, 2004).

STYLES OF DEFORMATION

Based on the dominant deformation mechanisms, FTB may be divided into two domains: Thin-skinned and thick-skinned deformation (e.g. McClay, 1992). The former refers to areas where the deformation strictly occurs in the sedimentary cover above a regional basal detachment (i.e. foreland). Conversely, thick-skinned deformation represents basement-involved thrusting, and is characteristic for hinterlands.

Basal detachment faults are sub-horizontal gliding surfaces, hosted by mechanically weak layers (shale/evaporite), and commonly form near or at the basement/sedimentary cover contact (e.g. McClay, 2004). In general, multiple levels of detachments occur, as the basal detachment tend to ramp up to shallower stratigraphic weak-layers, progressively towards the foreland. Likewise, thrust splays tend to branch up from the flat detachment, and may produce a variety of thrust- and thrust-related fold structures (e.g. Jamison, 1987), as illustrated and summarised in Figure 2.2.

Thrust systems

In general, thrust systems can be divided into two end-member types: (I) imbricate fans, and (II) duplexes (Boyer and Elliott, 1982). Imbricate fans (Figure 2.2a-b) comprise a system of linked thrusts that branch upwards from a common detachment surface, i.e. floor thrust, and terminate updip without merging into an upper detachment (e.g. McClay, 1992). An imbricate fan in which the majority of displacement is on the frontal thrust is termed leading imbricate fan. Conversely, a trailing imbricate fan has most of its displacement on trailing thrust (Boyer and Elliott, 1982). An imbricate fan can also be categorised by its thrust sequence. For instance, forward-breaking (piggy-back) thrusting, which is the most common pattern, indicates that younger thrusts nucleate in the footwall of older thrusts, and verge in same direction (McClay, 1995). In contrast to imbricate fans, duplexes (Figure 2.2c-e) form an array of thrusts that are bounded by a floor thrust at the base and a roof thrust at the top (*sensu* Dahlstrom, 1970). The volume of rock bounded by thrusts within a duplex is termed thrust

horse (Boyer and Elliott, 1982), of which the dip direction of the horses characterises the duplex: hinterland dipping or foreland dipping. The dip is controlled by the ratio between displacement and length of horses; commonly displacement is shorter than the length of horses and results in hinterland dipping duplex (Mitra, 1986). Although remarkably rare, a third type of duplex geometry occurs when displacement matches length of horses, known as antiformal stacks (McClay, 1992).

Thrust fault-related folding

The structural styles of thrust-related folds can be characterised in terms of three main modes: (i) fault-bend folds, (ii) fault-propagation folds, and (iii) detachment folds (e.g. Jamison, 1987).

Fault-bend folds (Figure 2.2f) form as a thrust sheet moves over irregularities in the fault surface, e.g. ramps (Suppe, 1983). In his research, Suppe (1983) suggested a fundamental relationship between the fold interlimb angle (γ) and the ramp angle (α). In more detail, specific fold geometries are dictated by the ramp: (i) the backlimb is parallel to the footwall ramp, with fixed fold hinges that reflect the flat-ramp-flat transitions, and (ii) the forelimb terminates in the upper-flat thrust, is shorter and steeper than the back-limb, and its hinges migrates with displacement (Suppe, 1983; Jamison, 1987).

Fault-propagation folds, similar to fault-bends fold, have a direct link with thrust ramps. However, fault-propagation folds (Figure 2.2g) form immediately in advance of a propagating fault tip, whereas fault-bend folds form subsequent to the ramp formation (e.g. Suppe and Medwedeff, 1990; Mitra, 2003). In more detail, folding by layer-parallel slip accommodates strain as the thrust dies out updip while displacement continuous. Similar to fault-bend faults, the backlimb syncline hinge of a fault-propagation fold is fixed; however, the other hinges migrate with displacement (Suppe and Medwedeff, 1990). Characteristics of fault-propagation folds are: (i) asymmetric folds, verging in thrust direction, and (ii) tight interlimb angle (Mitra, 1990; Suppe and Medwedeff, 1990).

Similar to fault-propagation fold, detachment folds develop at the termination of a thrust, however, without a ramp in the underlying thrust. Rather, detachment folds (Figure 2.2h) forms above a bedding detachment where slip occurs along the layering, preferentially within a ductile unit (e.g. Mitra, 2003). Generally, detachment folds develop in layered sequences with substantial thickness and competency contrast (Jamison, 1987; Mitra, 2003). In terms of fold geometry, detachment folds are typically more symmetric and more likely to display

opposite sense of vergence both across and along fold trends, compared to fault-bed folds and fault-propagation folds (Mitra, 2003).

Additional folding mechanisms

There are additional folding mechanisms that, although not restricted to, may occur in thrust belt settings, for instance: (I) folding by salt mobilisation, (II) transpressional folding, and (III) contractional inversion.

Salt mobilisation (Figure 2.2i) can occur in most settings where salt is present (e.g. Jackson and Talbot, 1991). The primary driving force of salt tectonism is differential loading, which may be induced by gravitational (overburden), displacement (regional extension or shortening), or thermal gradients (e.g. Hudec and Jackson, 2007). A variety of structures can form in the context of salt tectonism, e.g. salt walls, domes and pillows, depending on the (i) source geometry, i.e. line or point, (ii) structural maturity, and (iii) interaction with regional deformation.

Transpressional stress is associated with local restraining bends along strike-slip faults (e.g. Woodcock and Rickards, 2003). This may result in a variety of contractional structures, including thrusts and folds, which in map-view commonly develop an *en echelon* arrangement and imbricate fault patterns, as well as positive flower structures (Figure 2.2j) in cross-section (Woodcock and Fischer, 1986; Woodcock and Rickards, 2003).

Contractional inversion (Figure 2.2k) of former extensional faults and related basins is a particularly common phenomenon in FTB settings (Bonini et al., 2012). Normal faults may accommodate inversion by reactivation, but also by localising thrust splays and folds (Scisciani, 2009). Hence, inversion tectonics may result in complex geometries, as several studies have shown (e.g. Coward et al., 1991; Scisciani, 2009). Several controlling factors of fault reactivation have been emphasised: fluid pressure, fault dip, shortening direction, sediment loading, as well as the importance of a basal ductile layer (e.g. Turner and Williams, 2004; Bonini et al., 2012). A diagnostic feature of an inverted basin, is the contrasting offsets between separate sedimentary units: the upper units show contractional offset, whereas the lower units show extensional offset. These two domains are separated by the null point, i.e. the point where a certain syn-tectonic marker unit has regained its regional elevation by inversion (*sensu* Williams et al., 1989).

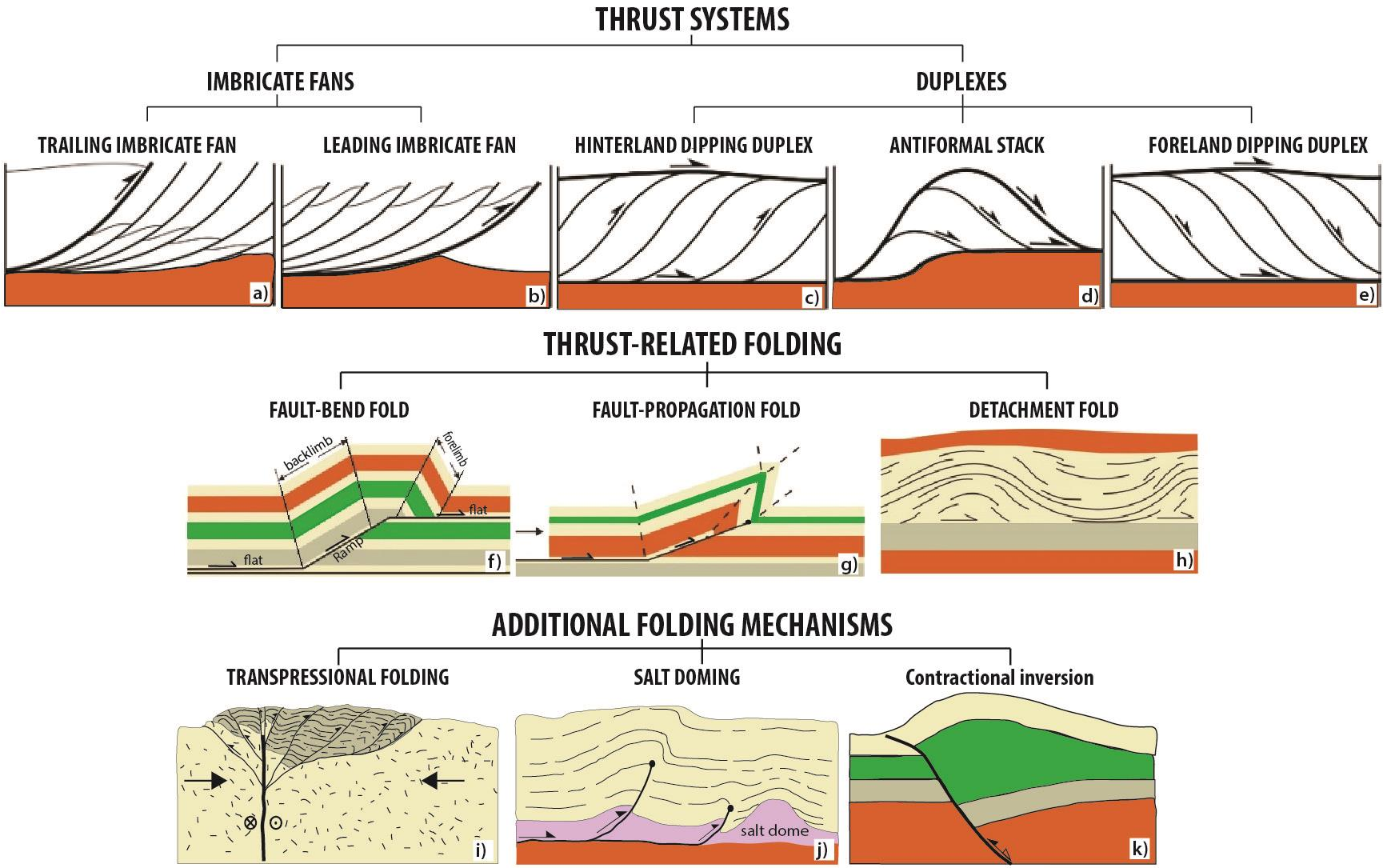

Figure 2.2 – Schematic overview of characteristic structures of FTB. Note that some of these, e.g. salt doming and flower structures, are not exclusively related to fold and thrust belts. Modified after Boyer and Elliott (1982); Van der Pluijm and Marshak (2004); Williams et al. (1989).

2.2 FAULT ZONE ARCHITECTURE

Brittle fracturing and faulting generally occurs in the uppermost crust, at low confining pressures, and may form complex fault zones that evolve spatiotemporally with respect to structural and fluid flow properties (Shipton and Cowie, 2001; Wibberley and Shipton, 2010; Agosta et al., 2012). A first-order description of the fault zone architecture (see Figure 2.3) commonly includes three structural components: fault core, damage zone and host rock (Caine et al., 1996; Bense et al., 2013). The structural architecture seems largely controlled by the displacement magnitude, host rock and depth of deformation (Micarelli et al., 2006; Faulkner et al., 2010).

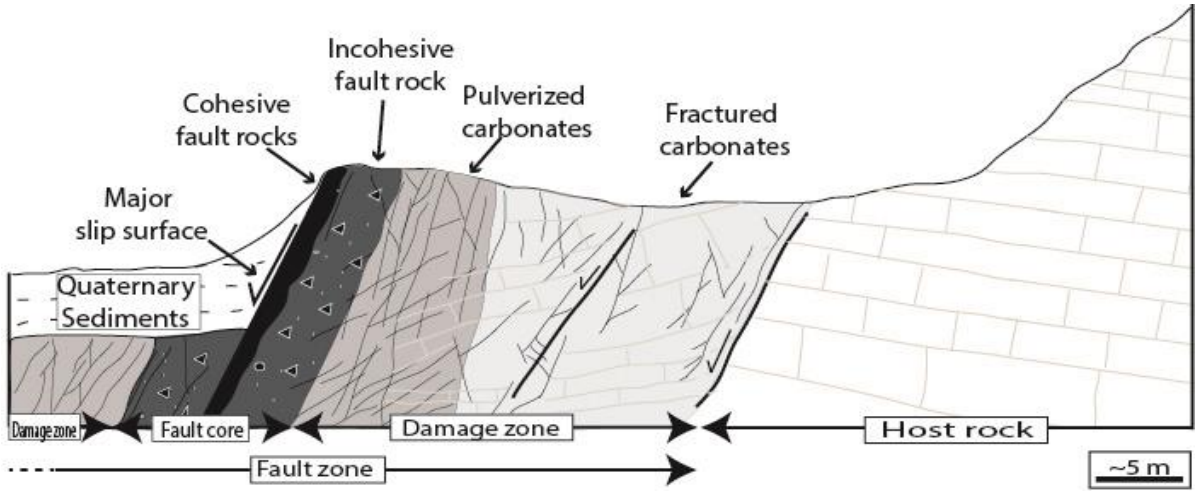

Figure 2.3 – Illustrational cross-section of the fault architecture, with internal domains and their characteristics. Note the (i) preserved primary fabrics in the damage zone, and (ii) obliterated primary fabrics in the cataclastic deformed core region. Modified from Agosta (2008).

Fault cores may develop around major slip surfaces and accommodates the greater strain from the fault-displacement, as reflected by intensely deformed fault rocks, e.g. gouge, breccia, cataclasite. Pre-existing sedimentary fabrics are fully destroyed by cataclastic flow (grain comminution/rotation), dissolution/precipitation, mineral reactions or other mechanical/chemical processes (Chester and Logan, 1986; Caine et al., 1996; Micarelli et al., 2006). Fault cores are commonly discontinuous, ranging from centimetres to a few meters wide, and heterogeneously distributed along fault-strike and fault-dip (Micarelli et al., 2006). The damage zone flanks the core and is characterised by fault-related fractures and minor faults (Caine et al., 1996; Agosta and Aydin, 2006). In general, the fracture density decreases as a function of distance from the slip surface (Faulkner et al., 2010), and opposed to the core; primary fabrics are commonly recognisable within the damage zone. The host rock is found

outside the deformed fault envelope, surrounding the damage zones, and is characterised as undeformed or background-fractured rock (Agosta and Aydin, 2006).

Childs et al. (2009) argues that the components of the fault architectural model proposed by Caine et al. (1996) lack unique definitions, causing difficulties for measuring outcrop thicknesses. As an alternative, they propose a new classification of fault architecture, including components such as fault rock, fault zone, relay ramp and damage zone. However, our observations from the study area correlated better with the model of Caine et al. (1996), and the terminology defined therein will be used in the fault descriptions in this thesis.

The lithology of the host rock seems to have a significant impact on the fault architecture. Ferrill and Morris (2008) describes the importance of mechanical stratigraphy and its influence on carbonate fault zones (Figure 2.4). Accordingly, faulting in mechanically competent (massive, clay-poor) limestone-sequences form planar and narrow fault zones, characterised by steep faults, minor fault block tilting and absences of ductile structures such as fault-related folding and clay/shale smear. In contrast, fault zones incompetent (clay-rich) sequences are associated with laterally variable widths, displacements and bed dips, in addition to moderate-to-steep faults, clay smearing and folding by strain sinking weak layers.

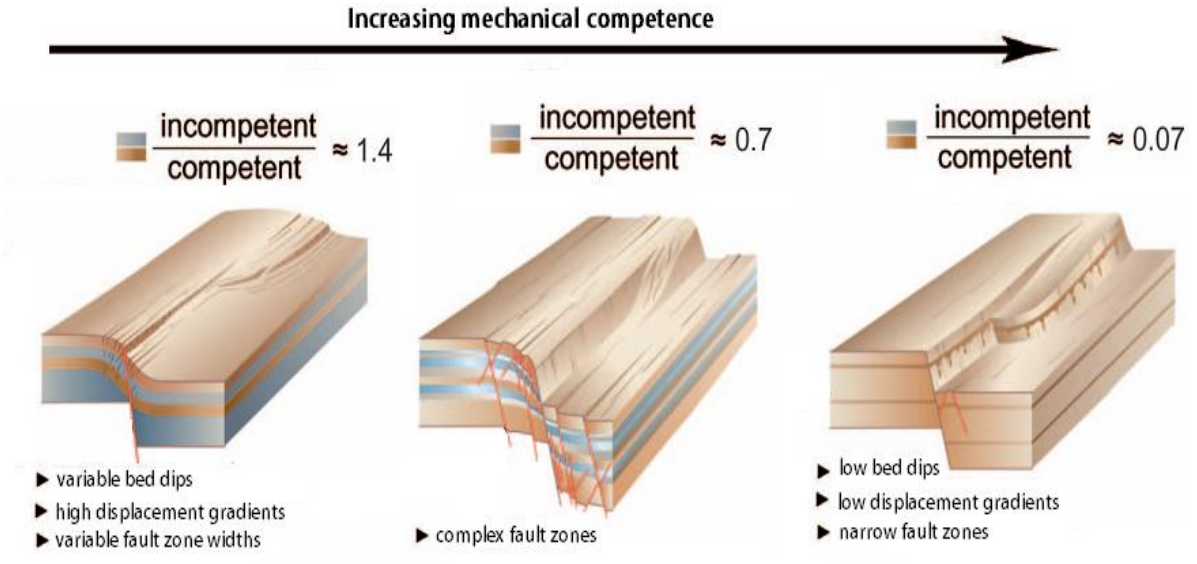

Figure 2.4 – Conceptual illustration of the mechanical stratigraphy and its impact on fault zone geometry and characteristics. Modified from Ferrill and Morris (2008).

Caine et al. (1996) proclaims that the architectural components and their distributions control fluid flow properties of fault zones. Conceptually, fault cores form barriers to across-fault fluid flow, due to grain-size reductions and mineral precipitations; whereas, damage zones, dominated by connected fractures, may represent permeability-enhanced systems (Caine et

al., 1996; Billi et al., 2003). Hence, fault zones may form barrier, conduit, or combined conduit-barrier systems for fluid flow. According to Faulkner et al. (2008), the petrophysical properties of the host rock may strongly affect the fault permeability. Faulted low-porosity host rocks commonly produce highly fractured damage zones, associated with enhanced secondary porosity (φ) and permeability (κ). In contrast, damage zones in high porosity rocks may represent reduced φ and κ, due to pore collapse, and/or development of deformation bands (Faulkner et al., 2010; Agosta et al., 2012). Traditionally, deformation bands form in sandstones and represents impermeable membranes; however, their existence have also been reported from porous carbonates (e.g. Bonson et al., 2007).

Authors (e.g. Agosta, 2008; Bense et al., 2013) have described a significant difference between the fault permeability model in clastic rocks and carbonate rocks (Figure 2.5). Whereas clastic fault zones represents permeability reduction relative to the host rock, carbonate fault zones may form both significant fluid pathways and barriers. This peculiar behaviour may be ascribed to the extremely reactive nature of $CaCO_3$. Accordingly, dissolution and precipitation along fractures and faults may, respectively, enhance or reduce secondary φ and κ (Bense et al., 2013).

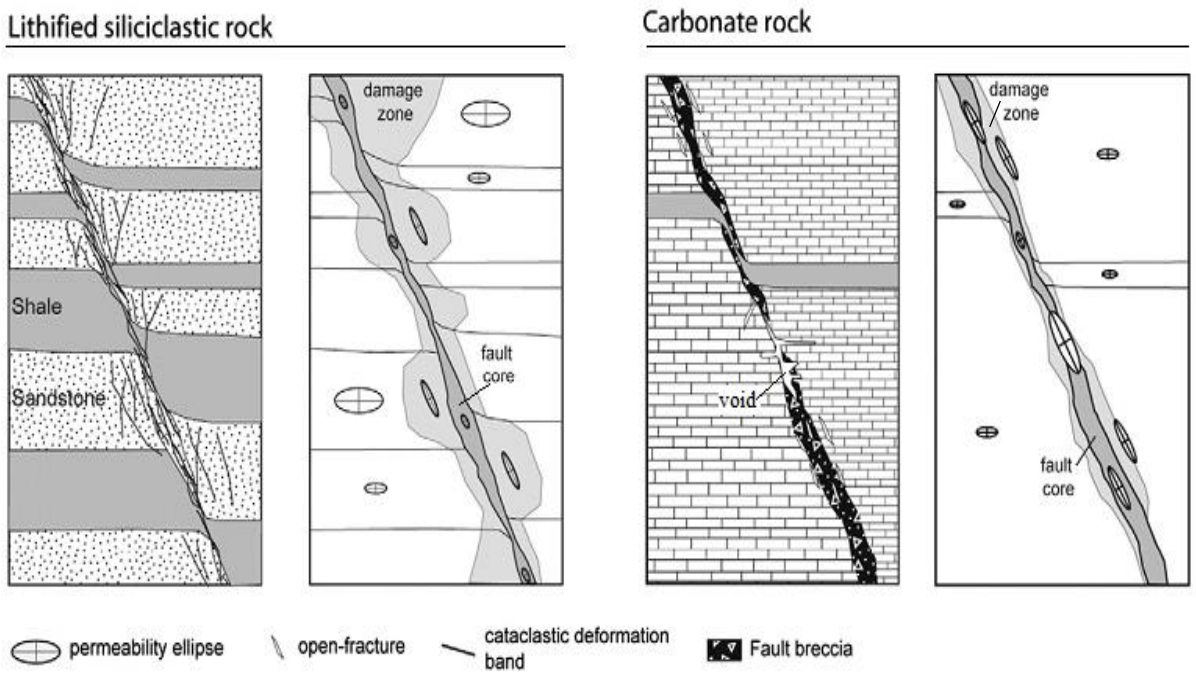

Figure 2.5 - Fault architecture and related conceptualised models of fault permeability in clastic and carbonate rocks. Note that (1) the permeability ellipses illustrates the dominant fluid flow vectors, and (2) overall reduced fault permeability in the clastics, versus enhanced in the carbonates, relatively to the host rock. After Bense et al. (2013).

3. GEOLOGICAL SETTING

The purpose of this chapter is to introduce the regional geology of Tunisia in a spatiotemporal context. Tectonic events through the entire Phanerozoic, related to the evolution of the western and central Mediterranean region, have resulted in a complex and fascinating geology. For convenience, the regional geology is divided into tectonic and stratigraphic parts; however, the strong link between them should be recognised, as they affect one another in a geodynamic system.

3.1 REGIONAL TECTONIC SETTING

3.1.1 GENERAL FRAMEWORK

The geology of Tunisia may be divided into four regions based on structural and stratigraphic features: The Saharan Tunisia, Tunisian Atlas, Pelagian Platform and North-South Axis.

The Saharan Tunisia

The southern Tunisia is commonly referred to as Saharan Tunisia, or the Saharan Platform. It is essentially a flat plateau with gentle topography. The stratigraphy is unfolded, but slightly uplifted towards the north, causing it to dip gently to the southwest (Burollet, 1991). Trough-forming extensional faults, trending E-W to ESE-WNW, mark the transition from the northern margin of Saharan Tunisia to the Tunisian Atlas. This transition, known as the Chotts-Gafsa Zone, is associated with E-W elongated ranges and deep basins (Burollet, 1991; Mejri et al., 2006). The E-W fault system corresponds to the southern paleo-margin of the Tethys, an ancient Paleozoic-Mesozoic ocean (Burollet, 1991; Mejri et al., 2006; Khomsi et al., 2009).

The Tunisian Atlas

One of the most prominent features of the Tunisian landscape is the series of NE-SW elongated ranges that covers most of the western and northern regions. These ranges are formed by outcropping folds and thrusts that reflect the imprint of the Atlassic Orogeny; a series of mountain chains, spanning from Morocco to Tunisia and shaped by convergence between the African and European plates during the Cenozoic Era. In general, the Tunisian Atlas grades from stacked nappes in northernmost part (Tellian Atlas), to thrusts and broader folds further south (Mejri et al., 2006). Diapiric extrusions of evaporites and clay occur all over the region, and frequently form the basal contact of thrusts sheets, suggesting they provide a fundamental detachment surface (Burollet, 1991; Anderson, 1996).

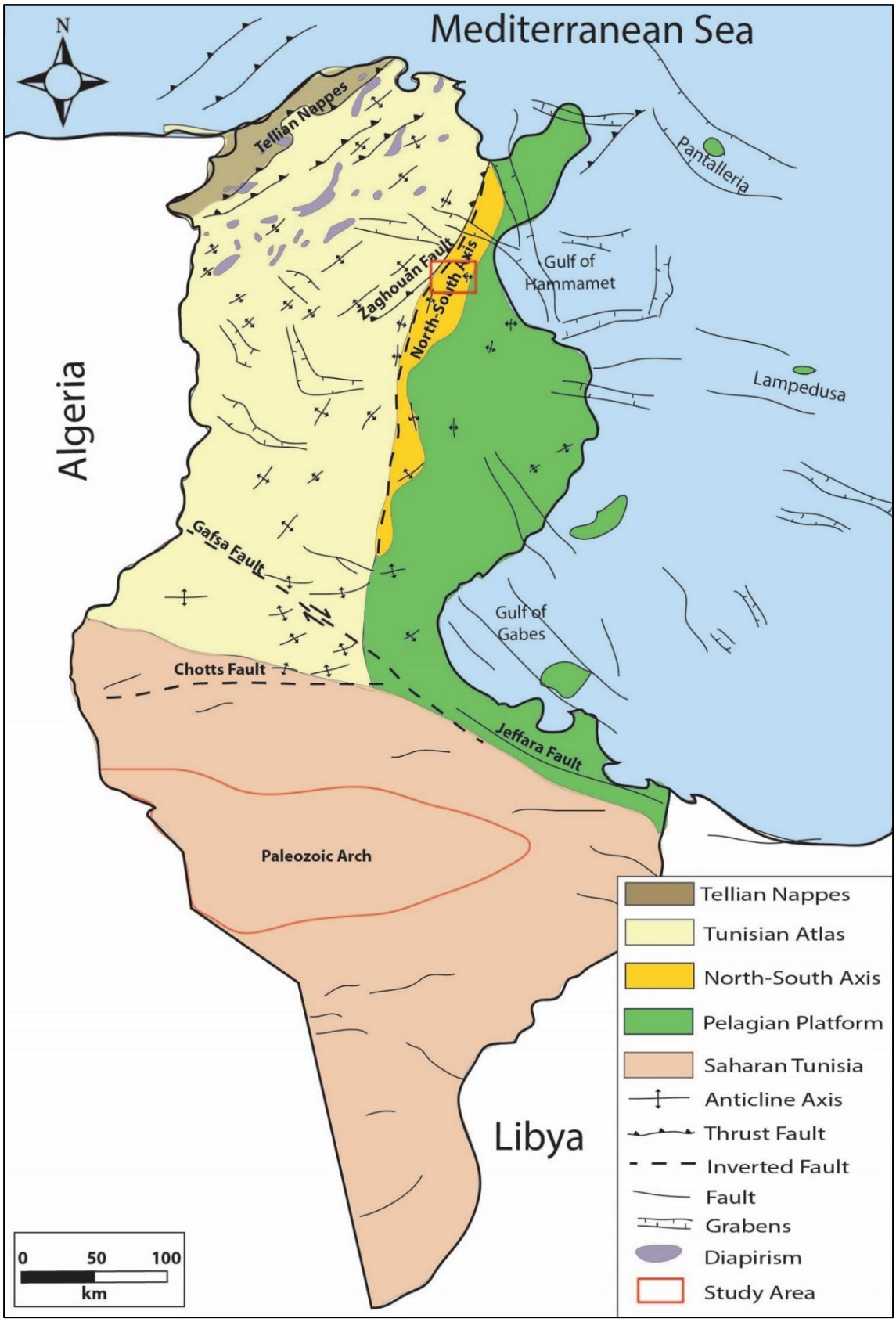

Figure 3.1 – Tectonic sketch over Tunisia. Notice the four domains: Tunisian Atlas (including the Tellian Nappes), North-South Axis, Pelagian Platform and Saharan Tunisia. Notice (i) the predominant NE-SW atlassic trend, (ii) N-S trends in the North-South Axis, and (iii) NE-SW trending grabens. (Modifed Burollet, 1991; Anderson, 1996; Hlaiem, 1999; Mejri et al., 2006).

Most of the tectonic lineaments in the Tunisian Atlas possess the atlassic NE-SW trend; however, some structures are separated by elongated grabens or half-grabens, formed by NW-SE to WNW-ESE trending faults. According to Bouaziz et al. (2002) and Mejri et al. (2006), these grabens originated during extensional phases in Late Cretaceous and Oligocene, and commonly reactivated in as dextral strike-slip faults in Late Miocene. Others (e.g. Ben Ayed, 1980; Jallouli and Mickus, 2000) suggest they formed as pull-apart basins by transtensional faulting.

The Pelagian Platform

The lowlands and shallow continental shelf of Eastern- and offshore Tunisia corresponds to a relatively stable carbonate platform known as the Pelagian Platform, which extend as far as the Maltese Islands in the northeast, and northwestern Libya in the southwest (Burollet, 1991; Klett, 2001; Bey et al., 2012). For clarification, the term "Pelagian Platform" will hereby be restricted to Eastern Tunisia, including both onshore and offshore.

In several papers (e.g. Bishop, 1988; Burollet, 1991; Anderson, 1996), the platform has been considered as relatively stable and depicted as a zone that passively subsided in front of the Atlas during most of Cenozoic time. Accordingly, a structural boundary, known as the North-South Axis, accommodated most of the strain from the western margin of the atlassic orogeny, and decoupled the Pelagian Platform from the extensive deformation. Recent studies (Khomsi et al., 2006; Khomsi et al., 2009) contest these claims, invoking atlassic deformation (thrusting and folding) based on well ties and high-resolution seismic data from both onshore- and offshore Tunisia. In their interpretations, an atlassic foreland basin was formed on top of the Pelagian Platform and subsequently deformed by eastward propagation of the thrust belt front.

Although the degree of Atlassic deformation is debated, the Pelagian Platform is inevitably distorted by a complex system of NW-SE to E-W trending faults, which forms numerous horsts and grabens in the offshore Tunisia. Most of these structures originated post-atlassic, and contemporaneous with the Pantelleria-Malta-Linosa rifting during regional Late Miocene-Pliocene NE-SW extension in the Pelagian Platform (Bouaziz et al., 2002; Khomsi et al., 2009). Different explanations have been proposed for this regional extension. Jongsma et al (1987) proclaimed that these rifts initiated as pull-apart (transtensional) basins, due to oblique plate convergence. Yet, Argnani (1990) suggested an alternative model, involving N-S oriented extension associated with back-arc extension in the Tyrrhenian Sea, as a response to

a complex subduction zone between the converging African-European Plates. Additionally, expressions of magmatic activity related to the extensional events in Cretaceous and Late Mio-Pleistocene times, occur throughout the Pelagian Platform (Mejri et al., 2006).

The North-South Axis

The western margin of the Pelagian Platform is separated from the Atlassic highlands by a major tectonic lineament called the North-South Axis (NOSA) (Bey et al., 2012). This corridor of steep, elongated ranges, stretches hundreds of kilometres, from the northern margin of the Saharan Platform, through central Tunisia and continues to the northernmost tip of Tunisia (Burollet, 1991). As its name implies, the North-South Axis is oriented roughly N-S and grades to NE-SW towards north.

The origin of the NOSA is debated, several studies (e.g. Burollet, 1991; Bouaziz et al., 2002) have ascribed it to a basement fault system, likely inherited from Precambrian or Paleozoic events, which was inverted during Atlassic compression. Accordingly, this feature acted as a barrier and decoupled the Pelagian Platform from the collisional deformation. Conversely, Boccaletti et al. (1990) interpreted the NOSA as transpressive, positive flower structure, formed post atlassic-compression during Mio-Pliocene. Anderson (1996), on the other hand, contests this, claiming that the transpressive model lacks convincing evidence, and rather suggests that the NOSA represents the thrust front of the Atlassic, thin-skinned thrust belt. Additionally, Anderson claims that basement fault inversion only played a minor role in the deformation.

3.1.2 STRUCTURAL EVOLUTION / TECTONIC HISTORY

The tectonic history of Tunisia may be subdivided and summarised in the following chronological steps: 1) Caledonian and Hercynian collisional events, 2) Tethyian rifting, 3) Atlassic phases.

1) Caledonian and Hercynian collisional events (Ordovician to Carboniferous)

The supercontinent Pangea formed during Paleozoic times by the linkage of Laurasia and Gondwana through continental collisions (e.g. Caledonian and Hercynian events). Although there is no direct evidence in Tunisia of these collisions, they may be inferred through geophysical and well data from the Saharan Tunisia, where the older Paleozoic units have been folded, uplifted and eroded (Mejri et al., 2006).

2) Tethys rifting (Late Carboniferous to Lower Cretaceous)

Subsequently to its formation, rifting began to fragmentise Pangea and form today's northern margin of the African plate. The related fault system trend predominantly E-W to NW-SE, likely inherited from Paleozoic events (Zouaghi et al., 2011). Consequently, rifting and subsidence led to the opening of the ancient Tethyan seaway, which flooded the North African shelf in the Late Carboniferous-Permian times (Klett, 2001). Great thicknesses of Triassic-Lower Cretaceous units of evaporite and carbonate, suggests a considerable subsidence during Mesozoic times, that continuously generated accommodation-space for the sedimentary infill (Burollet, 1991). Shortly after its deposition and burial, the Triassic evaporites began to remobilise by halokinesis (Mejri et al., 2006).

According to Klett (2001) and Mejri et al. (2006), several N-S and E-W normal faults formed in the NOSA region during the Early Mesozoic and played an active role in the sediment distribution. In general, the area east of NOSA was more stable and represented shallower facies than the western side (i.e. the opposite of today's landscape) (Mejri et al., 2006).

3) Atlassic phases (Late Cretaceous – Pliocene)

The first expressions of the convergence between the African and European plates appeared in the Late Cretaceous and continued more or less throughout the Cenozoic Era. However, complex structural and sedimentary patterns, e.g. spatiotemporally heterogeneous episodes of faulting and associated growth strata (Bouaziz et al., 2002; Mejri et al., 2006), reveal a polyphasal deformational history that may be subdivided into the following four phases: I) Late Cretaceous compression, II) Mid-Late Eocene compression, III) Oligocene extension, IV) Late Miocene-Pliocene compression.

I. The Late Cretaceous compression was oriented NW-SE, resulting in initial NE-SW trending atlassic folds. A regional unconformity, named the Austrian unconformity, reflects this uplift (Burollet, 1991). The folds proximate to the NOSA were retarded by this strain-accumulating barrier, and thus forced to obtain a subparallel, N-S trend. Extensional expressions also occurred in Late Cretaceous, especially in eastern Tunisia where NW-SE oriented grabens formed by transtensional faulting, and active volcanism occurred locally (Mejri et al., 2006).

II. In the Mid to Late Eocene, contemporaneous with the Pyrenean orogeny in Europe, the NOSA was reactivated by a contractional phase when the stress rotated approximately N-S. This led to a reversal of the relationship between western Tunisia

and eastern Tunisia: Previously higher and more stable grounds in the east began to subside and form the lowlands and flooded offshore regions that we observe at present time (Mejri et al., 2006).

III. An Oligocene extensional phase has been recorded by commonly NW-SE trending normal fault populations with syn-tectonic growth strata in north-central Tunisia (Bouaziz et al., 2002). Several of these normal fault sets were subsequently folded, and some re-activated as dextral strike-slips faults, during Late Miocene-Pliocene deformation (Bouaziz et al., 2002).

IV. The continuous convergence between Africa and Europe was intensified in Tunisia with a major compressional event in Late Miocene, commonly referred to as the Atlassic/Alpine Orogeny (Klett, 2001; Mejri et al., 2006). The impact was onset in northern Tunisia, by the arrival of the Tellian thrust nappes, derived from NNW. Ultimately, the reorientation of the stress state to NW-SE led to reactivation and forming of the characteristic NE-SW trending folds in the Atlas region (Bouaziz et al., 2002). Studies have recorded a south-eastward migration of the deformation front (Bouaziz et al., 2002). The compression continued into Pliocene by folding and local overturning of the nappes in the north (Burollet, 1991). In the offshore Pelagian platform, regional NE-SW rifting formed or rejuvenated NW-SE trending grabens, contemporaneous and sub-parallel to the Pantelleria-Malta grabens (Bouaziz et al., 2002; Khomsi et al., 2009). Late Miocene-Pliocene sinistral transpression, along the NOSA region, has been proposed by Boccaletti (1990) and Mejri et al. (2006). Regionally, neo-tectonic movements have occurred up to modern times in Tunisia.

3.2 REGIONAL STRATIGRAPHIC FRAMEWORK

The regional stratigraphy of Tunisia (see Figure 3.2) display wide lateral facies variations. For this reason, the following chapter aims to present a regional stratigraphic column, representative for the study area region, in Northeast Tunisia. Paleozoic rocks are excluded, since they generally do not outcrop in Tunisia, and offers no relevance for this thesis.

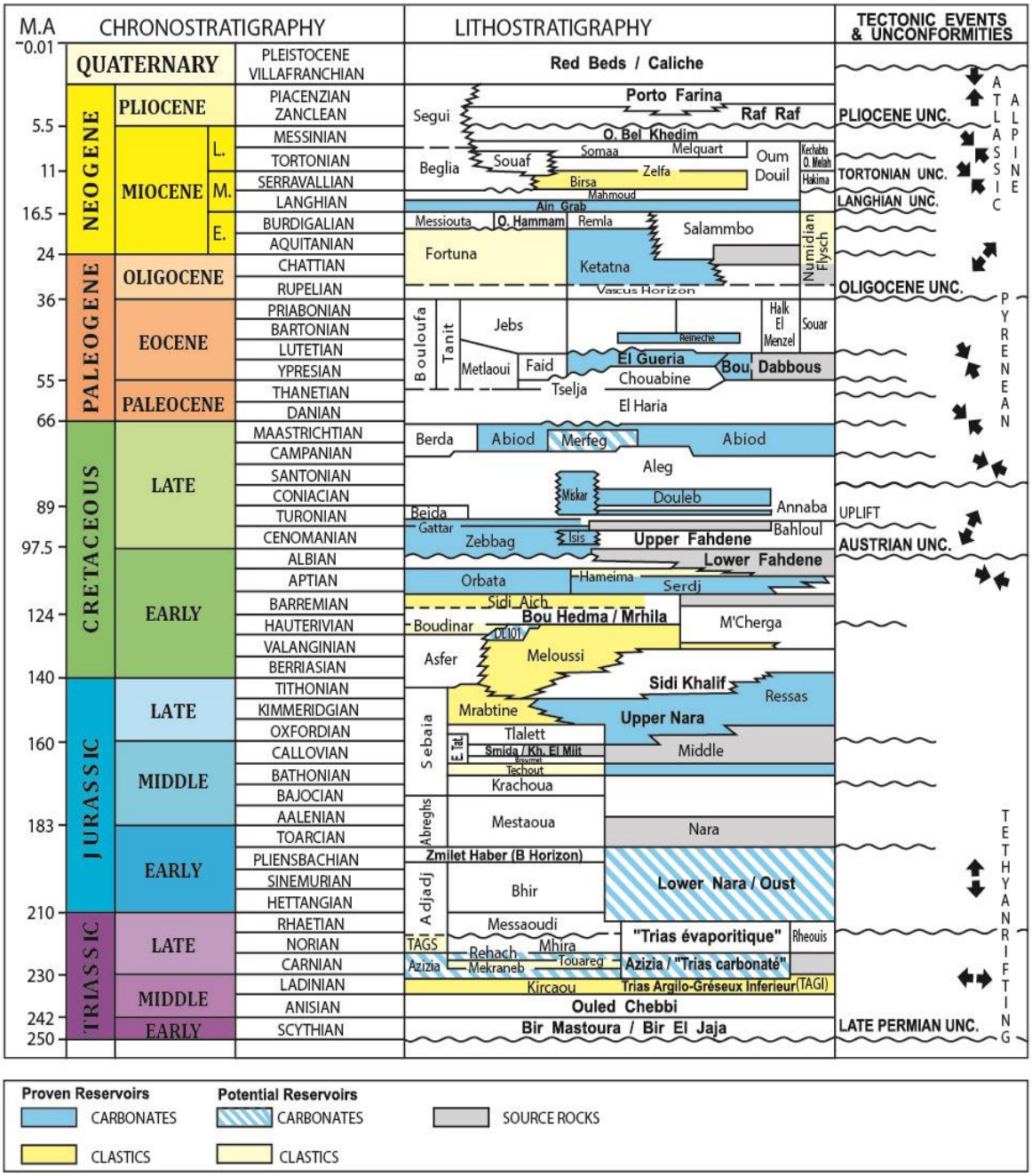

Figure 3.2 – Stratigraphic chart of Tunisia, including lithostratigraphy, major tectonic events and unconformities through the Mesozoic and Cenozoic Era. Modified from ETAP (2001)

Triassic

The outcropping Triassic succession has a peculiar appearance: although well-exposed in numerous diapiric extrusions all over the Tunisian Atlas, the primary Triassic series is largely obliterated by salt remobilisation, and blended to a homogenous mass of evaporites, clay and silt (Mejri et al., 2006). This extrusive form of Triassic rocks is labelled as the Rheouis Formation. Nevertheless, an *in-situ*, conformable Triassic succession outcrops in the Saharan Tunisia that according to Mejri et al. (2006) correlates with the undifferentiated extrusions. Two main intervals are identified, a lower clastic interval and an upper evaporitic interval, where the two are separated by a dolomitic section (Bishop, 1975; Klett, 2001). The lower interval, of Scythian-Ladinian age, consists of red sandstone and shale, corresponding to the Bir Mastoura, Bir El Jaja, Ouled Chebbi and Kirchaou formations. A dolomitic section, of Late Ladinian-Carnian age, marks the boundary between the lower and upper intervals, and corresponds to the Azizia and Trias Carbonate formations. The uppermost interval, of Norian-Rhaetian age, is comprised by gypsum, salt and anhydrite, interbedded with minor clay and dolomite units, and relates to the Trias Evaporitique Formation (Klett, 2001; Mejri et al., 2006). A continental to shallow marine depositional environment is envisaged for the clastic interval, respectively from south to north (Bishop, 1975; Klett, 2001). Successively, restrictions of the western Tethys realm, alongside rift-controlled subsidence, led to deposition of epicontinental evaporites (Bishop, 1975; Bouaziz et al., 2002).

Jurassic and Lower Cretaceous

A carbonate platform formed in the Jurassic, on top of the Triassic deposits. The platform sloped towards the north-northwest, resulting in a shallow marine, platform in the south and progressively deeper-water, marine facies to the north (Klett, 2001 and references therein). The Hettangian-Barremian sequence consists predominantly of carbonates, including limestones, dolomites and marls of the Nara, Sidi Khalif and M'Cherga formations (Burollet et al., 1978). A clastic system of deltaic facies developed in the south during the Kimmeridgian, and prograded northwards until Barremian times. These clastic deposits corresponds to the M'Rabtine, Meloussi, and Boudinar formations (Mejri et al., 2006). A maximum flooding event occurred during the Barremian to Aptian, resulting in the deposition of transgressive units of pelagic limestone and marl, which forms the Bouhedma and M'Cherga formations (Klett, 2001). Overlaying the M'Cherga Formation, the Serdj Formation of Aptian age consists of bioclastic and reefal limestones, interbedded with marl

and silt, and reflects an inner-shelf carbonate platform setting (Mejri et al., 2006; Heldt et al., 2010).

Late Cretaceous

The Late Cretaceous, including the Albian, is represented by the Sidi Mansour Group, which consists of three formations: The Fahdene, Aleg and Abiod Formations (Mejri et al., 2006). The Fahdene Formation, of Albian-Cenomanian age, consists of shale and pelagic limestones. A distinct layer of thinly laminated limestone and intercalated marl, represents the Bahloul Member and marks the boundary from the Fahdene Formation to the overlaying Aleg Formation. The Aleg Formation, of Turonian-Campanian age, comprises pelagic limestones with interbedded marl. The Campanian to Maastrichtian Abiod Formation overlies the Aleg Formation, and is characterised by chalky limestones, mudstones and marly units. Frequently, unconformities occur at the boundary between top Aleg Formation and base Abiod Formation, and these have been ascribed to both tectonic activity and salt migration. The overall depositional environment envisaged for the Late Cretaceous is inner shelf to open marine. As a prominent part of the stratigraphy in the study area, the Cretaceous interval is further emphasised in section 4.2.2.

Cenozoic

Tectonic activities recommenced in Late Cretaceous/Paloecene, as the African Plate converged towards the European. Consequently, the Cenozoic successions encompass a gradual shift from marine to continental facies (Figure 3.3). The Cenozoic series may be divided into three stages: I) Paleocene to Eocene shale and limestone units; II) Oligocene to Early Miocene of varying facies; III) Middle Miocene to Pleistocene, synorogenic facies including molasses:

I. The El Haria Formation of Maastrichtian to Paleocene overlays the Abiod Formation, and is characterised by distinct green-coloured shales with interbedded minor limestone beds. Successively, the Ypresian (Lower Eocene) is represented by the Bou Dabbous Formation, consisting of pelagic limestones. Lastly, the Souar Formation of Middle to Upper Eocene comprises alternating shale and limestone units.
II. The Oligocene – Early Miocene interval includes a variety of facies, from deep marine to continental. In Central and Northeast Tunisia, this interval is characterised by massive, continental sandstone units of the Fortuna Formation. Commonly, a hiatus marks the boundary between the Souar Formation and Fortuna Formation, which

depicts a regional Oligocene unconformity (Klett, 2001; Mejri et al., 2006). The source of the clastic material is not well understood, but observations indicate transportation from southwest to northeast (Burollet et al., 1978).

III. Tectonic uplift during the Late Oligocene/Early Miocene resulted in erosion and a large depositional hiatus. The transgressive limestone unit of Ain Grab Formation of Middle Miocene age thus unconformably overlies the Oligocene – Early Miocene Fortuna Formation. In the Mid- to Late Miocene, the depositional environment became progressively shallower, reflected by clastic units of conglomerate, sand and shale, which corresponds to continental, fluviolacustrine and shallow marine facies of the Oum Douil Group (Patriat et al., 2003).

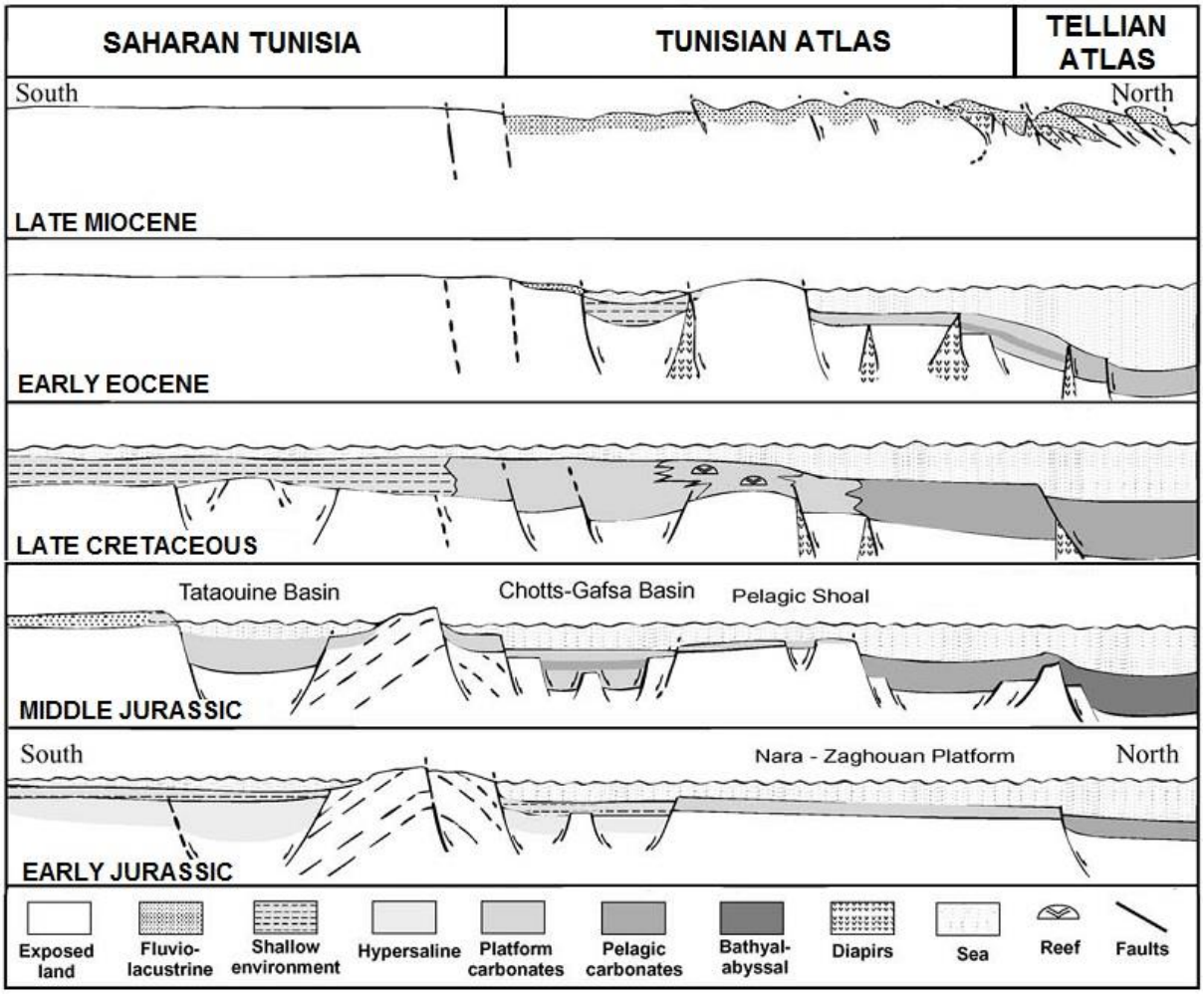

Figure 3.3 – Tentative N-S sections of Tunisia, illustrating the tectono-sedimentary evolution from the Mesozoic to the present state. Notice the (i) rifting and deposition of basinal salt and platform carbonates during Early Jurassic, (ii) first outlines of atlassic compression in Late Cretaceous by folding and diaprism, accompanied by northwards facies variation, from shallow-, to deep-marine, and (iii) inversion and thrusting in the main compressional event, Late Miocene, resulting in regional uplift and continental/fluviolacustrine deposits. Modified from Bouaziz et al. (2002)

4. RESULTS

4.1 INTRODUCTION

The purpose of this chapter is to present and analyse the collected data and observations. First, however, an introduction of the study area will be presented in section 4.2, and includes an overview of the geography, previous works, structural setting and stratigraphy. Subsequently, section 4.3 - Structural Analysis, which represents the main focus of this chapter, will present and describe collected data.

4.2 GEOLOGY OF THE STUDY AREA - JEBEL FADELOUN ANTICLINE

4.2.1 STRUCTURAL OVERVIEW

The study area, Jebel Fadeloun (JF), is located in the northeast Tunisia, 25 km west of Gulf of Hammamet, in the transition zone between the Tunisian Atlas, North-South Axis (NOSA) and Pelagian domains (Figure 4.1). JF is essentially formed by an outcropping anticline; 8 km long, 5 km wide and 350 m.a.s.l. at its highest point. The core of the fold exposes Cretaceous Aptian Limestones, which forms the main attention for this investigation. The published literature concerning the JF is sparse; it is partly described by the French-language PhD thesis of Saadi (1990), who interpreted JF, together with the Jebel Garci and Jebel Mdeker anticlines (see Figure 4.1), to form a northern prolongation of the NOSA. Khomsi et al. (2009) characterised the structural styles in the region, based on seismic sections and wells. They interpreted a regional, buried structure (Kondar, Figure 4.1), oriented NE-SW, which apparently coincides with the JF anticline. Additionally, the JF is included in regional, 1:50 000 scaled, geological map, published by Service Géologique de Tunisie (2003), entitled "Sidi Bou Ali".

Although the JF anticline is situated east of the NOSA, within the lowlands of the Pelagian Platform, the atlassic front looms nearby: Elongated mountains and monumental peaks such as the Jebel Zaghouan reflect a zone of intense deformation, where the regional Zaghouan thrust and the NOSA structure merge, just 25-30 km west of the JF (Khomsi et al., 2009; Dhahri and Boukadi, 2010).

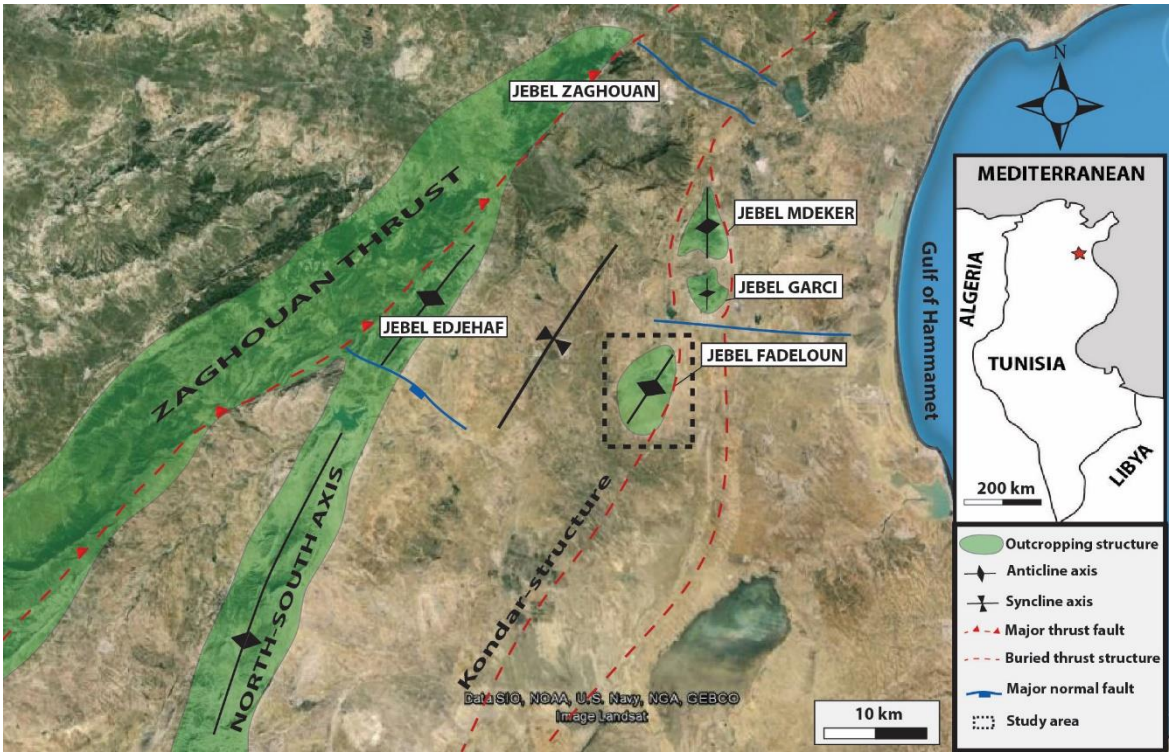

Figure 4.1 - Structural overview of the study area and selected key structures. Satellite image from Google Earth, interpretation based on (Saadi, 1990; Khomsi et al., 2009; Dhahri and Boukadi, 2010). The red star in the inset map marks the location.

Burial-, and deformation depths

Vitrinite reflectance data and fluid inclusions have been sampled and analysed by Cavailhes (2015) in DNO International. Based on these analyses, a maximum burial depth of 2.5-3.5 km can be deduced for the crestal Aptian rocks. In addition, fluid inclusions from calcite mineralisation in the faults and fractures reveal a trapping temperature around 75 ºC. This may suggest a deformation event occurred at 2-3 km depth, assuming a geothermal gradient in the range of 30-40 ºC/km, which is consistent with a regional geothermal study by Dhia (1987).

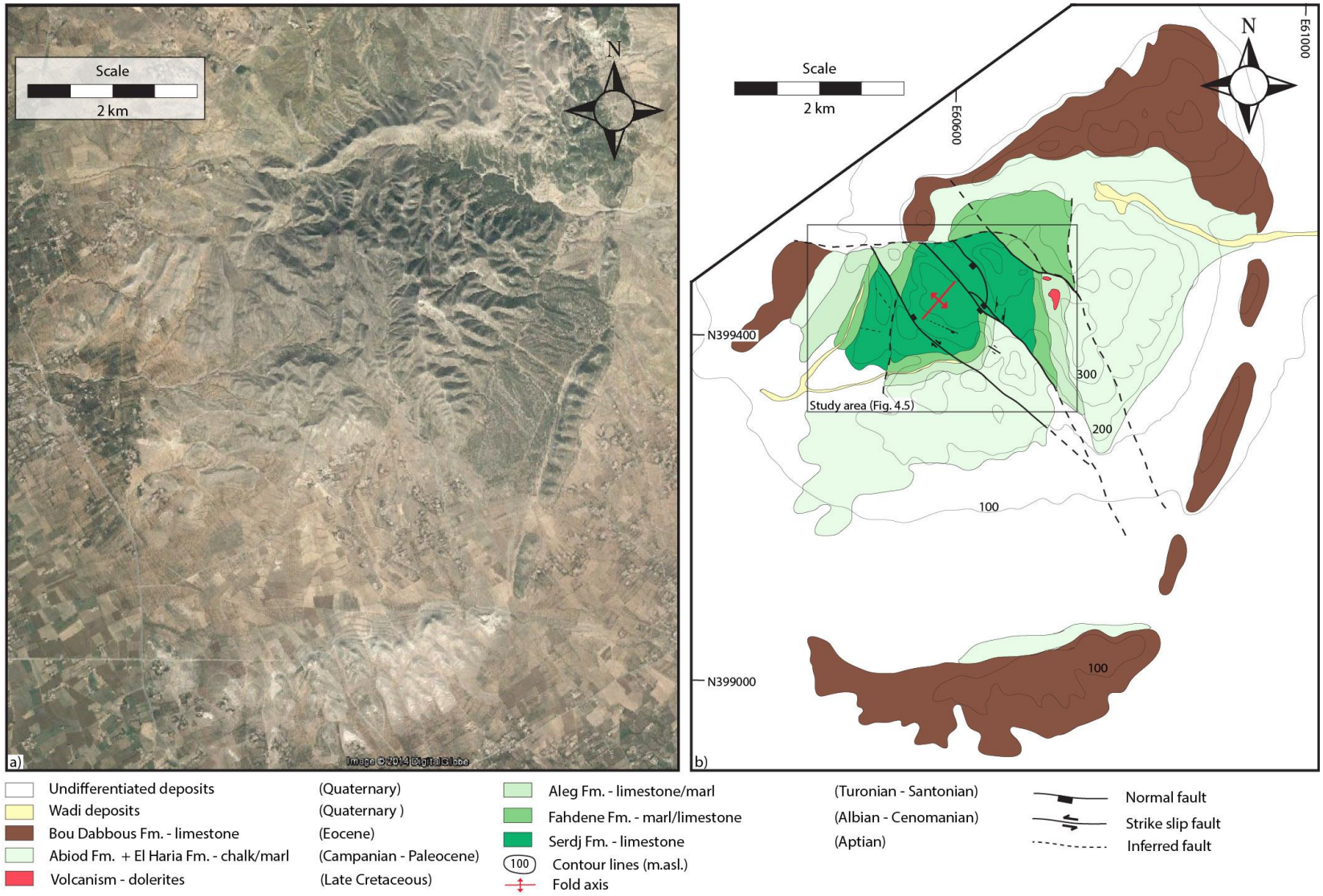

Figure 4.2 – a) Satellite image of Jebel Fadeloun, modified from Google Earth. b) Geological map, based on field observations and a geological map by Rabhi (2003). See Figure 4.1 for regional location. Grid references are in UTM (projection: UTM zone 32N).

4.2.2 STRATIGRAPHIC OVERVIEW

The outcropping stratigraphic column of JF (Figure 4.3) involves lithologies from Aptian (Lower Cretaceous) to Ypresian (Eocene). Our study was limited to the Cretaceous rocks, especially the Aptian of Lower Cretaceous. Therefore, younger lithologies (Paleocene and Eocene) will be given no further emphasis. Based in field observations and published literature, the following formations may be recognised:

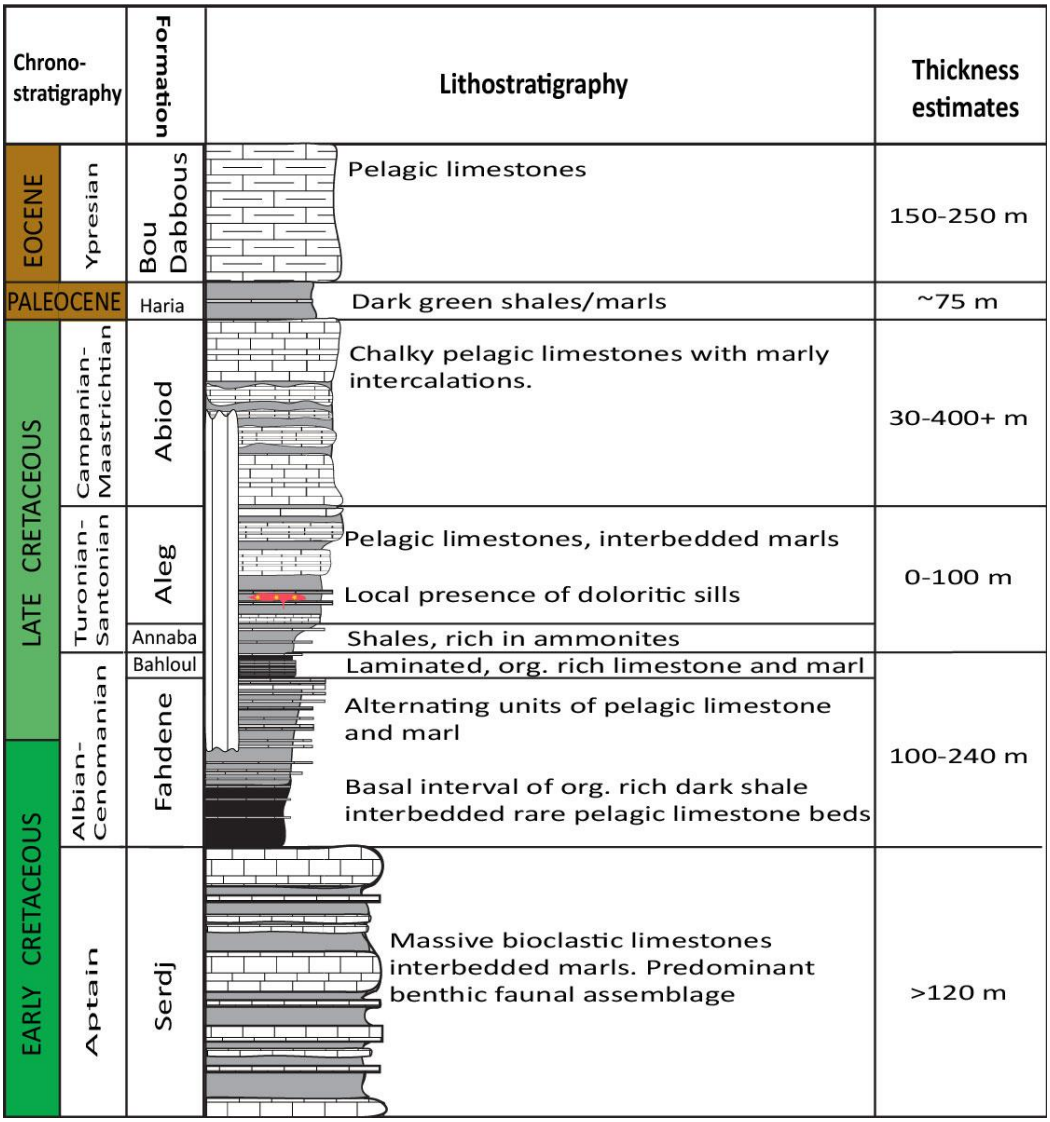

Figure 4.3 - Stratigraphic column of Jebel Fadeloun based on local field observations, general descriptions (Mejri et al., 2006), and written communication with Atef Ben Kahla (DNO Tunisia, 2015). Thickness estimates are derived from the pre-existing geological map, apart from the Serdj Fm. that was manually logged. Note the (i) thickness variations, reflecting lateral differences, (ii) a local hiatus between Fahdene Fm. and Abiod Fm. that can be observed in Figure 4.2 in the northernmost segment of the fold, and (iii) presence of local volcanism.

Aptian "Serdj Formation"

The Serdj Formation is predominantly made up of yellow-brownish to grey, massive limestone beds, varying from wackestone to grainstone texture, and interbedded argillaceous limestones (i.e. marls). Characteristic textures include benthonic foraminifera, bioclasts, and various macrofossils, e.g. bivalves, echinoderms and cephalopods. Recrystallised grains are common, and seen as sparkling faces in freshly cut samples. The textural and faunal assemblages of the Serdj Fm. indicate a carbonate ramp setting, with facies variations between inner-mid ramp (packstone) and outer ramp (wackestone). Detailed logging and sampling of the Serdj formation was performed and its thickness measured to be >120 m (the basal contact was not observed).

Albian - Cenomanian "Fahdene Formation and Bahloul Member"

Erodible marls and pelagic limestones of the Fahdene Formation represents Albian-Cenomanian age, and form a distinct boundary with the underlying Serdj Formation that is easily recognisable in the field. Generally, the limestone:marl ratio increases upwards in the formation and the faunal assemblage includes planktonic foraminifera, ammonites and echinoids. Thinly laminated, dark-grey limestone and marl of the Bahloul Member, form the uppermost unit of the Fahdene Fm and commonly contains high levels of organic matter (Mejri et al., 2006). Generally, a change in the depositional environment can be recognised during the Aptian/Albian transition, from shallow marine platform to open marine facies. According to Mejri et al. (2006), the Fahdene Formation represents a local record of the global Albian Anoxic events.

Turonian-Santonian "Aleg Fm. and Annaba Member"

The Aleg Fm. of Turonian-Santonian age consists of alternating shales and pelagic limestones. A shaley interval, rich in ammonites, represents the basal Annaba Member. The lithology grades upwards to more massive pelagic limestone beds, with intercalations of marls. Dominance of shale and pelagic faunal assemblages suggests an open marine/lower slope environment. Unconformities are regionally known within the Aleg Fm. and at the base of the overlying Abiod Fm., which have been attributed to discrete tectonic movements and halokinesis (e.g. Mejri et al., 2006). A local hiatus between Fahdene Fm. and Abiod Fm. is observed in the northernmost segment of the JF fold and can be seen in Figure 4.2. In addition, localised volcanic bodies are observed within the Aleg Fm. The intrusions follow bed boundaries (sills) and appear conformable deformed (fractured and faulted) with the

surrounding formations. Observations by optical microscopy reveal a medium-grained, doloritic texture, composed of serpentinised olivine, ortho-pyroxene and calcite.

Campanian – Maastrichtian "Abiod Fm"

White-coloured, massive chalky limestone, interbedded marly units, corresponds to the Abiod Formation of Campanian-Maastrichtian age. The chalky beds possess a distinct, brittle character, and commonly subject to denser fracturing, relative to the marl units. There are large thickness contrasts between western and eastern fold limb, as shown in the geological map in Figure 4.2b. Regional studies (e.g. Bey et al., 2012) of the Abiod Fm. have documented fault-related thickness and facies variations, in addition to slumping structures, all suggesting syn-sedimentary tectonic instability (Mejri et al., 2006).

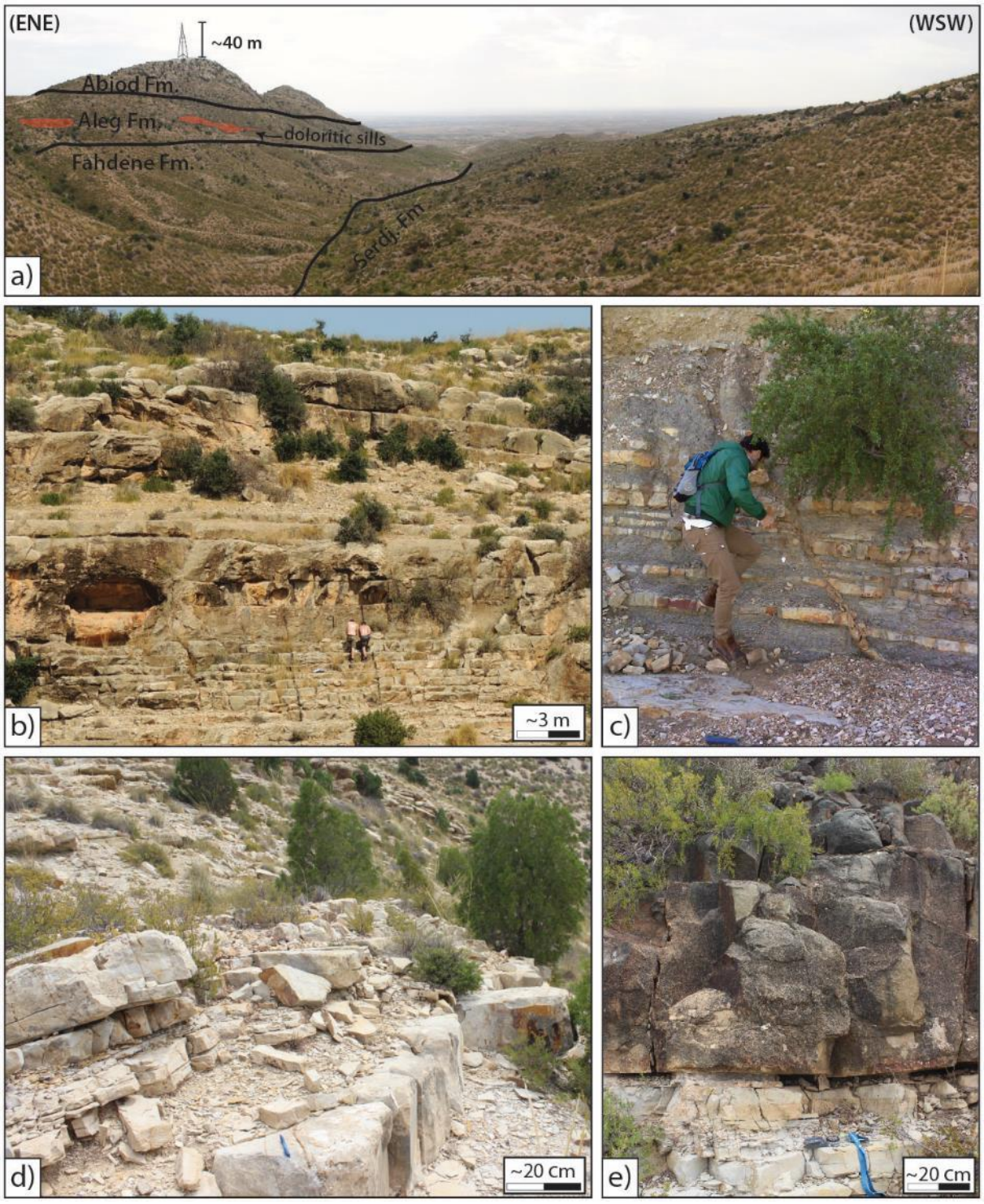

Figure 4.4 - Field expressions of selected formations. (a) Overview of landscape in the eastern fold limb, with annotated stratigraphy. (b) Serdj Fm. of massive, yellowgrey-coloured limestone and minor marl units. (c) Fahdene Fm. organic-rich marl, interbedded minor limestone units. Note the minute fault right of person. The marls of the Fahdene Fm. are highly erodible and commonly reflects incised topography in the field. (d) Photo of the Abiod Fm. showing alternating limestone (chalk) and marl units. (e) Intraformational boundary between Aleg Fm. limestone and doloritic sill.

4.3 STRUCTURAL ANALYSIS

The following sections aim to present and analyse the structural data from the study area. For convenience, the content is arranged in three sections: 1) fold characterisation, 2) faults and fractures characterisation, and 3) microstructural and petrophysical characterisation of fault rock.

4.3.1 FOLD CHARACTERISATION

OUTCROP STUDY

The size of the outcropping fold structure is estimated, by satellite images, to 8 km long and 5 km wide. Several fault sets dissects the fold, as illustrated in the geological map in Figure 4.2. In order to capture the shape of the fold and quality check the pre-existing geological map, measurements were recorded of bedding and fault planes within the entire study area.

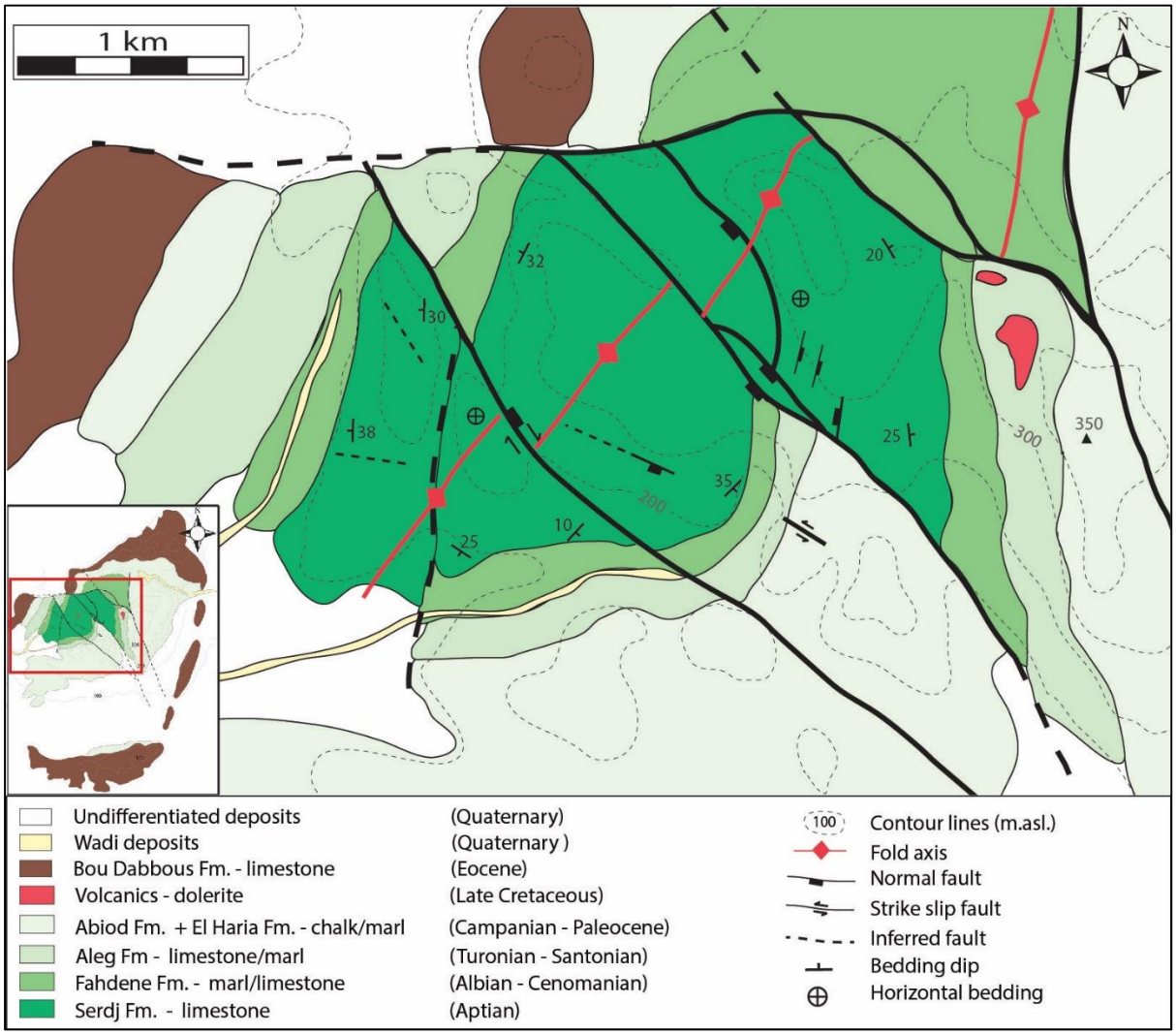

Figure 4.5 – Geological map of the study area, with bedding dip and faults. Notice how the fold axis is oriented NE-SW and coincides with the atlassic trend.

Based on field studies and satellite images, several fold characteristics are observed. The fold axis trend approximately NE-SW, which is illustrated in Figure 4.5. A relatively symmetrical fold-shape is captured by a structural cross section (Figure 4.7a) oriented perpendicular to the fold axis. The western and eastern fold limbs dips, $\leq 32^{\circ}$ and $\leq 35^{\circ}$, respectively, forms an interlimb angle of 113°, which corresponds to an open and upright fold, with an axial plane oriented c. 225/88. A curving of the fold axis can be observed from the fold axis-parallel cross section (Figure 4.7b), suggesting the fold is non-cylindrical, with a four-way dip closure. Numerous faults span across the fold, as illustrated in Figure 4.7b, and results in fold segmentation. The faults show predominantly NW-SE to ESE-WNW trends and normal sense of displacement; however, certain slip surfaces reveal both vertical and subhorizontal lineations. These are interpreted as normal faults with a minor strike-slip component (Figure 4.6b). Further data from fault and fracture characterisation are presented in section 4.3.2.

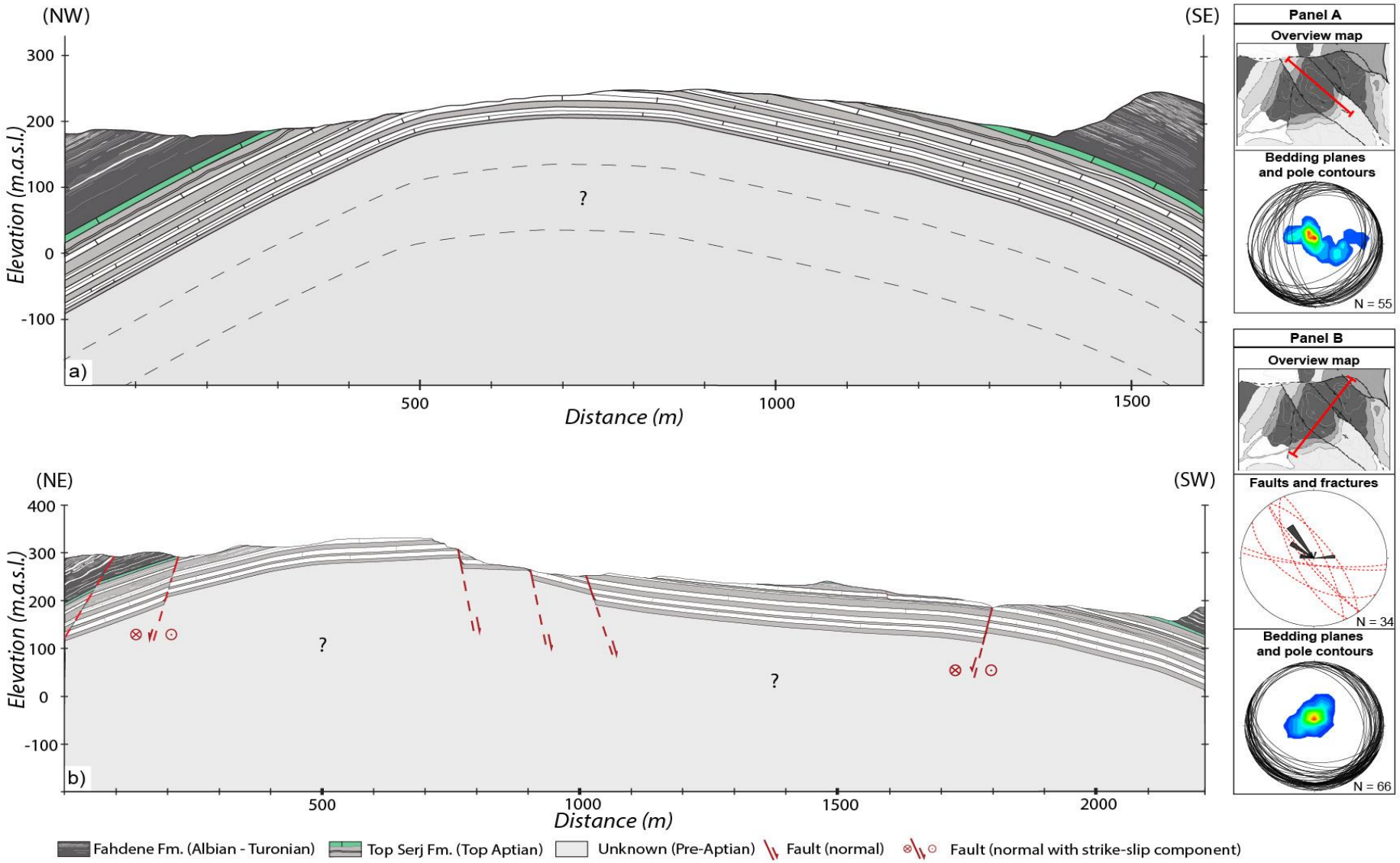

Figure 4.6 – Structural cross sections with corresponding panels showing location and summary measured trends. a) Section oriented perpendicular to the fold axis. Notice the (i) symmetric and open fold geometry, and (ii) absence of faults. Panel A shows location of the section. b) Section oriented along the fold axis. Note the (i) curved fold axis, (ii) dissecting faults, and (iii) predominant fold-perpendicular fault and fracture populations in the stereonet. Stipled great circles corresponds to faults, whereas the half rose diagram illustrates fracture trend distribution.

SEISMIC EXPRESSION

A 2D seismic section (Line 12.15) was interpreted for correlation with the subsurface geology of the study area. In addition to the JF anticline, the section comprises two other large structures, a syncline and a second anticline. As illustrated in Figure 4.7, these structures combined include a variety of features: (i) yellow-blue coloured, strong seismic reflectors, (ii) upward-truncated reflectors, (iii) abruptly terminated/discontinuous reflectors, (iv) imbricated reflectors, (v) local thickening of reflector units, and (vi) steeply dipping reflectors.

The syncline, sited in the western part of the line, have a symmetric and gentle geometry. A strong reflector unit can be recognised, particularly within the syncline, and correlates to the top Bou Dabbous Fm. of Eocene age. The illumination is resulted by the strong impedance contrast between the Bou Dabbous Fm. limestone and the overlaying Souar Fm. shale. Not only does this provide a marker horizon for stratigraphic ties, but it also allows for correlation with outcropping units in the JF. Numerous reflectors truncate upwards in a horizontal reflector above, forming an angular unconformity (Figure 4.7a). Observed discontinuities along reflectors are interpreted as faults, including both normal and reverse sense of slip, demonstrated by a graben-structure and an imbricate stack. The faults occur at various depths and offset different units, located above-, below-, and the Bou Dabbous Fm. itself. Furthermore, extensional faults are not observed above the unconformity. Certain reflector units appear to thicken, away from bounding faults. The broadening seems conformable, and it is difficult observe any onlapping relationship among the reflectors.

The JF anticline, in the centre of Figure 4.7, is characterised by poor seismic illumination that limits the observations within the structure. However, steeply dipping reflectors towards the surface boundary, sketch a relatively symmetric, open fold. Additionally, observations from the western fold limb, near the surface boundary, may indicate the horizontal reflector units above the angular unconformity participate in the folding.

In contrast to the JF anticline, the eastern anticline is well expressed and restricted to the subsurface. The fold has a low amplitude and short wavelength, relative to the JF. A peculiar feature can be observed from the internal fold-domain: the reflectors dip-direction is gradually inversed with depth. Further, the lower interval (dipping westwards) appears to form a wedge-shaped body, which thickens and terminates towards, what is interpreted as, a fault (Figure 4.8).

Interpretations are further discussed in section 5.1.1.

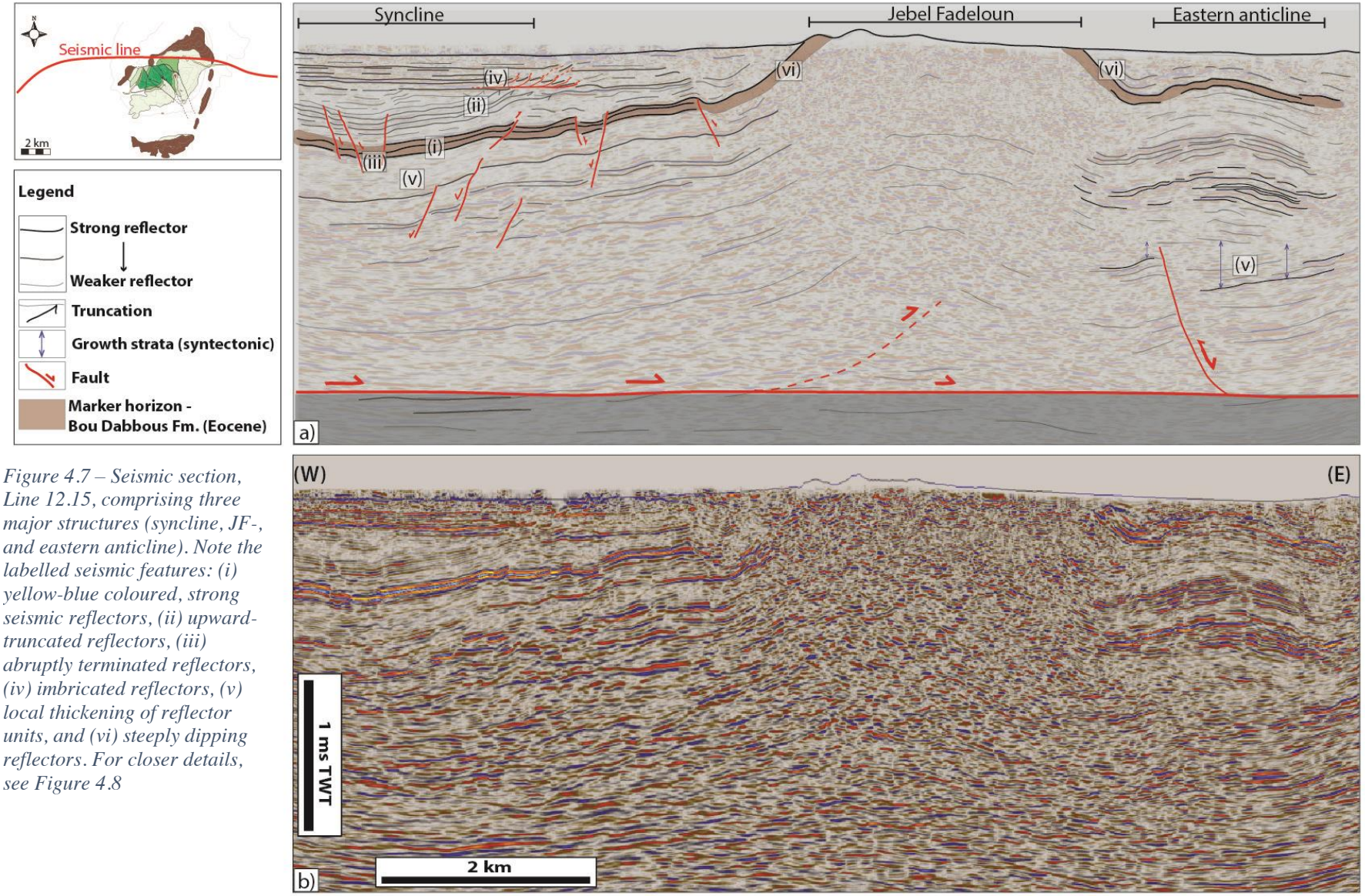

Figure 4.7 – Seismic section, Line 12.15, comprising three major structures (syncline, JF-, and eastern anticline). Note the labelled seismic features: (i) yellow-blue coloured, strong seismic reflectors, (ii) upward-truncated reflectors, (iii) abruptly terminated reflectors, (iv) imbricated reflectors, (v) local thickening of reflector units, and (vi) steeply dipping reflectors. For closer details, see Figure 4.8

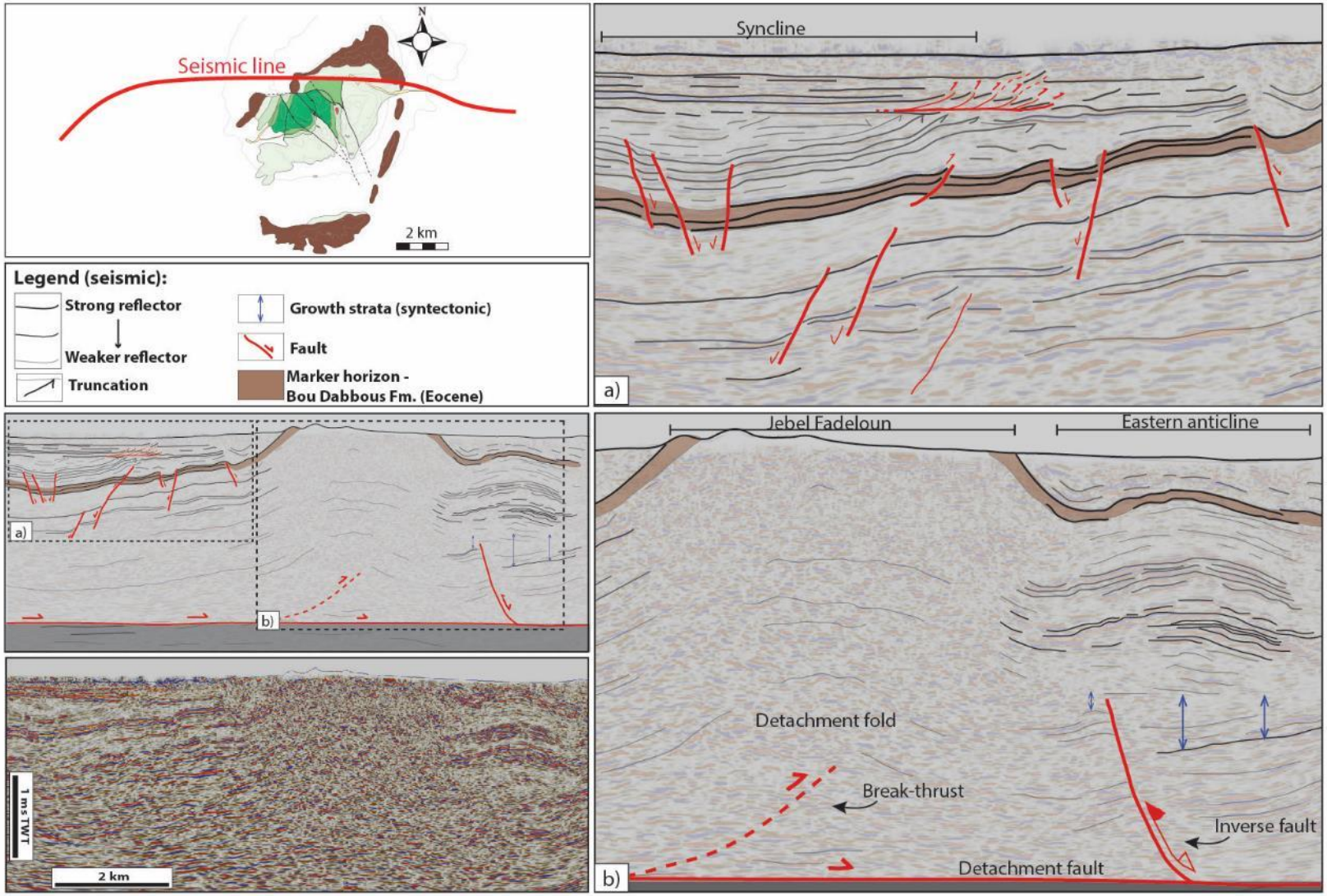

Figure 4.8 – Detailed overview of the observed structural features in Line 12.15. (a) Interpretations from the syncline area, including multiple generations of faults, possible growth strata, truncated reflectors and imbricated stacks. (b) Interpretations of the JF anticline and adjacent, second anticline. Notice the following features: (i) detachment folding of JF, with a possible break-thrust (stipled), and (ii) inverted half-graben anticline with wedge-shaped growth strata.

4.3.2 FAULT AND FRACTURE CHARACTERISATION

The following section presents fault and fracture characteristics from the study area. To begin with, two different fault zones of contrasting displacement magnitudes will be described and analysed. Then, fracture studies from two different localities will assess the background fracturing and present some controlling factors on the fracturing. Key motives are to (1) characterise the fault architecture, (2) establish the kinematics of the faults, (3) characterise the fracture pattern, and (4) investigate mechanical strength properties.

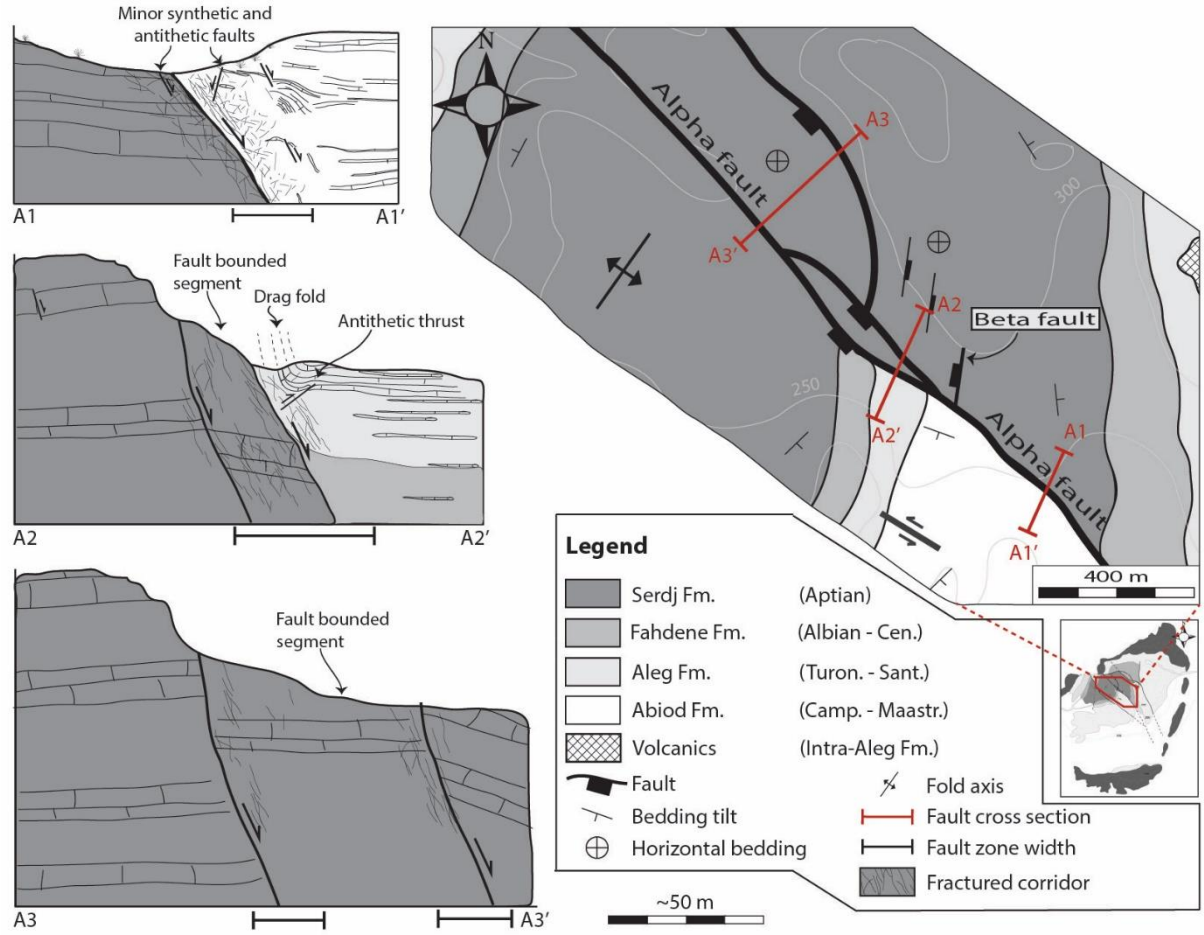

Figure 4.9 – Geological map and simplified fault zone sections. The inset map shows the location, whereas the geological map indicates the positions of (1) the Alpha and Beta faults, and (2) Alpha fault sections A1-A1' to A3-A3'. Notice the following observation along the Alpha fault: (i) fault segmentation in section A2-A2' and A3-A3', (ii) intense fracturing and minor faulting within the fault zones, (iii) intra-Serdj Fm. fault displacement at the fold crest in section A3-A3', (iv) drag fold hangingwall syncline, suggesting normal displacement (A2-A2').

MAJOR FAULT STUDY - LOCALITY "A1"

The A1 locality represents an expression of the Alpha fault; a major normal fault, oriented approximately NE-SW and partly exposed along a c. 2400 m elongated fault trace. As illustrated in Figure 4.9, the Alpha fault is characterised by planar fault surfaces; however, local bends and fault segmentations occur as well. The A1 locality offers partial exposures of both the hangingwall and footwall, and was selected for outcrop analysis to examine the fault architecture.

Overview of the fault zone

The A1 locality includes a c. 20 m wide fault zone, composed of a narrow fault core, sandwiched between damage zones in the hangingwall and the footwall (Figure 4.10a and b). The overall orientation of the primary slip surface is measured to c. 150/60. Quaternary debris and vegetation covers much of the core area, typically reflecting fault-related weak zones prone to weathering and erosion. The footwall consists of massive Serdj Fm. limestone, while the hangingwall comprises alternating chalk and marl units of the Abiod Formation. Juxtaposition of the Serdj Fm. against Abiod Fm. suggests a minimum displacement of 100 m based on the stratigraphic relationship (Figure 4.3). However, as the locality is positioned in the fold limb (illustrated in Figure 4.9), pre-faulting bedding tilt contributes to the resulting juxtaposition. Based on the intra-formational displacement observed at the fold crest (A3 in Figure 4.9), and assuming similar displacement magnitude amongst the A1 and A3 localities, a minimum offset is estimated to c. 50 m.

Fault core

The fault core width varies from 1 to 4 meter and consists of a poorly exposed primary slip surface, surrounded by a zone of intensely deformed fault rocks, i.e. breccia and gouge. Most of the core is confined to the hangingwall side, predominant characterised by fault breccia (Figure 4.11f). The breccia clasts are angular, up to 50 cm in diameter, of hangingwall material, and bound by calcite mineralisation and matrix. Fractures filled with white-to-grey, blocky calcite crystals are abundant within the fault breccia and reach thicknesses up to 20 cm. Additionally, patches of incohesive fault gouge, with foliated fabrics (Figure 4.11e), occur in the immediate vicinity of the primary slip surface. The foliation is measured to sub-vertical and fault-parallel orientation. Microscopic analyses of various fault rocks are presented in section 4.3.3.

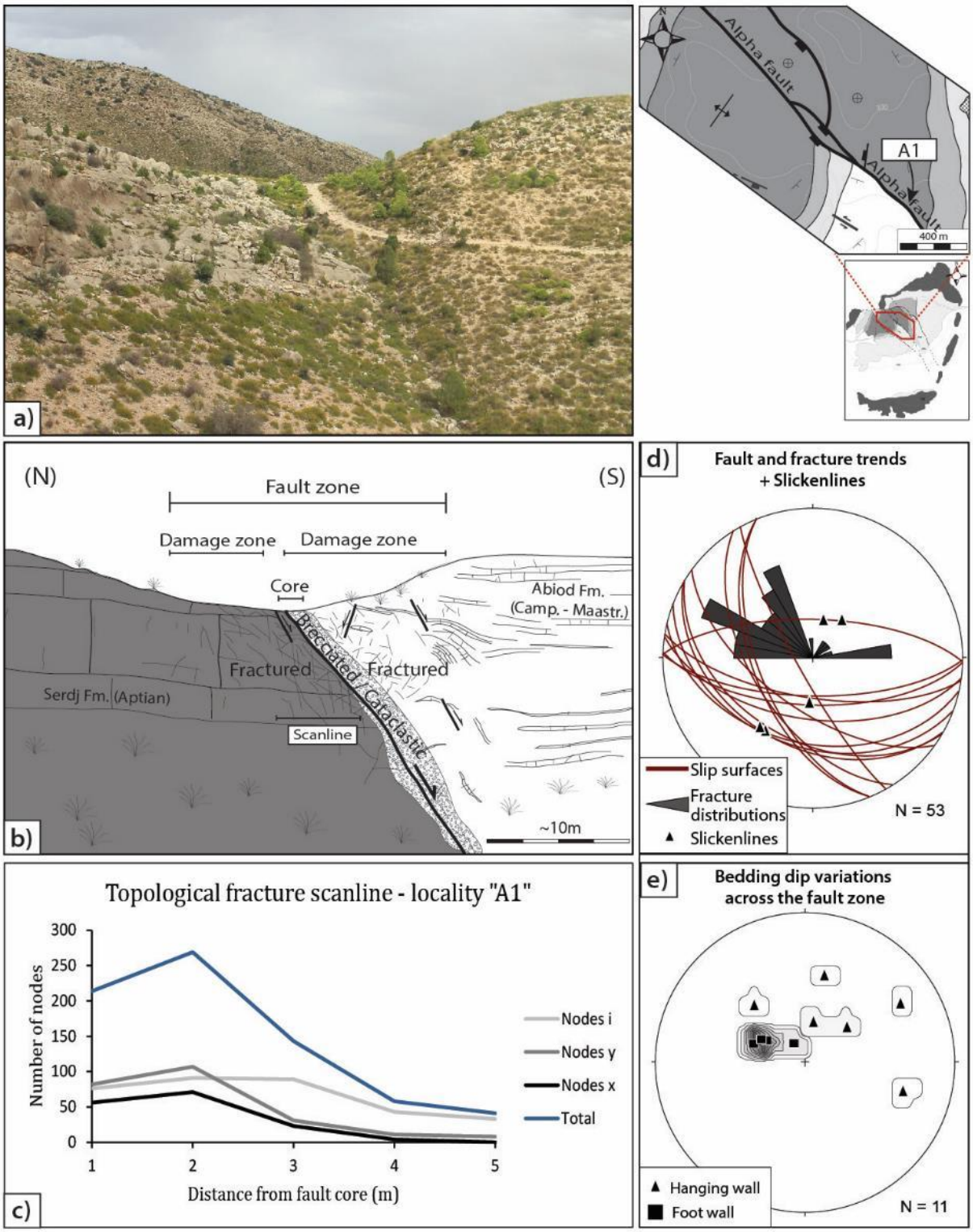

Figure 4.10 – Alpha fault, A1 locality. (a) Photograph of the fault zone. (b) Observed structures and fault architecture. (c) Plot of the topological fracture scanline from the footwall damage zone. Note that X-, and Y-nodes, i.e. connected fractures, decrease with distance from the core. (d) Fracture and fault trends with slickenlines. Notice (i) both the fracture and fault trends range from E-W to NNW-SSE, and (ii) slickenlines reflect dip-slip sense. (e) Bedding dip variations, plotted as poles, across the fault zone. Note the scattered hangingwall records, whereas the footwall dips are gathered.

Damage zones

Two opposed damage zones of different host rock may be recognised in the fault zone: The footwall damage zone (FWDZ) includes massive, meter-scale thick limestone beds of Serdj formation. In contrast, the hangingwall damage zones (HWDZ) comprises decimeter-scale units of alternating limestone and marl.

Footwall damage zone (FWDZ)

The FWDZ is characterised by intense, anastomosing fracture sets in the inner zone proximate to the core, followed by reduced fracture frequency and connectivity away from the core (reflected by the scanline in Figure 4.10c). A variety of fracture patterns are recorded, however, the predominant trends are parallel and sub-parallel to the fault (Figure 4.10d). Joint, veins and shear fractures occur, differentiated by the latter's visible shear displacement. The fractures are mostly calcite cemented, rarely unfilled, 1-20 mm wide and cm to meter-scale long. In general, the fracture lengths appears to increase with distance from the core, i.e. the contrary to the fracture frequency (Figure 4.10c). Interestingly, fractures with rusty (hematite) cement are also observed, and commonly oriented sub-perpendicular to main fracture sets (Figure 4.11b). These are interpreted as pressure solution seams, i.e. stylolites. Calcite coated slip surfaces and associated lineations are recognised as growth fibers and fault groove marks, i.e. slickenlines (Figure 4.11a). In addition, arrays of parallel, overlapping veins, trending sub-perpendicular to the fault, are recognised as en échelon tension gashes (Figure 4.11d). The gashes can be used to indicate the sense of shear, which in this case suggest NE-SW oriented σ1, and corresponding dextral shear oriented c. N-S.

A fracture corridor (Figure 4.11c), 20-50 cm wide and >10 m long, is situated distally in the FWDZ. The fractures trend fault-parallel and contrasts with the surroundings both in terms of size and texture. The corridor includes two types of fracture characteristics: (1) 1-20 mm thick fractures, filled by blocky calcite mineralisation, and (2) 20-300 mm wide fractures, with a two-component infill consisting of (i) marginal blocky/laminated calcite, and (ii) angular fragments bounded by a beige-coloured, fine-grained calcite matrix. The absence of apparent slip displacement, along with angular clasts in the matrix-composed centre, may indicate hydraulic brecciation.

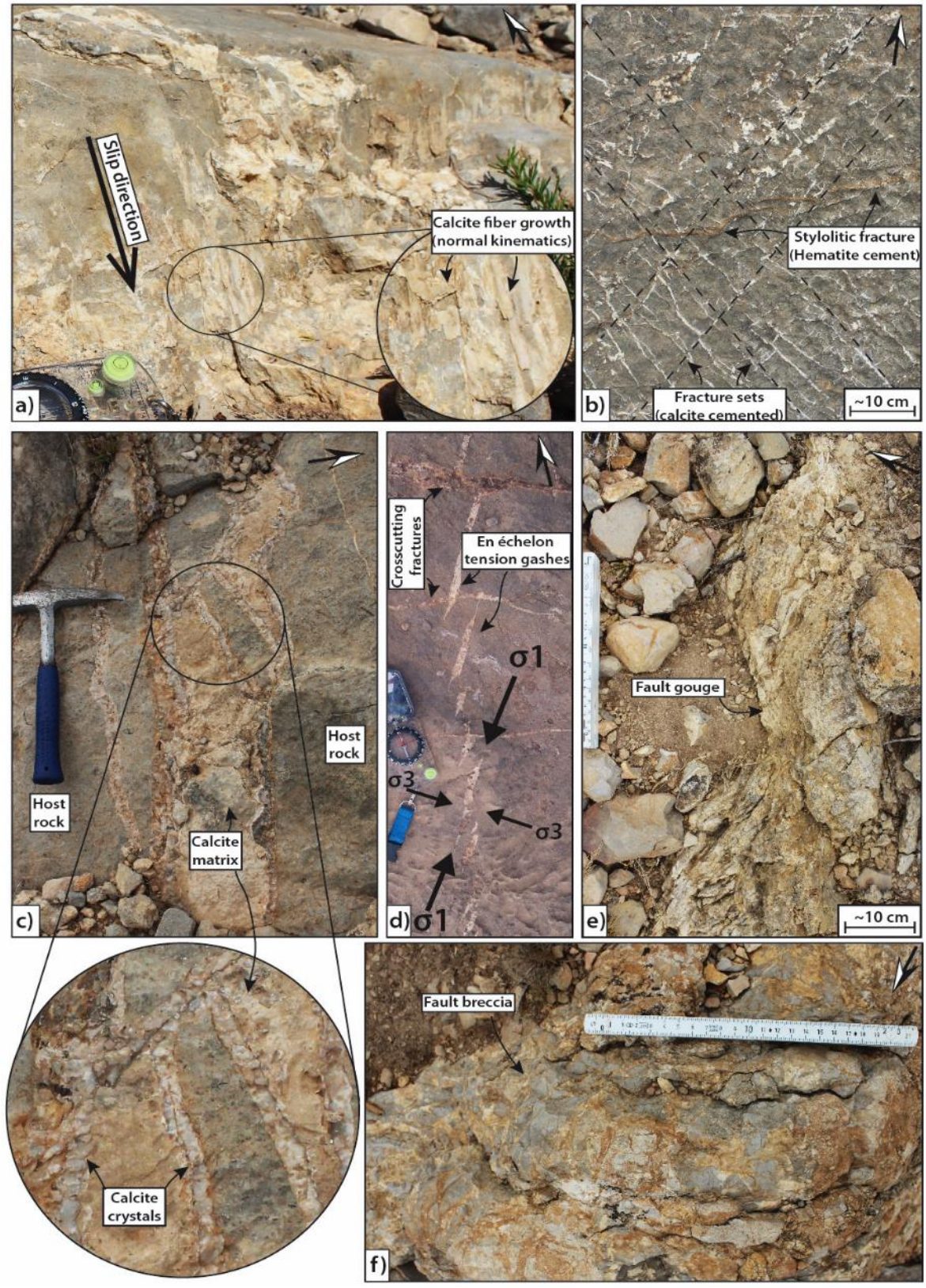

Figure 4.11 - Expressions of deformation structures in the Alpha fault zone. Right-corner arrow indicates north (a) Secondary slip surface with syn-kinematic calcite growth mineralisation. (b) Intense fracture networks in the core/damage zone boundary. Irregular, hematite filled fractures are interpreted as pressure solution seams. (c)

Fracture corridor in the distal FWDZ, hosting a two-component infill: fibrous/laminated calcite and matrix in the centre. (d) En echelon arranged, tensional fractures in the FWDZ, indicating local dextral kinematics. (e) Fault gouge in the core. Note the foliation and poorly consolidation. (f) Clast-, to matrix-supported fault breccia in the core domain. Notice the angular clasts (hangingwall material), bounded by sparry calcite.

Hangingwall damage zone (HWDZ)

The HWDZ is severely crushed and largely covered by debris, which limits quantitative measurements. Generally, fractured and discontinuous blocks of hangingwall material, up to 50 cm in diameter, dominates the proximal damage zone. In addition, minor faults occur, trending both parallel and perpendicular to the primary fault. The distal HWDZ is characterised by fractured, yet continuous beds. Fractures are largely bed bound (some cross cutting) and filled with calcite or iron oxide cement. Overall, the hangingwall bed-geometries show a higher degree of fault-related deformation compared to those of the footwall, as illustrated in Figure 4.10e.

Fault trace

As illustrated in Figure 4.9, the Alpha Fault spans across the study area, and can be traced north-westwards from locality A1, to the A2 site (Figure 4.12). A complex pattern is recognised from the A2 outcrop, as the fault splits into two branching segments. Minor faulting, with offsets estimated to less than 1 meter, can be observed in the footwall, trending perpendicular to the Alpha fault. Some of the hangingwall units are oriented parallel with the fault plane, forming a syncline structure that straightens away from the fault (Figure 4.12c). A local discontinuity within the syncline, accompanied by locally folded units above, suggests the presence some internal faulting (Figure 4.12c). As annotated in Figure 4.12, the hangingwall syncline is interpreted as a drag fold, with an internal antithetic thrust fault, both resulted by normal fault displacement. Also, one could speculate in a clay smear controlled drag folding (e.g. Færseth, 2006), considering the high clay content of Fahdene Fm. (section 4.2.2) in the downfaulted block.

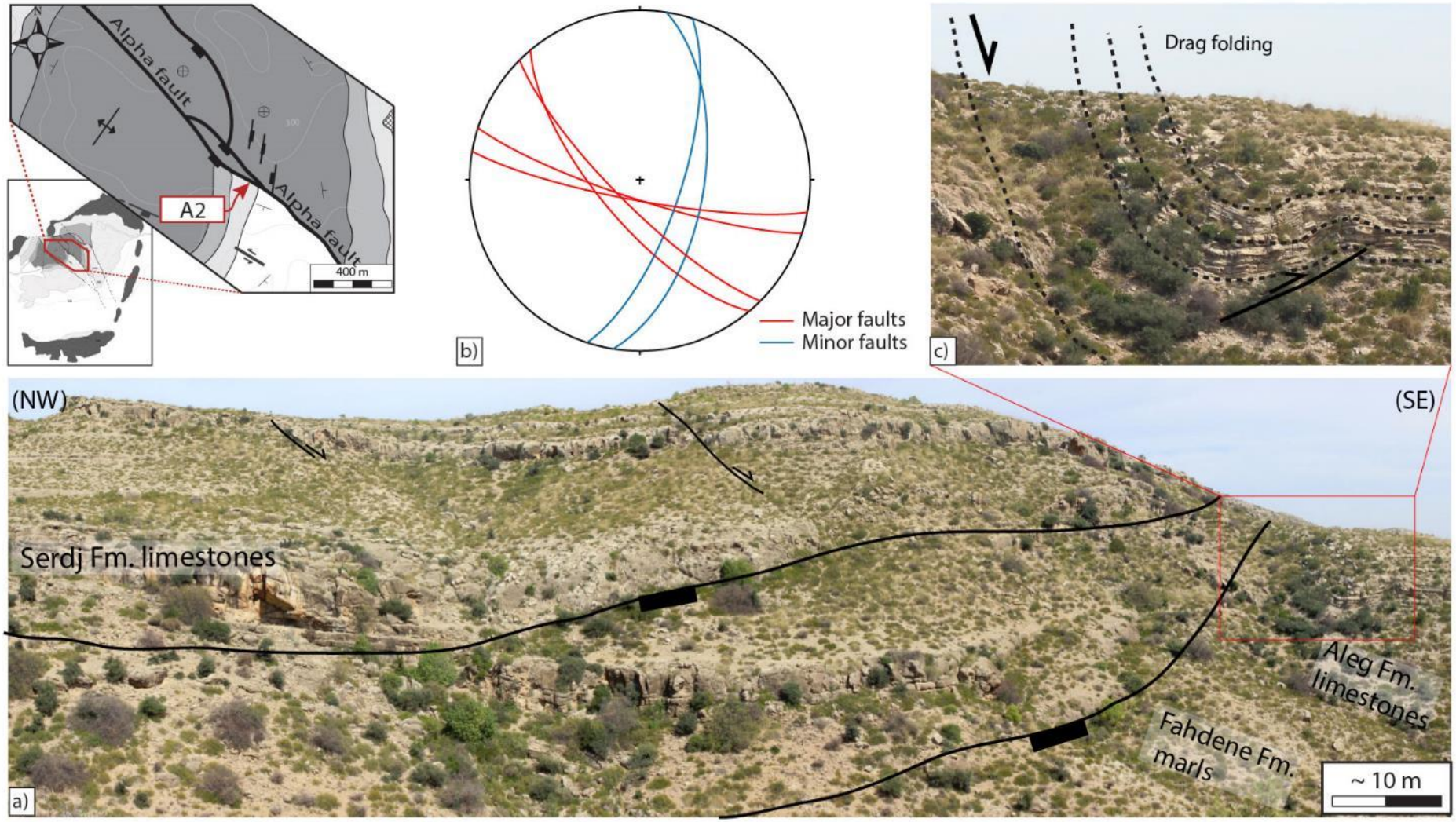

Figure 4.12 – Alpha fault, A2 site from Figure 4.9. a) Overview photo. Notice (i) fault segmentation, (ii) minor faults in the footwall, and (iii) drag folding of the hangingwall. b) Illustrative plot of the predominant fault trends. c) Detailed photo of the hangingwall drag folding. Note the minor, antithetic thrust.

MINOR FAULT STUDY - LOCALITY "BETA"

Situated c. 50 meters north of Alpha, the Beta locality (Figure 4.13a) consists of a normal fault oriented sub-perpendicular to the Alpha fault. The Beta fault extends over c. 50 meters, trends 190/68, and includes a well-defined marker bed that shows an offset (*d*) of 6 meters and normal sense of slip. Measured fault zone width varies from 6 to 10 m and narrows upslope along the fault strike. A curved, roll-over geometry may be recognised from the hangingwall block. The primary slip surface is largely eroded and covered by debris; however, a secondary slip surface (*d≤ 2 m)* is preserved and forms the boundary between the core and the hangingwall damage zone. In terms of fault domains, the Beta Fault shows lack of core-diagnostic fault rocks. Hence, the fault architecture (Figure 4.13b) is described by a centred intensely deformed damage zone (IDDZ), successively bounded by weakly deformed damage zones (WDDZ), *sensu* Micarelli et al. (2006).

Intensely deformed damage zone (IDDZ)

The IDDZ ranges in width from 2 to 4 meters, confined by the primary slip surface and the secondary slip surface (SSS), and characterised by highly connected fracture networks. Localised deformation, i.e. fragmentation, mineralisation and slip surface-parallel foliation, occur in the SSS and extend c. 10 cm to each side. The offset of the SSS is estimated to 1-2 meters. Fracture sets are predominantly short (5-20 cm) and narrow (2-20mm), trending sub-parallel to perpendicular to the fault plane and calcite cemented, partly open or open. Additionally, iron contaminations (red coloured calcite) and hematite cement occur frequently in the fracture fill. Sets of large, fault-perpendicular fractures span from the IDDZ and several meters into the footwall WDDZ. These are up to 200 mm wide and feature the same two-component infill as described in the abnormal fracture corridor in the distal Alpha footwall.

Weakly deformed damage zone (WDDZ)

The WDDZ extends approximately 2-4 m to each side of the IDDZ. Observations suggest that the hangingwall WDDZ is slightly less damaged than the footwall, which hosts the previously mentioned series of large, fault-perpendicular fractures. However, a contrast is noticed in the hangingwall, between the massive (4m thick) marker bed and the overlaying (0.4m thick) bed, where the latter appears more fractured (Figure 4.14e). In general, both fracture frequency and fracture connectivity decline distally from the fault. The predominant fracture population trends sub-perpendicular to the fault plane (Figure 4.13d), and occasionally arranged in an *en échelon* pattern.

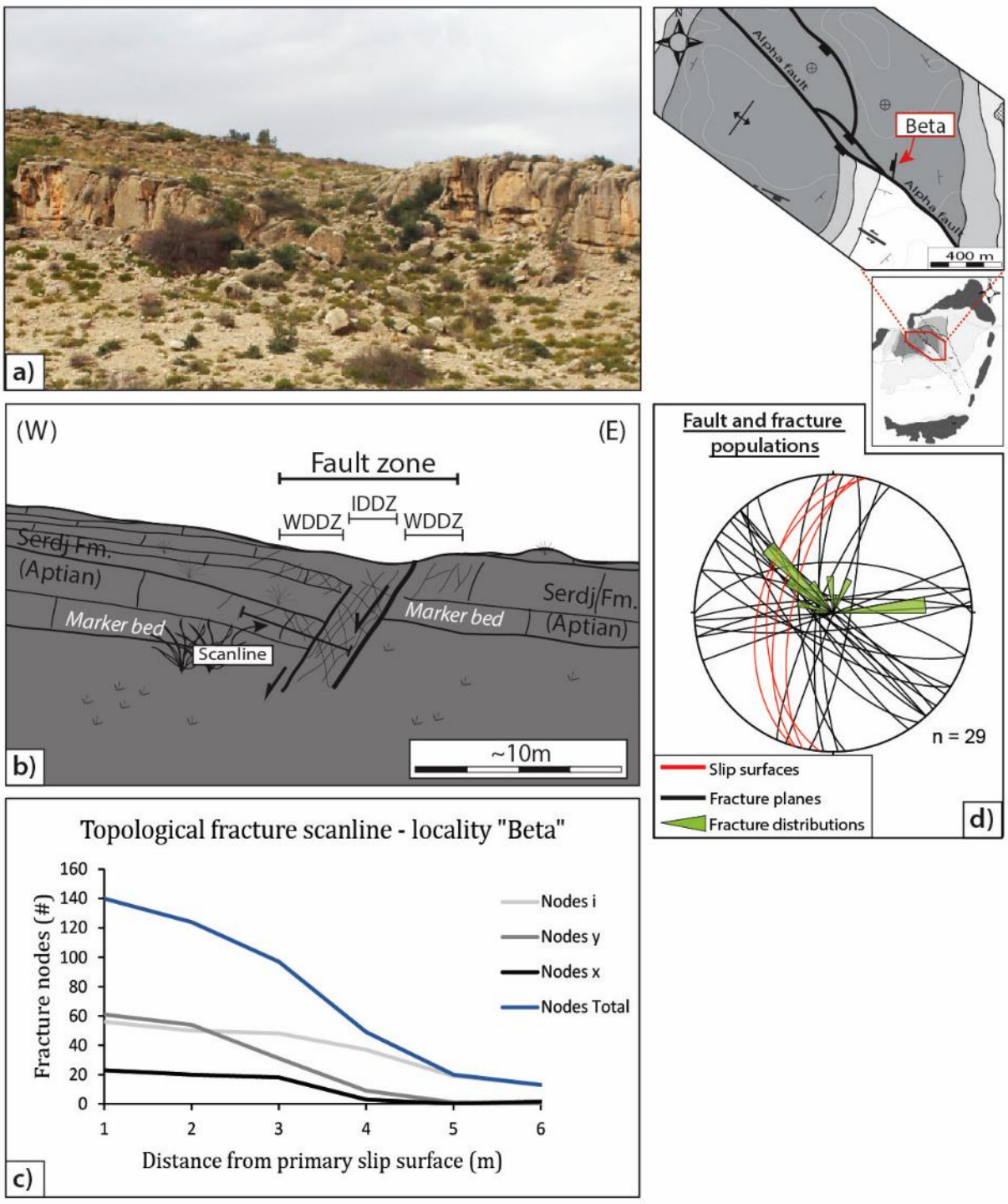

Figure 4.13 – Overview of Beta fault. (a) Photograph of the fault zone. Notice the curved hangingwall geometry (b) Observed structures and interpreted fault architecture. The IDDZ is bounded by a primary-, and secondary slip surface. (c) Plot of the topological scanline in the hangingwall damage zone. (d) Stereoplot of fault and fracture populations. Note that the predominant fracture sets are oriented sub-, perpendicular to the fault plane. IDDZ; intensely deformed damage zone, WDDZ; weakly deformed damage zone.

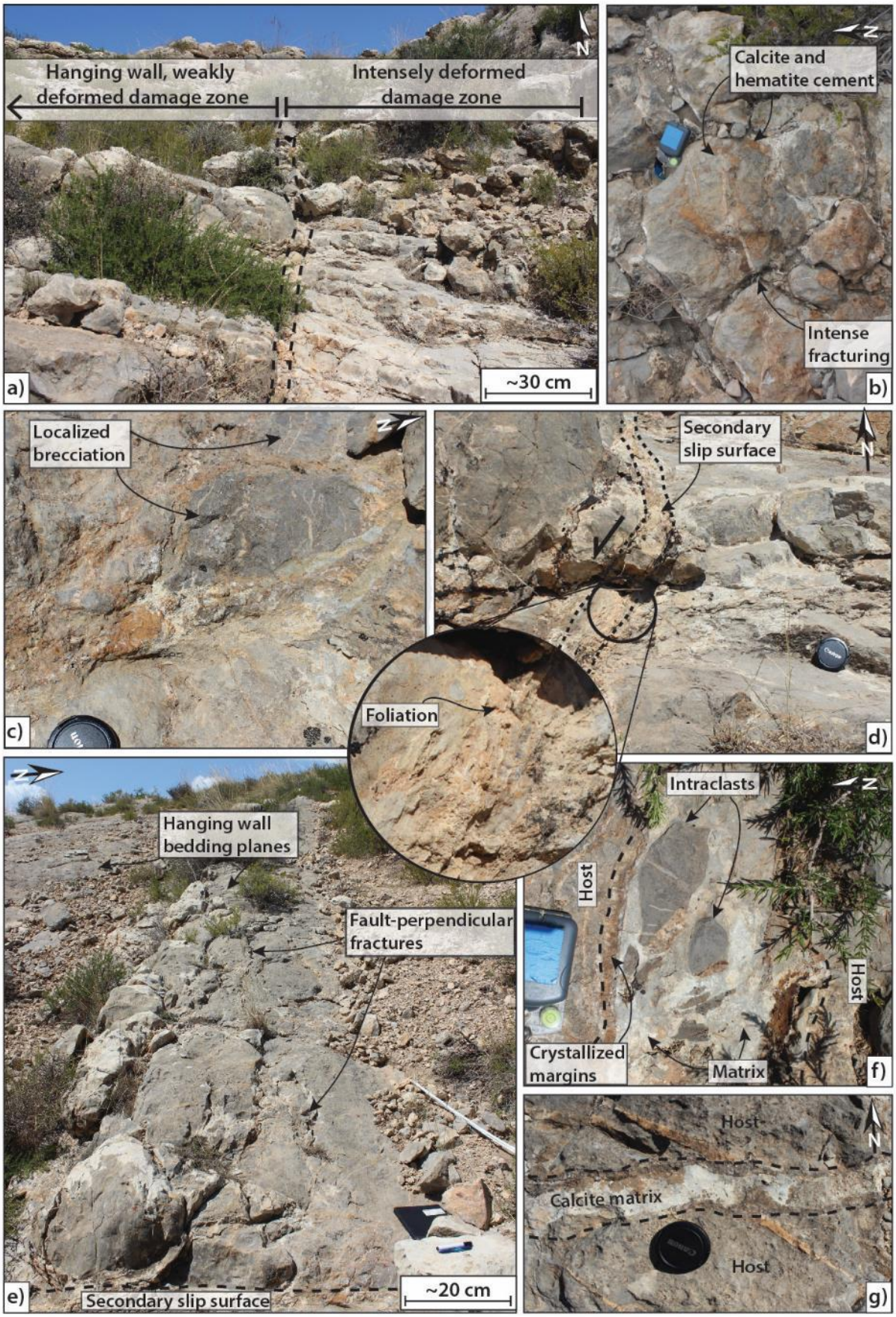
Hanging wall, weakly deformed damage zone
Intensely deformed damage zone
N
~30 cm
a)
Calcite and hematite cement
Intense fracturing
b)
Localized brecciation
c)
Secondary slip surface
d)
Foliation
Hanging wall bedding planes
Fault-perpendicular fractures
Secondary slip surface
~20 cm
e)
Intraclasts
Host
Host
Crystallized margins
Matrix
f)
Host
Calcite matrix
Host
g)

Figure 4.14 – Deformational expressions from the Beta fault. (a) Overview of contrasting deformation domains: the highly fractured IDDZ and the less deformed WDDZ (hangingwall), separated by a (stippled) secondary slip surfaces. (b) Anastomosing, calcite and hematite cemented, fracture networks in the IDDZ. (c) Localised brecciation, confined to a 20 cm wide zone around the secondary slip surface. (d) Secondary slip surface with slip-parallel oriented foliation, consisting of sparry calcite mineralisation, fragments and fine-grained matrix. (e) Overview of the hangingwall WDDZ. The deformation is minute, still some fracture sets occur, predominant fault-perpendicular oriented. (f)-(g) Hydraulic fractures in the footwall WDDZ, oriented fault-perpendicular and several meters in length. Notice the presence of matrix-supported clasts with intragranular veins in (f).

FRACTURE FREQUENCY AND CONNECTIVITY

As expressed in Figure 4.10c and Figure 4.13c, the fault-related fracture networks were recored as nodes by the use of topological scanlines (section 1.4). These values can be presented in ternary diagrams, to illustrate the connectivity variation along scanlines (Figure 4.15). The recorded nodes represents an areal frequency (m^2) that can be converted, via geometrical relationships, to linear frequency (m), as plotted in Figure 4.16.

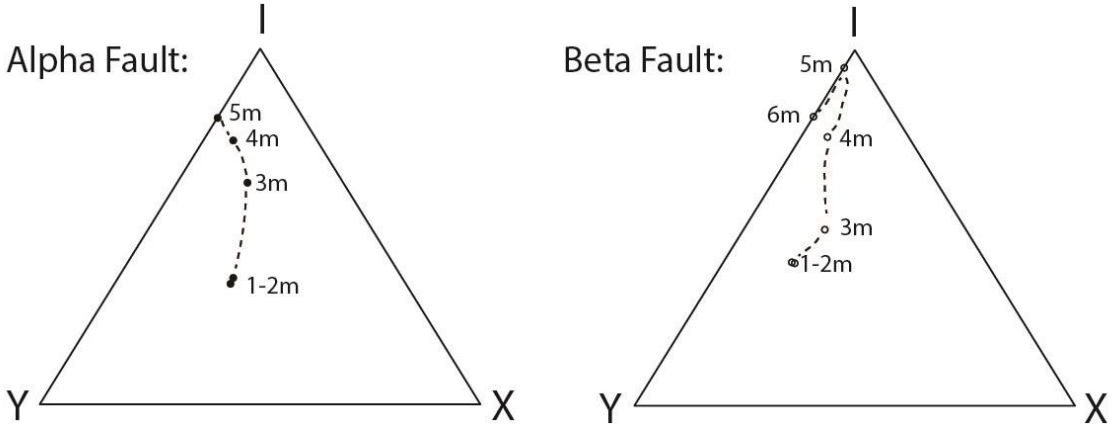

Figure 4.15 – Ternary diagram presenting the proportions of I-, Y-, and X-nodes from topological fracture analysis of the fault zones. The plot illustrates the connectivity profile, marked with the distance from the fault core. Note that the fracture connectivity generally decreases away from the core, i.e. approaches the I-node corner.

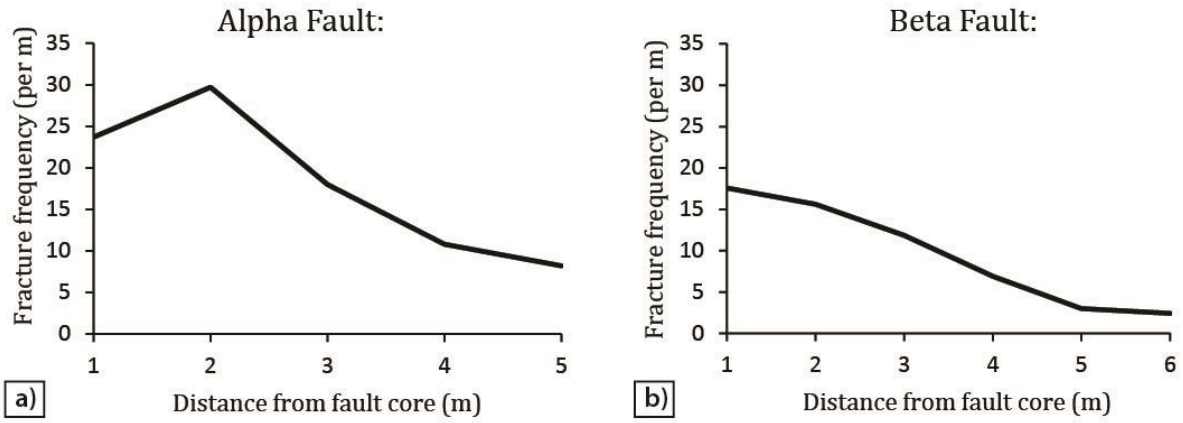

Figure 4.16 – Plot of fracture frequency vs. distance. a) Fracture frequency in the Alpha Fault FWDZ. b) Fracture frequency in the Beta Fault HWDZ.

MECHANICAL STRENGTH PROFILES

Fault zones are commonly associated with anomalous mechanical strengths, relative to the host rock. To test this characteristic, a manual rebound hammer was utilised to record mechanical strength profiles (Figure 4.17a-b) across both the A1 and Beta fault zones.

As illustrated in Figure 4.17, the resulting profiles show a strength weakening trend in the central domain of the faults. Particular high contrasts are recognised from the Alpha profile, where the host rock/core ratio is ≤ 9. Likewise, the Beta profile display an overall strength reduction in the centre region. Yet, the strength contrast is smaller (≤ 3) and only a third compared to the Alpha.

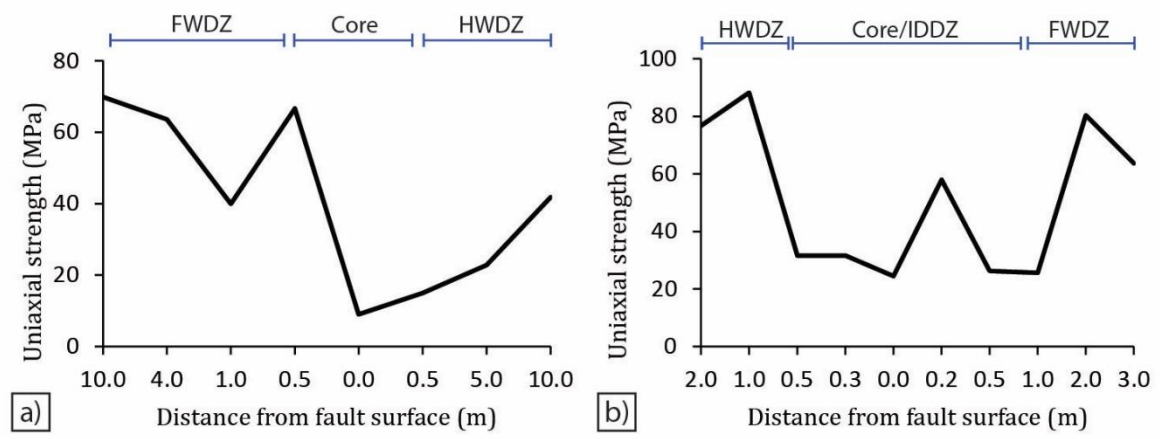

Figure 4.17 – Mechanical strength profiles across the examined fault zones. Notice the annotated fault domains. a) Alpha Fault zone: a significant strength reduction is observed in the core of the Alpha fault. The strength increases away from the core. b) Beta fault zone: the strength profile displays a noteworthy strength weakening in the IDDZ, relative to the surrounding rocks. FWDZ, Footwall damage zone; HWDZ, Hangingwall damage zone; IDDZ, Intensely deformed damage zone (equivalent to core).

SUMMARY AND PRELIMINARY INTERPRETATIONS OF THE FAULT CHARACTERISATION

Key observations from the two fault zones are summarised and presented in Table 4.1 below. Regarding the fault zone architecture, observations from the A1 locality (Figure 4.10b) correlate with the conceptual model of Caine et al. (1996), where strain-contrasting domains are represented by a core and flanking damage zones. Characteristic observations include core-confined fault breccia and gouge (Figure 4.11e-f), and largely intact beddings in the damage zones, with intensified fracturing towards the core (Figure 4.16a) By comparison, the Beta Fault shows similar fracture and connectivity profiles (Figure 4.15b and Figure 4.16b). However, the fault architecture diverge from the A1: fault rocks are nearly absent, and thus a different classification is proposed for the Beta Fault (Figure 4.13b), where the core-term is substituted with an intensely deformed damage zone (IDDZ). It is interpreted that the difference in fault architecture is due to the contrast of displacement-magnitude.

The observed micro-kinematic indicators may reflect the larger-scale fault kinematic. For instance, fault-trend-perpendicular slickenlines, as recorded at the A1 locality (Figure 4.10d), suggests dip-slip movement. Likewise, syn-faulting crystal growth fiber, e.g. Figure 4.11a, can indicate the slip direction, in this case supporting normal movement. The normal sense of slip suggested by micro-tectonic observations is also consistent with larger-scale observations along the Alpha fault, e.g. cross-fault juxtaposed older and younger rocks in respectively footwall and hangingwall (Figure 4.9, A1 and A2), and drag folding of hangingwall units (A2 in Figure 4.9 and Figure 4.12). As described, tensional gashes reflect dextral shear with a NE-SW oriented σ1, which neither fits the regional, NW-SE-directed, atlassic stress, nor stress states compatible with the faults. It is thus likely that the gashes originated from a different event, apart from the folding and faulting. Mechanical profiles shows strength weakening in core-regions. Yet, the Alpha profile display more asymmetry: HWDZ appears weaker, relative to the FWDZ, which may be attributed to differences in deformation, or lithology.

Table 4.1 - Summary of fault characterizations from the investigated fault zones

	Major Normal Fault	Minor Normal Fault
Fault name	Alpha Fault (A1)	Beta Fault
Fault plane orientation	NW-SE to E-W (150/60 - 092/84)	N-S (190/68)
Displacement	> 50 m	6 m
Fault zone width	20 - 50 m	6 - 10 m
Fault zone length	2400 m	< 100 m
Lithology (footwall)	Bioclastic packstone	Bioclastic packstone
Bed thicknesses (footwall)	0.5 - 4 m	2 - 4 m
Lithology (hangingwall)	Pelagic wackstone and marl	Bioclastic packstone
Bed thicknesses (hangingwall)	0.1 - 1 m	0.4 - 4 m
Fault zone architecture	Fault core + Damage zones	Intensely deformed damage zone (IDDZ) + weakly deformed damage zones (WDDZ)
Damage zone fabric	Fractures (joints and veins) + secondary slip surfaces + pressure solution seams + hydraulic breccia	Fractures (joints and veins) + hydraulic breccia
Core fabric	Primary slip surface (covered) + fault breccia and foliated gouge + fractures + calcite mineralization	N/A
IDDZ fabric	N/A	Primary slip surface (covered) + secondary slip surfaces (foliated fabrics and localized brecciation) + fractures
Fracture trends (in order of abundance)	NW-SE, NNW-SSE, E-W	NW-SE, E-W, N-S
Fracture trends (with respect to fault plane)	Parallel, sub-parallel, sub-perpendicular	Sub-perpendicular, perpendicular, parallel
Fracture frequency (per meter)	10 - 30	3 - 17
Mechanical strength ratio (Host rock/Core)	≤ 9	≤ 3

BACKGROUND FRACTURING – LOCALITY DELTA

In order to characterise the background fracturing, a remote site was selected, distant from any faults. The Delta locality, positioned 200 meters south of the Alpha fault, features a well-exposed bedding plane that comprises sub-orthogonal joint sets, and outcrops along a slope of c. 250 m extent (Figure 4.18a). The joint sets (S1 and S2) are orthogonally arranged NW-SE and NE-SW (Figure 4.18d), with an average fracturing frequency recorded at 1 fracture per meter, and a corresponding average aperture of 10-16 cm (see Figure 4.18b-c).

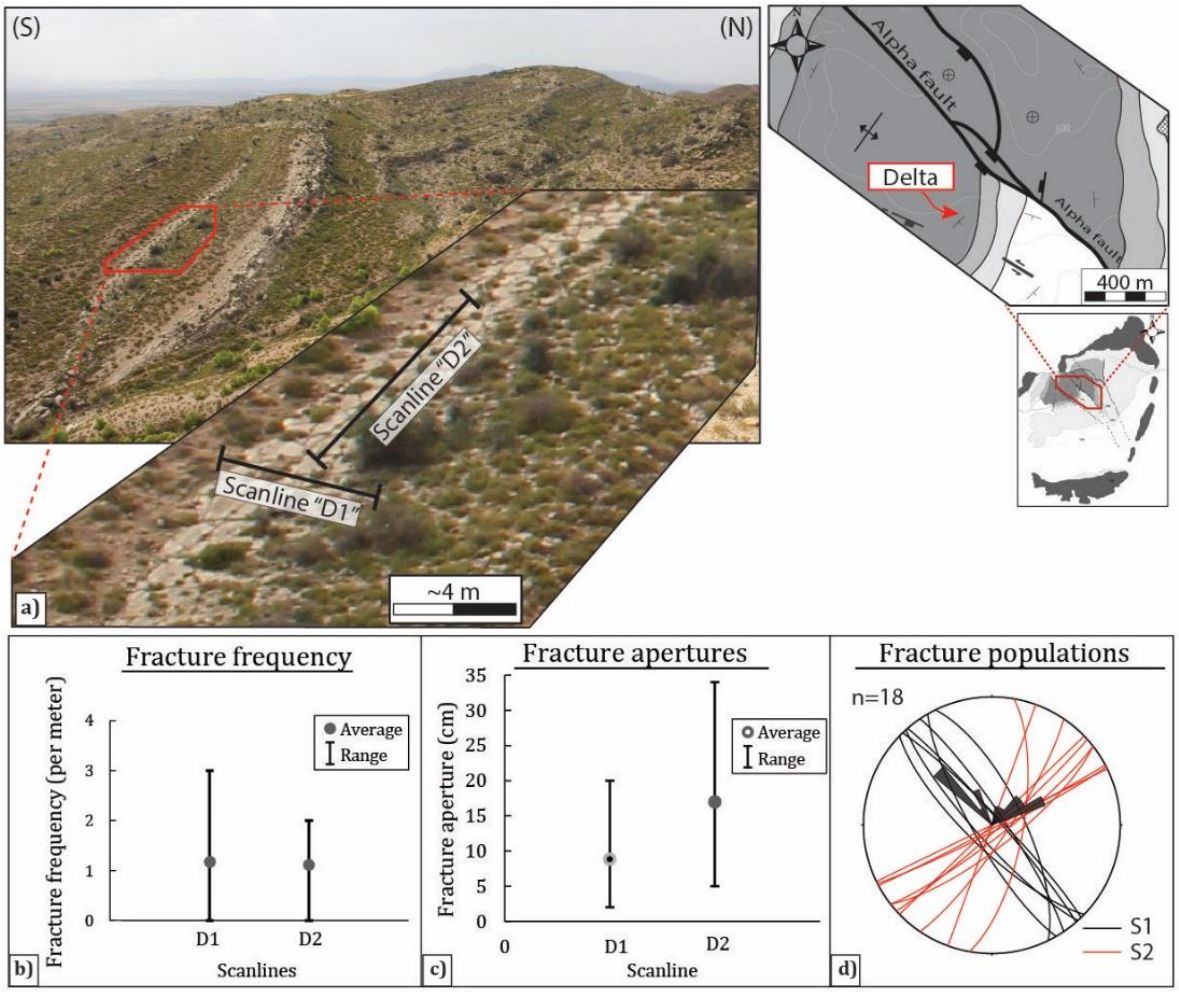

Figure 4.18 – Overview of the background fracture data from locality Delta. (a) Photo of locality with locations of scanline D1 and D2. The fractures are characterised as wide (≤ 40 cm) and long (>> 1m), and tensile. (b) Plot of the fracture frequencies. Notice that both scanlines have an average of c. 1 fracture per m. (c) Plot showing the recorded fractures and corresponding apertures (opening-space). (d) Stereoplot of the fractures reveals sub-orthogonally oriented fracture sets.

MECHANICAL STRENGTH CONTROLS ON FRACTURE PATTERNS - LOCALITY CHARLIE

A number of published studies have suggested a fundamental relationship, between mechanical layering and fracture intensity (Underwood et al., 2003; Cooke et al., 2006). Factors controlling the mechanical layering are recognised as lithology, texture and bedding thickness (e.g. Wennberg et al., 2006). To test this relationship, a case study was performed at a locality called Charlie.

The Charlie locality (see Figure 4.19) is positioned c. 300 m southwest of the Alpha fault and includes well exposed, nicely stacked tabular units of Serdj Fm. limestone. Minor faults ($d <$ 10 m) are located 20 – 50 meters away from the site and may have contributed to the observed fractures. Fracture data were recorded along 4 meter wide scanlines in each unit and include descriptions of the bed thickness, lithology, *in-situ* mechanical strength, fracture frequency and other characteristics (Appendix III; Tabel C). Key data are presented in Figure 4.19.

The observed fractures are comprised of both joints and veins, with predominantly NW-SE and NNE-SSW orientation (Figure 4.19d). Variations among the bedding units in terms of fracture distribution and morphology (e.g. bed bound, internal) can be recognised from Figure 4.19c. It is noted, regarding trends, that the C9 unit lacks bed bounded fractures. As observed from Figure 4.19b, the bedding units range mostly between 30 and 80 cm in thicknesses, apart from the massive, uppermost unit (C9, 160 cm). From the same graph (Figure 4.19b), a fracture frequency range of c. 3 to 9 fractures per meter can be determined. The fracture frequency pattern seems partly proportional to the bedding thickness; however, the massive unit (C9) conflicts with the trend by showing the lowest recorded fracture frequency. Similarly, the lithofacies fails to show an unambiguous relation to the fracture frequency, as expressed by the deviating frequencies in wackstone units with similar thicknesses (C4-6; Figure 4.19b). Comparisons of the *in situ* mechanical strength with the fracture frequency shows an irregular pattern, as expressed by the wackstone units: fracture frequencies seem partly proportional to the mechanical strengths (C2-C6 and C8; Figure 4.19e), yet deviations are reflected by C4 and C8.

Overall, the case study show ambiguous relations between the fracture frequency and proposed parameters. These inconsistencies may be explained due to a limited data set.

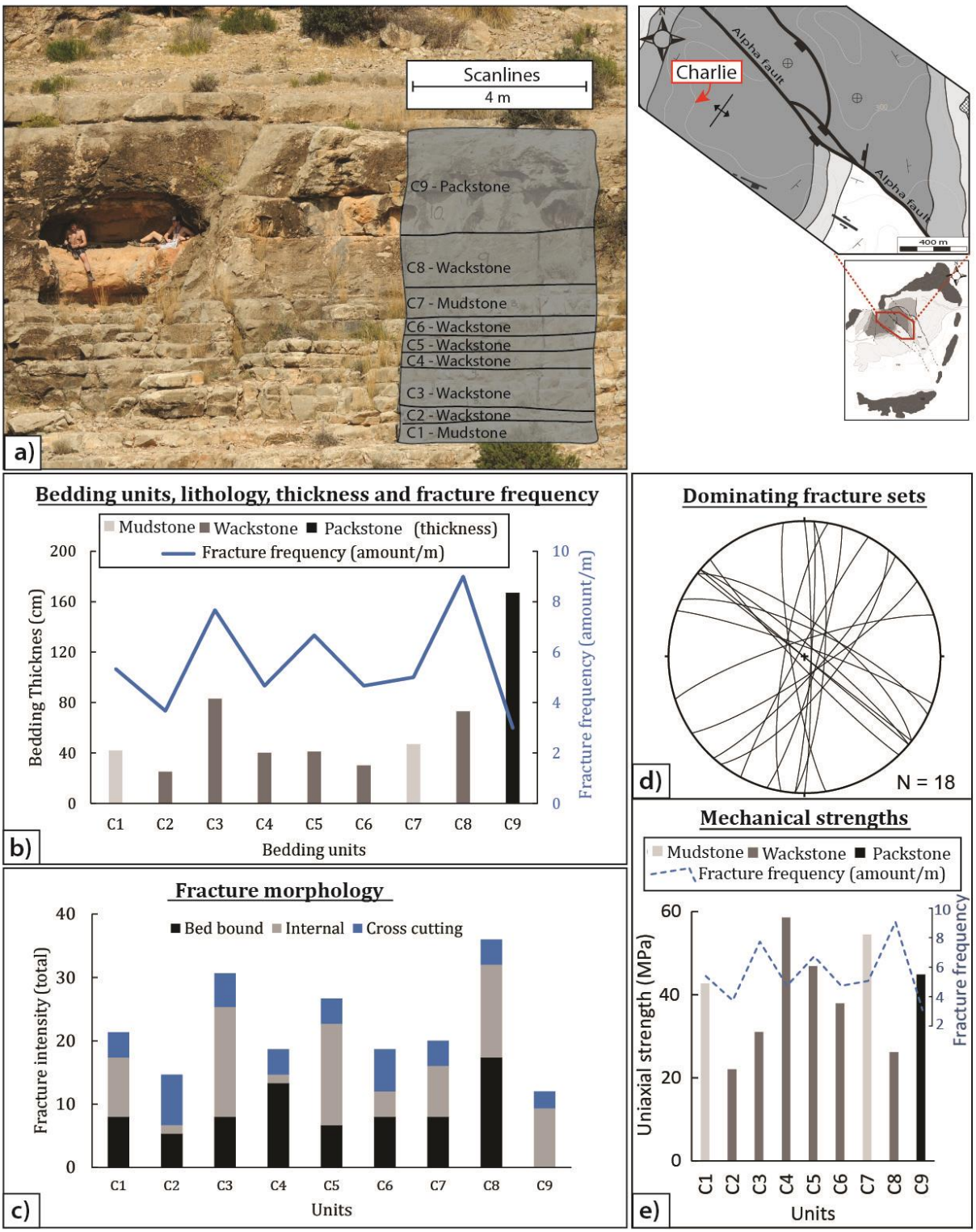

Figure 4.19 – Data from the fracture study at locality Charlie. a) Photo of the locality, with sketched scanline units and corresponding lithofacies. Notice cave men in karst cave for scale. b) Dual Y-axis plot of bedding thickness and fracture frequency. Note that (i) bedding units are categorised by lithofacies, and (ii) the fracture frequency appears partly proportional to the bedding thickness. c) Plot of fracture morphologies in each units. Notice absence of bed bound fractures in the C9 unit. (d) Stereoplot of the dominant fracture populations, trending NW-SE and NNE-SSE. e) Dual Y-axis graph, showing uniaxial strength, i.e. from schmidt hammer, and fracture frequency. Units are coloured with respect to the lithofacies. Note the inconsistent relationship between the uniaxial strength and the fracture frequency.

4.3.3 MICROSCOPIC ANALYSIS

The following section presents microstructural analysis of sampled fault rocks, and includes microstructural characterisation and porosity analyses. The aim is to characterise the tectonic impact on carbonate host rocks and petrophysical properties.

MICROSTRUCTURAL CHARACTERISATION

A total of 10 thin sections from the Alpha fault zones have been studied and analysed (see table 4.2). In order to capture different deformation signatures, samplings were carried out and categorised with respect to the fault zone architecture. Analyses of microfractures, and micrographs of all the thin sections can be found in appendix III and II, respectively.

Tabel 4.2 - Overview of thin section samples with characteristic observations

Sample	Sedimentary descriptions		Structural descriptions		
	Lithofacies	Microfossils (components in order of abundance)	Structural domain	Tectonic facies	Deformational fabrics
A1.1	Wackstone	Micritic mud, Planktonic forams, rare benthic forams	Core	Protobreccia	Brecciation, angular clasts, intense microfractures (en echelon pattern), solution-affected fractures
A1.2	N/A	Recrystallized peloids/bioclasts, rare planktonic forams	Core	Breccia/gouge	Brecciation, shear zones, angular clasts, intraclast veins, various fracture patterns, cryptocrystalline matrix (zoned), diagentic alterations, type I and II calcite twins
A1.3	Wackstone	Micritic mud, benthic and planktonic forams	Core	Protobreccia	Intense fracturing and brecciation, angular clasts, irregular seams (stylolites), type I and II calcite twins
A1.6	N/A	Recrystallized planktonic forams	Core	Breccia	Intensely deformed calcite crystals, stylolites, intraclast, type I, II and III twins
A1.4a	Packstone	Benthic fauna, recrystallized peloids/bioclasts	FWDZ	Stylobreccia	Irregular coarse veins, zones of stylolite-bound fragments
A1.7	Packstone	Recrystallized peloids/bioclasts	FWDZ	Hydraulic breccia	Laminated to fiberous calcite growth on large crystal, brecciated zone
A1.8	Packstone	Benthic fauna, recrystallized peloids/bioclasts	FWDZ	Hydraulic breccia host rock	Zones of stylobedding, large vein of euhedral and deformed crystals
A1.4b	Packstone	Benthic fauna, recrystallized peloids/bioclasts	FWHR	Host rock	Undeformed
A1.5a	Wackstone	Micritic mud, planktonic forams	HWDZ	Protobreccia	Intense fracturing
A1.5b	Wackstone	Planktonic and benthic forams	HWHR	Host rock	Undeformed

FWDZ=Footwall damage zone; FWHR=Footwall host rock; HWDZ=Hangingwall damage zone; HWHR=Hangingwall host rock

Core samples

As illustrated in Figure 4.21, samples from the fault core area display a high degree of deformation, demonstrated by brecciation, fracturing, calcite twinning, pressure solution seams and diagenetic alterations.

In general, the breccias consist of angular clasts and fragments, ranging up to 10 mm in diameter, and are bounded by either sparite (i.e. sparry calcite) or micro-/cryptocrystalline micrite. The clasts that possess recognisable primary textures, can be categorised as wack-/packstone composed by benthic and planktonic foraminifers, which corresponds to hangingwall material. Different expressions of brecciation can be observed from Figure 4.21a and Figure 4.21e. The former shows clast-supported protobreccia, with low matrix content and large angular clasts, whereas the latter represents matrix-supported breccia/gouge, consisting of fragments, few large clasts and abundant cryptocrystalline matrix.

The fractures vary, and may be characterised by three types: (i) transgranular; crosscutting objects, (ii) intergranular; breaking along objects, and (3) intragranular; confined to an object. Hybrids are also common. Different geometries and patterns are observed, e.g. straight, sigmoidal shaped, en echelon arranged, and various orientations. The core samples are commonly populated by long (>5 mm) and wide (>1 mm) transgranular fractures, accompanied by sub-perpendicular oriented intragranular fractures of relatively smaller size (see Figure 4.21d). In general, the fracture frequencies are high (Figure 4.23a), ranging from 4.5 to 12.2 per 10 mm, with a connectivity varying from moderate to high. Presence of asymmetrical fractures with undulating margins may reflect solution enlargement.

The edges of larger, angular grains are frequently fragmented (Figure 4.21h), which reflects abrasion by chipping processes. In general, chipping is driven by grain rotation and sliding, and results in both rounded grains and fragmentation (e.g. Heilbronner and Keulen, 2006; Billi, 2010).

Twin lamellae are frequently observed in the calcite crystals, and varies in characteristics. The predominant twin populations are thin (≤1 μm), straight and dense (Figure 4.20a). However, thicker ones (≤ 50 μm) occur, mostly as straight and less dense spaced (Figure 4.20b). Rare examples of curved lamellae are also observed (Figure 4.20c-d). These twins may be categorised respectively as Type I, II and III twins, *sensu* Burkhard (1993).

Most fracture voids are infilled with coarse to fine sparite cement and matrix fragments, though microcrystalline (micrite) cement occasionally occupies in the microfractures (>1mm wide). Some fractures show layered infill and may suggest multiple generations of opening and infill.

Irregular, zigzag-shaped seams with micritic infill are recognised as pressure solution seams (i.e. stylolites), of which two styles are observed: (1) grain-contact seams; and (2) elongated, irregular seams.

Brown-coloured skeleton grains with poorly preserved internal fabrics occur alongside clasts and particles that are partly or entirely recrystallised to sparry calcite. These observations reflect some of the diagenetic overprint that occur in the core samples, particularly by recrystallisation.

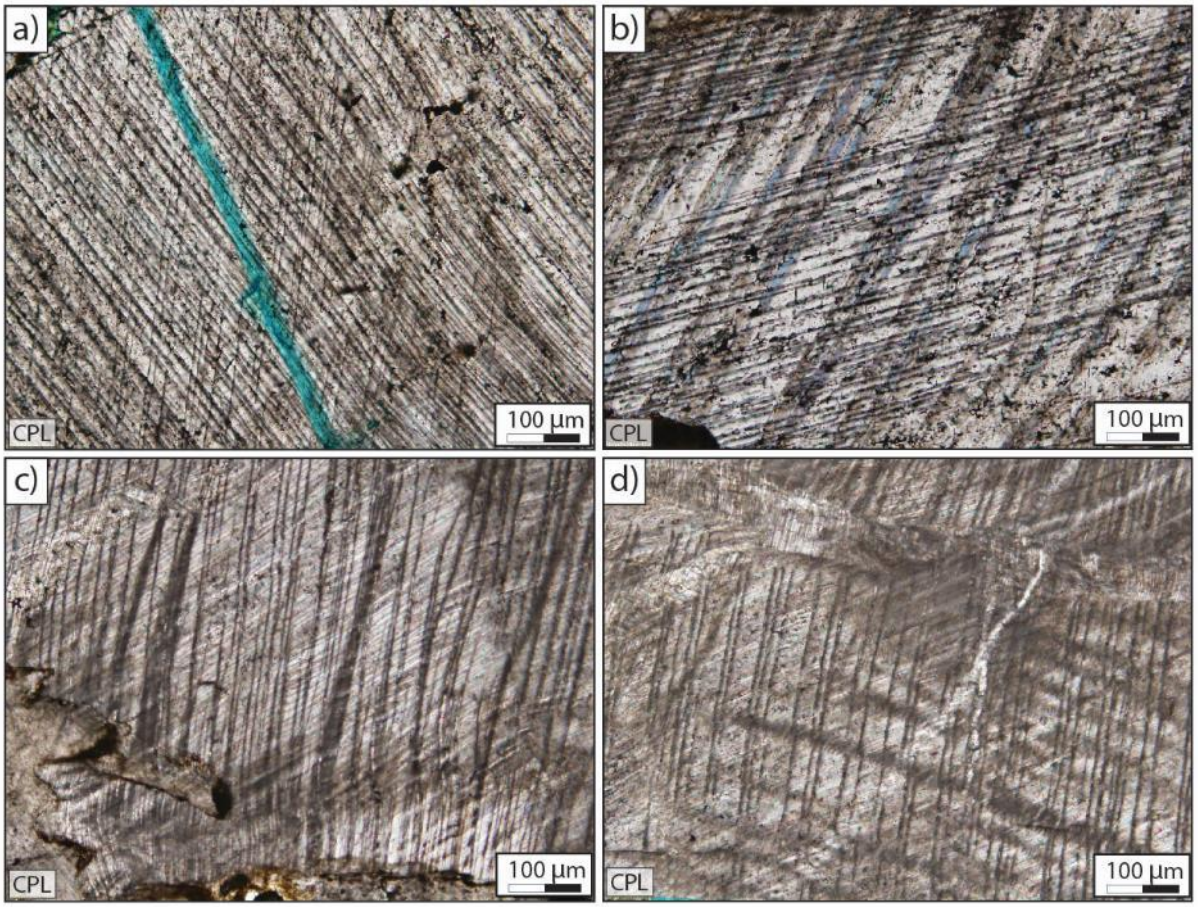

Figure 4.20 - Calcite lamellae twin types from core samples. CPL= Cross polarised. (a) Type I; thin, straight and dense twin. (b) Type II; thick (≤ 50 µm), straight and less dense. (c)-(d) Type III; thick and curved.

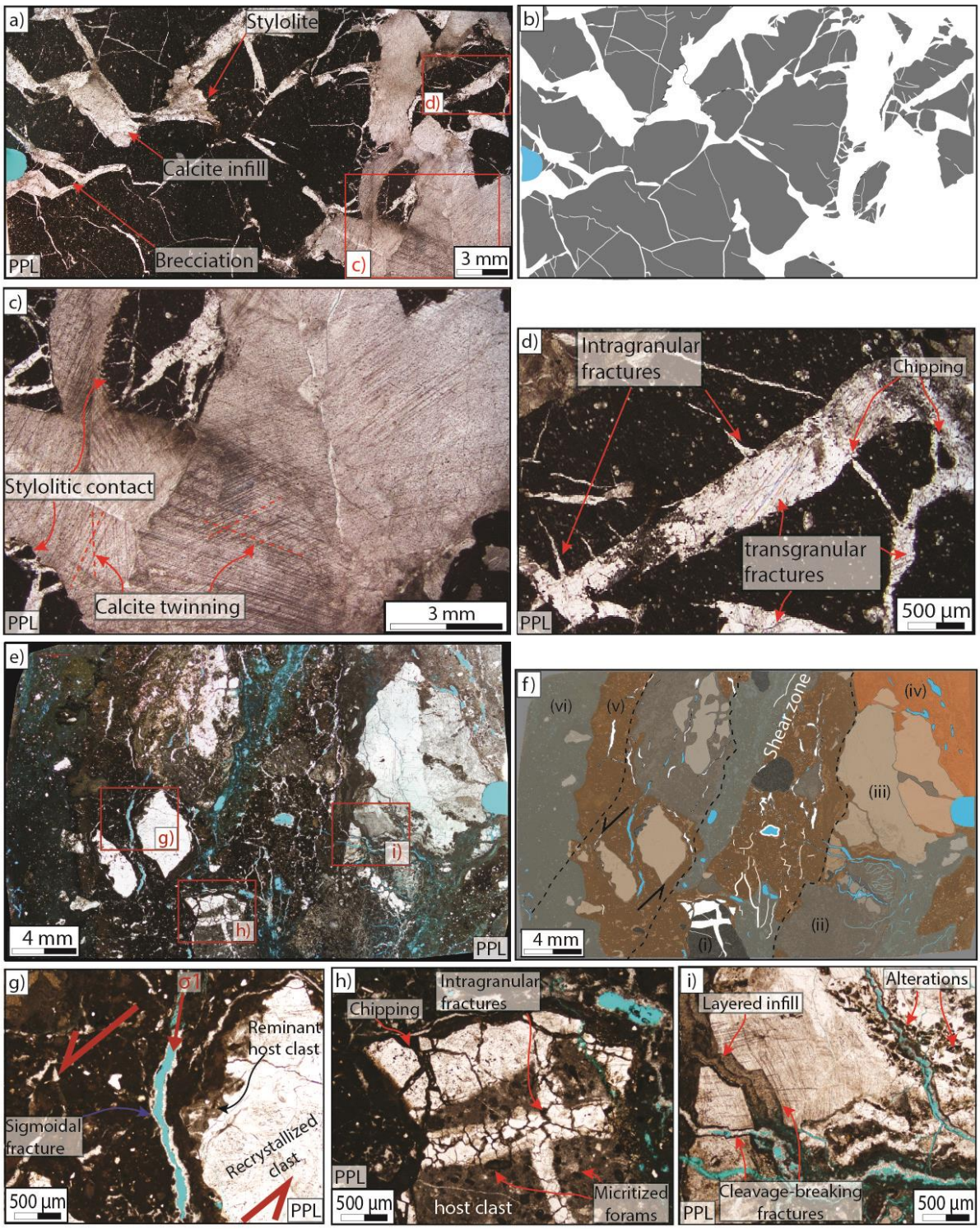

Figure 4.21 – Expressions of deformation in core samples. PPL=Plane parallel polarisation. (a) - (d) Clast-supported breccia, with stylolitic contacts, calcite twins, chipping and intense fracturing. (e) - (f) Matrix-supported breccia. Notice the different domains: (i) host clast, (ii) moderately altered clast, (iii) highly altered clast, (iv) zone of complex alterations, (v) zones of cryptocrystalline matrix and fragments, (vi) similar texture to (v), but different colour and abundant porosity. (g) Sigmoidal fracture dissecting a highly altered clast, with minor remnants of the host along the margin. (h) Host clast with intragranular fractures that clearly pre-dates the brecciation. Micritised, planktonic forams are recognisable. Chipping of edges (i') Intensely diagenetic altered and fractured clast. Note that some fractures seem controlled by the crystal cleavage, and filled with layered, fiberous calcite

Damage zone samples

The damage zones are characterised by rather preserved primary fabrics, accompanied by various degrees of fracturing and occurrence of stylolites. Fracture frequencies range from 1.0 to 7.6 fractures/10 mm, with moderate to highly connectivity. The fill and fracture types are similar to what described from the core samples.

Contrasting characteristics are observed in the Alpha fault between the footwall damage zone (FWDZ) and hangingwall damage zone (HWDZ), as illustrated in Figure 4.22a-d . The FWDZ, consisting of bioclastic packstone, comprises irregular, wide veins filled with coarse anhedral sparite, accompanied by isolated, curved microfractures, and localised zones of stylolite-bounded bioclasts. Comparatively, the calcispheric-wackstone composed HWDZ, shows hardly any stylolites, and rather appears intensely damaged by straight, transgranular fracture sets with fine-grained sparitic infill.

As described in section 4.3.2 (“Alpha fault”), an anomalous fractured corridor with a two-component infill was observed in the distal FWDZ and interpreted as hydraulic breccia (see Figure 4.11c). The thin section from the fracture infill (Figure 4.22e and f) shows marginal blocky (euhedral) to laminated calcite, and a centred, chaotic mass, consisting of fragmented bioclasts and crystals, and a cryptocrystalline matrix. A closer look at the host/marginal vein contact, shows multiple generations deformation, expressed by intergranular fracturing and kinking of twin lamellas in the crystals within the vein (Figure 4.22g-h).

Host rock samples

The sampled host rocks are relatively undeformed, with low fracture frequencies (0.5 – 1.5 per 10 mm) and poor connectivity. Pressure solution seams are observed (both grain-contact and irregular), though in a limited amount relative to core and damage zone samples. For expressions of host rocks, see appendix II.

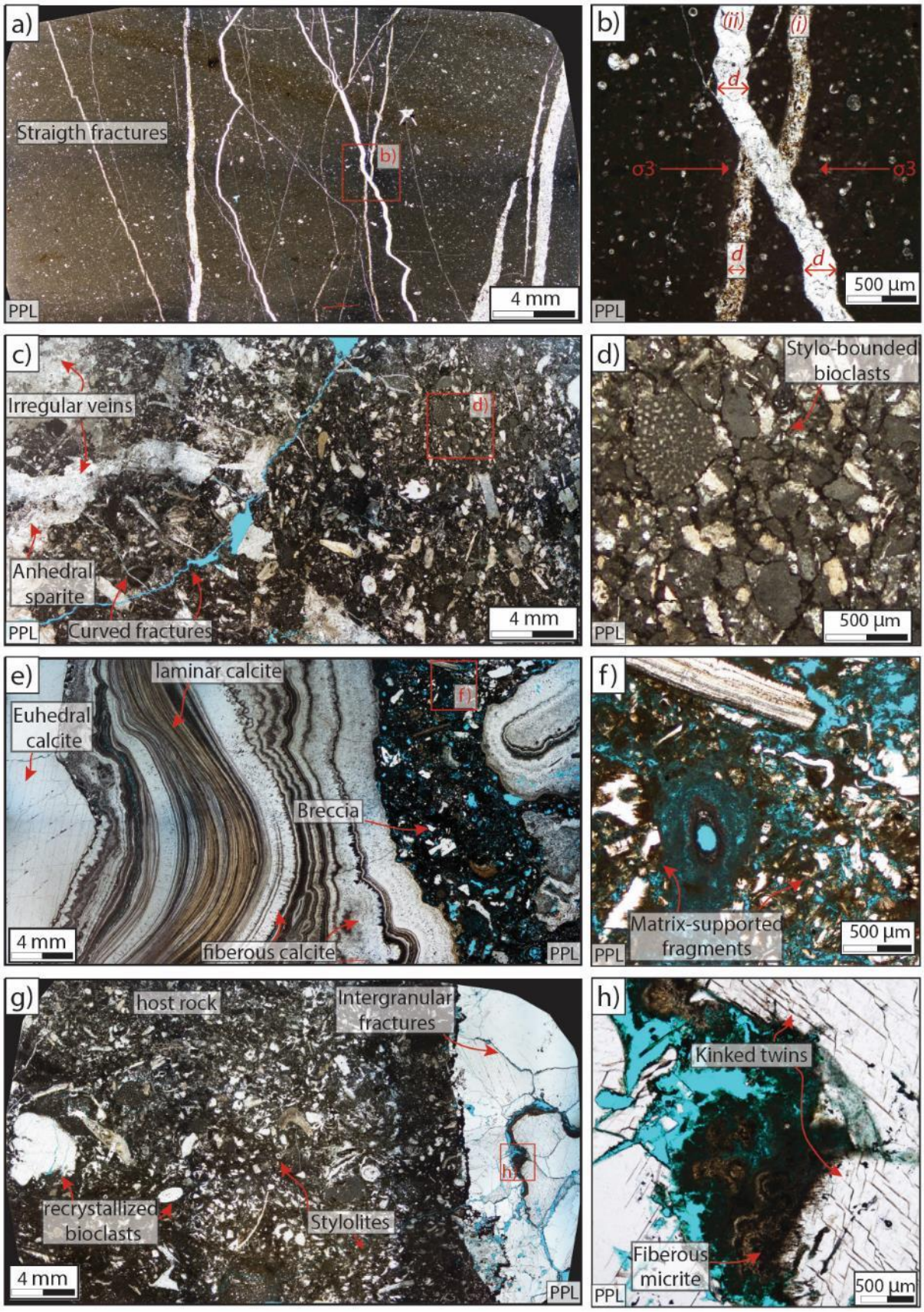

Figure 4.22 – Expressions of damage zone deformation from the Alpha fault zone: a) HWDZ sample. Note the sub-parallel oriented, transgranular fracture sets, filled with sparry calcite. The tensile mode is recognised from b), where a former generation vein (i) is crosscut by a younger, dilative vein (ii). The σ3 orientation seems

compatible for both generations. c-d) FWDZ sample. The left-hand side is dominated by coarse, irregular veins and curved, small fractures. In contrast, the right side shows lack of fractures, but possesses abundant pressure solution contacts that form zones of stylo-bounded bioclasts. e-f) FWDZ, hydraulic breccia sample, see Figure 4.11c for outcrop photo. The thin section covers the described two-component infill, represented by marginal blocky (euhedral) to laminated calcite, and a centred, heterogeneous mass. As illustrated in f), the mass consists of fragmented bioclasts and crystals, bounded by a cryptocrystalline matrix. g-f) FWDZ, hydraulic breccia host contanct. The sample covers the contact between the host rock and the marginal, blocky calcite vein. Notice the following features within the blocky calcite vein: (i) intergranular fractures, (ii) fibeours fracture infill, (iii) kinked crystal twins proximal to the fractures.

POROSITY TYPES AND ESTIMATES

The primary porosity (depositional pore space) of the Serdj Fm. host rock, hereby referred to as the matrix porosity, was analysed by Bjarte Lønøy in a sister MSc project (2015) focused on reservoir characterisation. In general, the study shows tight matrix properties, with 2D thin section porosities (φ_{2D}) ranging between 0.0 - 1.3 %. Samples from the host rocks that fringe the fault zones, display similar tight characters (φ_{2D} = 0.1 - 1.9 %).

Although the matrix porosities are negligible, a vast amount of secondary porosity types are observed in thin sections from the fault zones, including fracture porosity, vugs, and secondary inter-/intraparticle (see Figure 4.24). As described in the previous section, most fracture voids are calcite filled. Still, open or partly open fractures occur frequently, and forms the majority of measured porosity within the fault rocks. Some fractures show asymmetric margins and irregular shapes, suggesting enhanced void-space by dissolution. These are commonly termed channels, but for simplicity they are not differentiated from fracture porosity in this thesis.

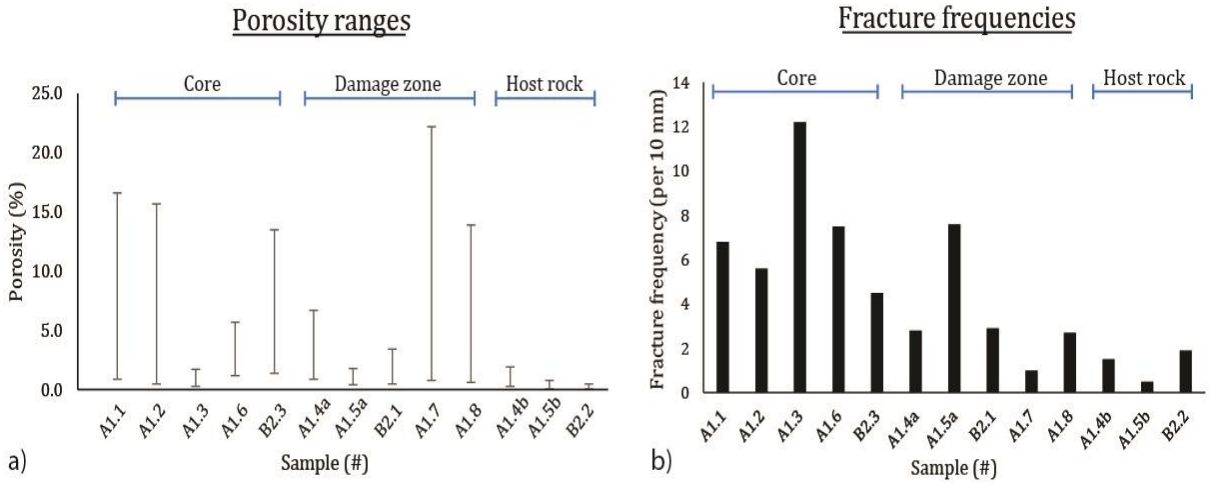

Figure 4.23 – Comparison of porosity and fracture data from thin sections. a) Overview of the porosity image analysis. Notice subdivison after fault domain. b) Plot of microfracture frequency. Note (1) the decreasing fracturing trend from the core to host rocks, and (2) a partly fit between porosity and fracture frequency.

As illustrated in Figure 4.23a, the core and damage zone samples have higher max. φ_{2D} values, than the host rock. A partial fit between fracture frequency and porosity may be

observed from Figure 4.23. Deviating values are also apparent, i.e. A1.3 and A1.7. For consideration, it should be mentioned that high-porosity samples (A1.7 and A1.8) in the damage zone, corresponds to the hydraulic fracture corridor, described in section 4.3.2 – Alpha fault. These samples are dominated by secondary inter-/ and intraparticle porosities, which seem to cause the deviation from the general pattern.

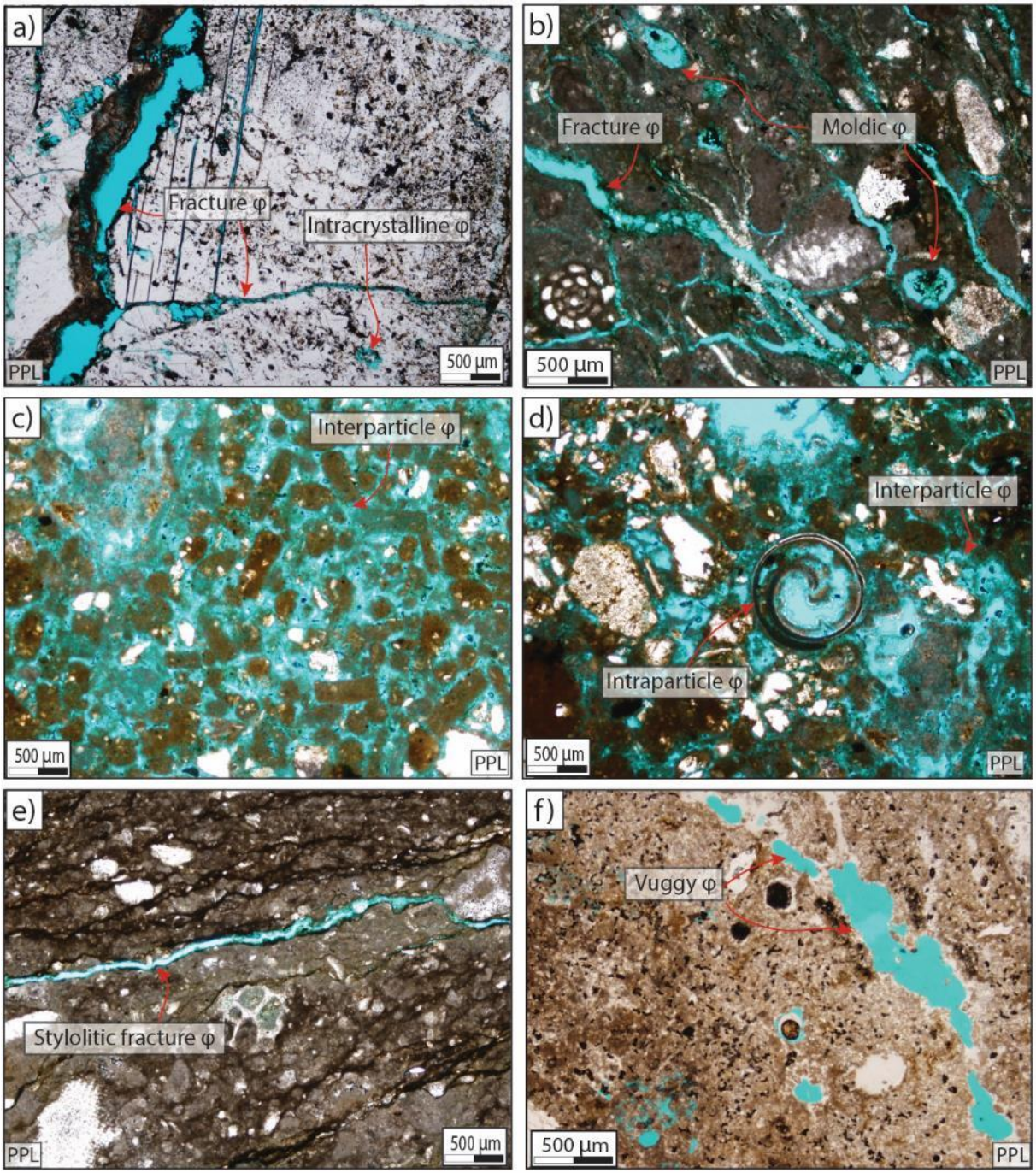

Figure 4.24 - Overview of observed porosity types in the fault rock. a) Fracture porosity: notice (1) irregular fracture margins, indicating dissolution, accompanied by pore-reducing cement, and (2) isolated, intracrystalline pores. b) Anastomosing fractures and moldic porosity. c) and d) Secondary inter-/intraparticle porosity in hydraulic breccia. e) Stylolitic-shaped fracture porosity. f) Isolated to touching-vug porosity amongst diagenetic overprinted matrix.

5. DISCUSSION

The presented data and observations from the study area reveal a variety of structures and rock properties of different scales. This study set out with the key aims of (i) structurally map and analyse the Jebel Fadeloun (JF) Anticline, and (ii) examine the tectonic impacts on the host rock. To assess these aims, following aspects will be discussed:

- Structural evolution
- Rock deformation and implications for fluid flow

5.1 STRUCTURAL EVOLUTION OF THE STUDY AREA

5.1.1 FOLDING MECHANISM

The poor seismic expression (section 1.4) of the JF Anticline results in a situation where the interpretation of its internal geometry relies partly on structural models, as well as the outcrop characteristics. As the described in section 4.3.1, observations from both field and seismic data display an open and upright fold, dissected by predominantly NW-SE oriented faults. Four alternative hypotheses are proposed for the mechanism folding the JF anticline: I) contractional ramp-related folding, II) detachment folding, III) folding related to salt mobilisation, and IV) transpressional folding.

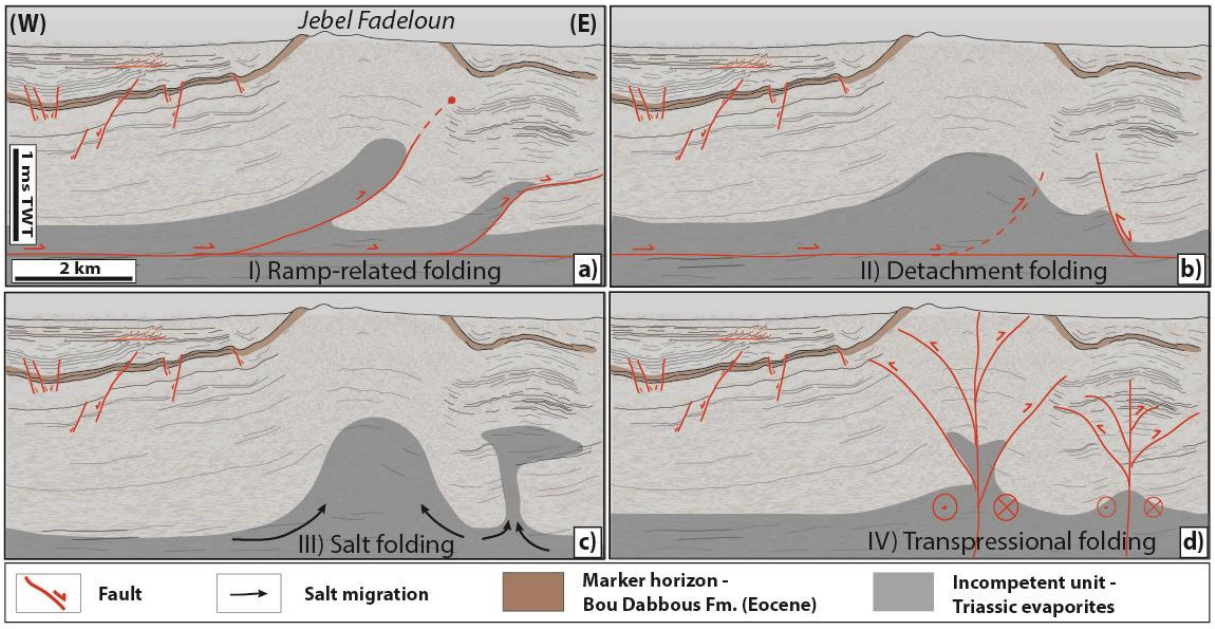

Figure 5.1 – Conceptual illustrations of the proposed folding mechanisms. a) Hypothesis I), contractional ramp-related folding. In terms of geometry, the left-hand thrust corresponds to a fault-propagational fold, next to a fault-bend fold. b) Hypothesis II), detachment folding and possible break-thrust. Also, note the potential inversion folding in the eastern anticline. c) Hypothesis III), folding by salt mobilisation. d) Hypothesis IV), transpressional folding.

Classic geometric models (e.g. Suppe, 1983; Suppe and Medwedeff, 1990) of ramp-related folds, i.e. fault-bend and fault-propagation folding, tend to describe asymmetric folds with steep forelimbs and vergence towards the thrust direction (Chapter 2; Figure 2.2f-g). However, adjustments in the contractional ramp-related folding scenario may allow for symmetric fold geometry, by invoking elements such as internal back-thrusting (e.g. Huiqi et al., 1992; McClay, 2011), imbricate relations (e.g. Mitra, 1986; Mitra, 1990), reactivation/involvement of pre-existing extensional fault (Williams et al., 1989; McClay, 1995), or possibly a combination of these (Figure 5.1a).

Although the proposed contractional ramp folding might be applicable, alternative models may provide a better fit with the symmetrical fold. For instance, detachment folding (Figure 5.1b) tend to form more symmetric geometries, both across and along fold axes (Mitra, 2003; Hardy and Finch, 2005). Further, detachment folding develops in thick sedimentary units of considerable competence contrast, which fits well with certain intervals in the local stratigraphy, e.g. the Triassic evaporites overlain by the Jurassic limestones.

The presence of potentially mobile evaporites means that also halokinetic models should be considered. As described in section 2.1, salt tectonism (Figure 5.1c) can form a variety of anticline structures, e.g. salt walls, domes and pillows (Jackson and Talbot, 1991; Hudec and Jackson, 2007). Salt movement may be induced simply by differential loading in the overburden, thermal gradients, but most commonly, by displacement during regional extension or shortening (Hudec and Jackson, 2007). Furthermore, expressions of salt structures are reported from the offshore Pelgian Platform (Mejri et al., 2006) as well as the North-South Axis (Hlaiem, 1999) and the Tunisian Atlas (Patriat et al., 2003).

A last proposed folding mechanism, is transpressional folding (Wilcox et al., 1973; Woodcock and Fischer, 1986). Transpressional folding (Figure 5.1d) may form by imbricate thrusting at restraining bends along strike-slip faults (Woodcock and Rickards, 2003). Some authors (e.g. Boccaletti et al., 1990; Bouaziz et al., 2002) have postulated sinistral transpressional activities, oriented approximately N-S, in the North-South Axis region,. Furthermore, Saadi (1990) interpreted the JF anticline, together with Jebel Garci and Jebel Mdeker (see Figure 4.1), to show signs of strike-slip architecture, including Riedel shears (*sensu* Woodcock and Schubert, 1994).

Khomsi et al. (2009) present an overview of the structural styles in the study area region. Based on interpreted seismic sections and wells, they report the following features: (i) contractional ramps and imbricate stacks (ii) salt diapirs, (iii) inverted, listric normal faults that extend down to the Triassic evaporites, and (iv) transpressional flower structures. Apparently, this suggest that all the proposed mechanisms are admissible. That said, some show less promising applicability: Firstly, the salt bodies decribed by Khomsi et al. (2009) shows sign of shortening mechanisms, associated with a regional detachment fault. Likewise, Hlaiem (1999) claims to record precursor salt bodies, in the NOSA/Pelagian Platform transition zone, that are intensely distorted by later compressional events. Seen in context with JF anticline's proximity to unambiguous thrust structures (section 4.2), simply salt-induced folding, decoupled from shortening deformations, appears somewhat unlikely. Secondly, reported transpressional flower structures (Khomsi et al., 2009) have E-W orientations and belong to an anomalous dextral strike-slip corridor, trending E-W and situated c. 40 km south of the JF anticline. Given their distance and contrasting trend, the described positive flower structures are considered irrelevant for the JF. Nevertheless, in terms of an proposed N-S oriented sinistral strike-slip regime (Boccaletti et al., 1990; Saadi, 1990), the trend of the JF anticline (NE-SW) is geometrically compatible with conceptual models of transpression (e.g. Wilcox et al., 1973; Woodcock and Fischer, 1986; Fossen et al., 1994). However, the lack of a fold-parallel (imbricate) fault pattern in the field area, conflicts with the transpressional flower model.

In terms of the folding mechanism, bearing in mind the presented arguments, contractional ramp-related folding (I) and detachment folding (II) appear the most compatible candidates. Shedding new light on the matter, Khomsi et al. (2009) report a buried structure (Kondar, Figure 4.1 and Figure 5.2), extending over more than 50 km, which overlaps with the JF anticline. The Kondar structure forms a symmetrical fold in the external domain of the trailing thrust sheet (Figure 5.2b), identical to the JF anticline. To support their argument, they refer to the failed petroleum well (Kfb, Figure 5.2), situated 30 km SW of the JF anticline. According to Khomsi et al. (2009), the well penetrated the crest of the Kondar structure to encounter a complex zone with a repeated section of Cretaceous limestones and Triassic evaporites. Correspondingly, Khomsi et al. (2009) interpret an internal structure of imbricated thrust sheets. They suggest the Kondar structure formed by contractional movement of a regional inherited listric normal fault, which also accommodated thrust splays. Parallels can be drawn

to the North-South Axis (section 3.1.1), which is presumed to have been developed by contractional reactivation of deep-seated normal faults (e.g. Hlaiem, 1999; Mejri et al., 2006).

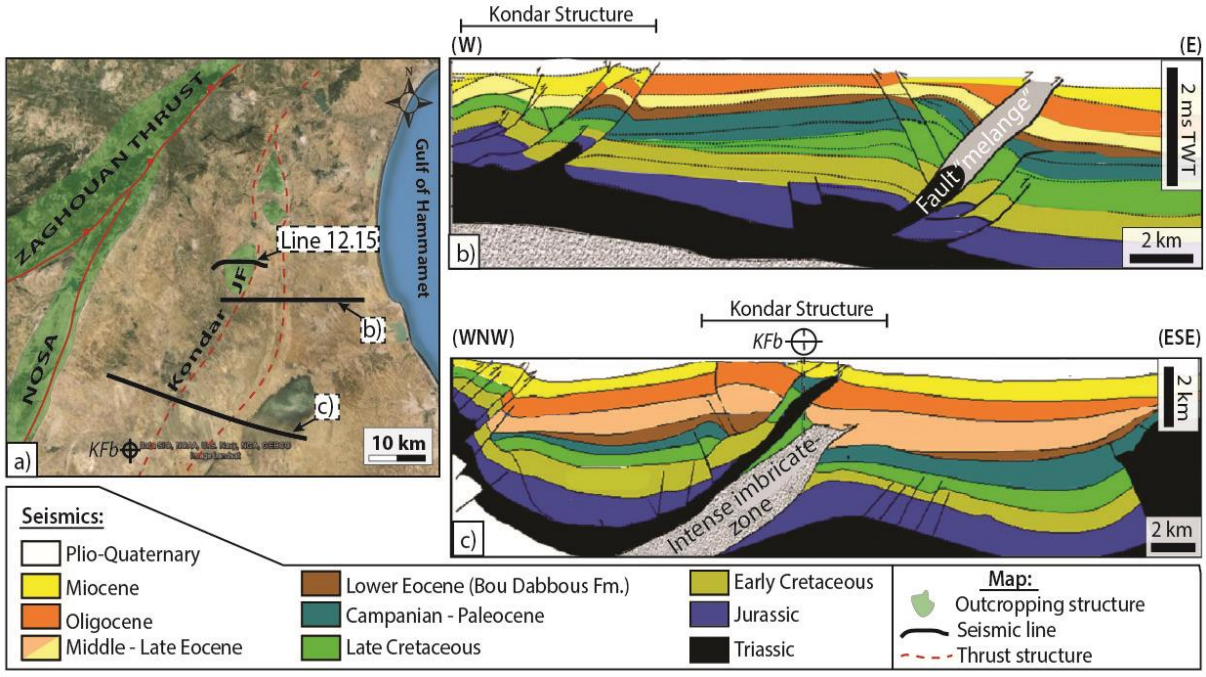

Figure 5.2 – Tectonic map and interpreted seismic sections. a) Tectonic map, including the seismic survey lines and position of the well Kfb. b) Seismic section. Notice the following features in the Kondar structure: 1) imbricate stack geometry, including minor thrust splays, and 2) symmetric fold in external domains of the trailing thrust sheet, identical to the JF anticline. c) Seismic section and well path. Notice (1) the symmetric outer fold, (2) the contractional ramp mechanisms, (3) back-thrusting in the backlimb, and (4) the KFb well, which showed a repeated section of Late Cretaceous and Triassic salt. Seismic sections are from-, and interpreted by Khomsi et al. (2009) and Khomsi et al. (2012).

It is unknown whether the interpretations (Khomsi et al., 2009) are equally based on the seismic and the well data. Suppose, for the sake of argument, that the interpretations are influenced by the well data, it would allow for other scenarios: Similar symmetric fold geometries, underlain by thrusts, can be achieved, for instance, by invoking the break-thrust model (*sensu* Fischer et al., 1992). Break-thrust folds initiates as detachment folds, which are subsequently faulted by thrusts that branch up from the detachment surface in response to progressive deformation, or contrasting stress/strain rates (Rowan, 1997; Mitra, 2002). The break-thrust folding scenario is hereinafter referred to as model II').

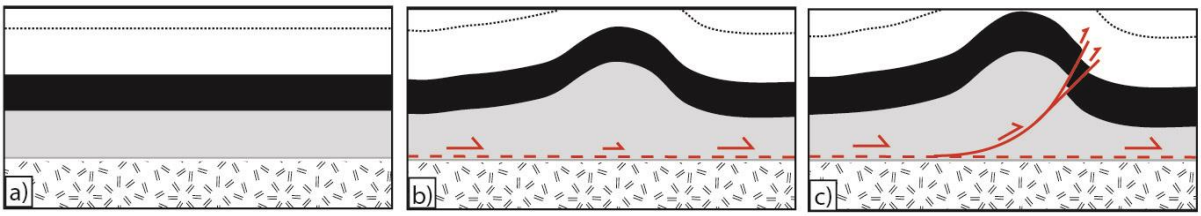

Figure 5.3 – Schematic illustration of break-thrust fold model. a) Pre-deformation. b) Detachment folding. c) Fold amplification and break-thrusts through the forelimb.

Analogue observations are reported from the Gulf of Mexico (e.g. Rowan, 1997; Salomon-Mora et al., 2009). A study by Rowan (1997) from the Mississippi Fan foldbelt, Gulf of Mexico, demonstrates how the frontal structure of the foldbelt, externally, displays symmetric fold geometries. However, the internal structure reveals a break-thrust fold, with local asymmetries. He further claims the symmetric outer arc was dictated by pre-existing salt pillows, and largely partitioned from later thrusting within the internal domain.

Parallels can be drawn from break-thrust folds in the Mississippi Fan foldbelt, to the JF/Kondar structure. Then again, assuming the JF Anticline corresponds to the Kondar structure, it aligns parallel (Figure 4.1) with the North-South Axis, the Zaghoan Thrust, and the overall atlassic trend. For this reason, it appears questionable that a pre-existing salt structure, if not controlled by a regional inherited framework, would dictate the folds and faults into an atlassic orientation. However, other studies have shown that symmetric break-thrust folds may form independently of precursor salt bodies (e.g. Costa and Vendeville, 2002; Mitra, 2002; Salomon-Mora et al., 2009). According to Mitra (2002), symmetric fold geometries are generally favoured by (i) low dipping detachments, and (ii) low frictional resistance. The break-thrust model is, thus, considered applicable, alongside the contractional ramp-related folding.

The presented arguments concerning the fold mechanism of the JF, points out the following:

- The geometric expressions from seismic lines, coupled with available well data, suggests that the JF comprises an external, symmetric fold, and a faulted internal domain. Furthermore, the proposed linkage to a buried structure, Kondar, implies an along-strike extent of more than 50 km.
- Folding by the III) salt diapirism model, or the IV) transpression model, conflicts with the observations, and appears incompatible with the reported structural styles and stress regimes in the area.

- The most compelling model is presented by the I) contractional ramp-related folding, which coincides with the dominant structural style reported by Khomsi et al. (2009). The model accounts for folding by contractional movement up a fault-ramp, and may include involvement of inherited listric normal faults. Alternatively, one may also speculate in the applicability of the II') break-thrust fold model, as it could form similar geometries, in accordance with both seismic and well data.

5.1.2 SPATIOTEMPORAL EVOLUTION OF THE FOLD, FAULTS AND FRACTURES

A critical aspect in understanding a structure and its evolution, is to constrain the relative timing of events. The deformation history can be inferred by investigating various structural relations, e.g. orientations, crosscutting relations, and overprinted fabrics. Further, tectono-stratigraphic relations may allow for more accurate dating of deformation events, for instance by unconformities and syn-tectonic growth strata. Based on presented data, it is possible to infer the deformational history of the Jebel Fadeloun anticline.

TIMING OF FOLDING

As expressed by the geological map (Figure 4.2), the outermost unit of the outcropping anticline corresponds to the Bou Dabbous Fm. of Eocene age, which suggests that the folding postdates the Eocene. Furthermore, observations seismic data (Figure 4.7) shows an angular unconformity where the overlying units appear to participate in the folding. Based on its stratigraphic position, coupled with reported unconformities the region (Khomsi et al., 2009; Hezzi et al., 2015), the unconformity is interpreted as either (i) the Oligocene/Miocene Unconformity, or (ii) the Upper Miocene Unconformity. Nevertheless, the folding of units above the unconformity suggests that the fold was formed, or accentuated during Miocene/Pliocene. By comparison, this is consistent with the interpretation by Khomsi et al. (2009), regarding the Kondar structure. They interpret the Miocene units to be conformably folded with the units below (Figure 5.2b-c). Moreover, the unfolded overlaying unit, of Pliocene-Quaternary age, pinpoints the folding to the Mio-Pliocene, i.e. coeval with the main atlassic compressional phase.

TIMING OF FAULTS AND FRACTURES

The studied faults of the JF anticline display predominantly fold-perpendicular NW-SE trends with chiefly normal-sense displacement. A key question is whether these are related to the folding or not. Three scenarios can be defined: (1) pre-fold faulting, (2) syn-fold faulting, or (3) post-folding.

The first scenario, (1) pre-fold faulting, suggests that the normal faults formed by an event prior to the folding. By comparison, regional studies (Burollet, 1991; Mejri et al., 2006) have reported the occurrence of NW-SE trending extensional faulting, dated to Oligocene age. According to Mejri et al. (2006), the faults developed by low differential stresses, related to transient relaxations in the regional, NW-SE oriented, compressional stress. However, observations from one of the major faults (Alpha Fault, section 4.3.2), suggest fault-related drag folding of hangingwall units. The preserved fault drag geometry conflicts a pre-folding origin, as it would likely have been overprinted by subsequent folding (Yamaji et al., 2005). Also, considering the matching orientation between the regional shortening direction and faults, a pre-folding faults scenario might preferably invoke (i) strike-slip reactivation and potential fold partitioning, or (ii) fault plane deformation. Neither of these features are characteristics of the study area.

The second scenario, (2) syn-fold faulting, implies $\sigma 1$ oriented NW-SE, with corresponding $\sigma 3$ directed NE-SW. Various studies have established a geometric relationship between fracture orientations and folds (e.g. Hancock, 1985; Ramsay and Huber, 1987; Price and Cosgrove, 1990). This system may provide an analogous proxy for similar large-scale structures, such as faults (Figure 5.4b). Conceptually, joints may form normal (T2) and parallel (T1) to the fold axis, to accommodate layer-parallel shortening and flexural folding (Fischer and Wilkerson, 2000). Similarly, conjugate pairs of shear fractures (R,R') tend to develop with an acute bisector perpendicular to the fold axis (Price and Cosgrove, 1990). Several features in the study area (Figure 5.4a), including fold axes, normal faults and an apparent strike-slip fault, may coincide with the proposed strain ellipse (Figure 5.4b). It is possible, therefore, that they developed simultaneously from the same stress state. Although such connections may be drawn, it is important to bear in mind that this presumes minimal rotation of the structures post-formation (e.g. Law et al., 2001). By comparison, the lack of axis-parallel faults, especially at the crest, conflicts with outer-arc extension, which assumes axis-perpendicular extension by orthogonal flexural folding (e.g. Wennberg et al., 2007). This observation may support that the envisaged syn-folding faults developed in a similar manners as the T2 fractures (Figure 5.4), parallel with $\sigma 1$. Additionally, one could speculate in a flexural component along the axis itself, considering its double plunge.

A study by Moustafa (2013) in the Syrian Arc belt, Egypt, characterised the fault patterns of various folds. According to his findings, the fault patterns were dominated by fold-axis perpendicular faults, and secondarily axis-oblique, conjugate fault sets. Moustafa claims the

syn-folding faults developed in response to the regional compressive stress as well as local strain during the folding progress. Expressions of axis-perpendicular faults are also reported from Tunisian Atlas region, and similarly interpreted as syn-folding faults (e.g. Chihi and Philip, 1998; Dhahri and Boukadi, 2010).

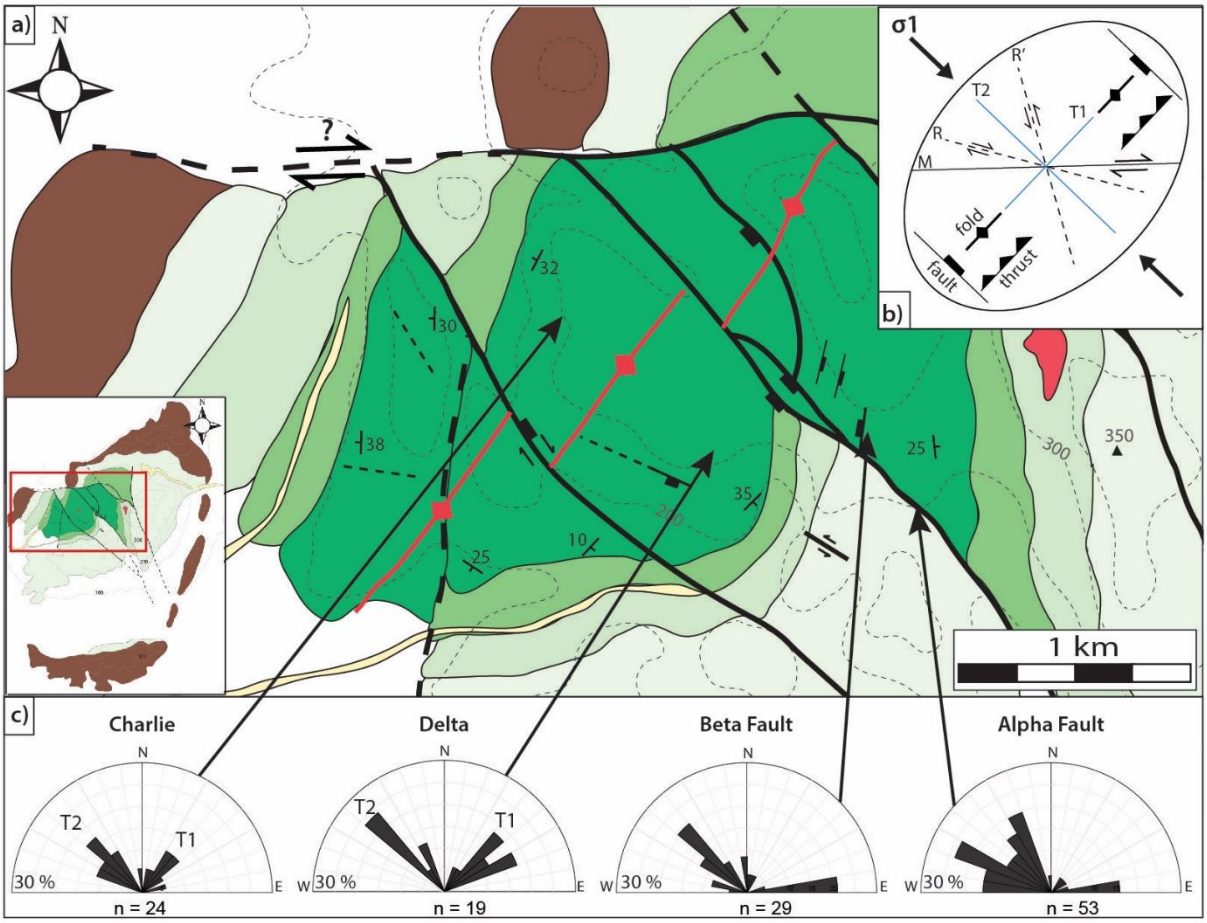

Figure 5.4 – Geological map of the study area with fracture orientations and proposed syn-fold relations. The inset map shows the location. a) Map of the study area. b) Interpreted strain ellipse, including conceptual structures related to the Riedel shear systems and flexural folding. Notice the possible correlations between the map and strain ellipse, including (i) NW-SE oriented normal faults and T2 fractures, (ii) the fold axes, (iii) E-W oriented, potential dextral strike-slip fault and the M. The dextral slip-sense is simply based on speculation. c) Summary half rose digram of recorded fracture orientations at selected localities. Note the interpreted T1-T2 fracture set in the rose diagrams, related to flexural folding. Structures in b) are adapted from Price (1966) and Hancock (1985).

The third scenario, (3) post-fold faulting, may suggest vertical σ1, and horizontal σ3 oriented NE-SW, (*sensu* Anderson, 1951). Similar stress states in this region are described by Bouaziz et al. (2002), who report NW-SE trending syn-sedimentary normal faults, of Late Miocene-Pliocene age, throughout the Pelagian Platform. They claim faults were formed by NE-SW oriented extension, related to regional extension in the Pantelleria-Malta-Linosa grabens, Mediterranean Sea (described in section 3.1.2). However, a proposed extensional stress

regime in the Mio-Pliocene conflicts with the coeval, and unambiguous, regional contraction. It is therefore proposed that the faults would have formed by transient relaxations, similar to scenario (1), rather than regional extension. Considering observations from the seismic section (Chapter 0; section 4.3.1), there are no expressions of extensional faulting in the units above the Oligocene/Miocene unconformity. This is unfortunate, since it could potentially reveal if the post-folding units were subjected to faulting, i.e. faults postdate the folding. Nevertheless, it might suggest that the outcrop faults are constrained to the anticline.

All thing considered, both scenario (2) and (3) appear plausible. It may also be that a combination of these occurred. Still, scenario (2) presents the most compelling arguments, in terms of (i) the match between fault patterns and the conceptual strain ellipse, and (ii) the similarity with alike structures in the Tunisian Atlas.

COMMENTS ON FRACTURE RELATIONS

In general, fault-related fractures form (sub) parallel to the major slip planes (e.g. Pollard and Aydin, 1988; Caine et al., 1996). Thus, it may be difficult to differentiate these from fold-related fractures, considering the parallelism of the faults and the T2 fracture sets in the study area. The scanlines from the study area, however, show a significant increase in the fracture frequency, associated with fault zones. It is reasonable to assume the fracturing patterns here are rather controlled by faulting. In turn, contrasting fracture trends (Figure 5.4c) between fault zone localities and distal localities, i.e. Charlie and Delta, might be explained by the complexities associated with fault zones, such as segment linkage, fault jogs and fault splays (Faulkner et al., 2010).

5.2 TECTONIC IMPACTS ON CARBONATE ROCKS: IMPLICATIONS FOR FLUID FLOW

Whereas the previous sections address aspects of larger-scale deformation structures, the present section aims to characterise the tectonic impacts on host rocks, in terms of microtectonic structures and processes, petrophysical properties and implications for fluid flow.

The strong link between brittle fault zones and fluid flow has been reported in a vast body of published studies (e.g. Chester and Logan, 1986; Caine et al., 1996; Billi et al., 2003). According to Caine et al. (1996), fluid flow is dictated by fault architecture: a conceptual model based on strain contrasting domains, i.e. core and damage zones. Depending on various factors, the fault architecture may represent a combined barrier-conduit system for fluid flow (Caine et al., 1996; Billi et al., 2003; Micarelli et al., 2006; Agosta, 2008). Specifically, studies in faulted carbonates show that fractures in damage zones can increase the porosity and permeability, whereas cataclasis (grain comminution) and chemical processes in the core may significantly decrease petrophysical properties (Billi et al., 2003; Micarelli et al., 2006; Agosta et al., 2012). Although the study of faulted carbonates has considerably advanced over the recent years, less emphasis has been given to the microscopic aspects. Hence, the nature of the microtectonic processes responsible for the development of low-permeable cores remains somewhat unclear (Billi, 2010).

MICROTECTONIC PROCESSES AND ASSOCIATED MICROSTRUCTURES

The analysed thin-sections of fault cores from the study area, shows various microstructures. These relate to a series of microtectonic mechanisms and processes that, to varying extents, may lead to grain size reduction and subsequent fault rock formation. Past studies (e.g. Billi et al., 2003; Agosta and Aydin, 2006; Agosta et al., 2012) emphasise two fundamental core-forming mechanisms in carbonates: 1) cataclasis, i.e. grain fragmentation and rigid-body rotation (*sensu* Sibson, 1977), and 2) pressure solution/dissolution. Together with potentially clay smearing, i.e. incorporation of clay-rich units into fault zones by shearing-mechanisms (e.g. Aydin and Eyal, 2002), these mechanisms are believed to control the sealing capacity of the fault (Knipe et al., 1997).

Different expressions of brecciation can be recognised from the studied core samples (e.g. Figure 4.21). These may reflect different evolutionary stages of core formation, as illustrated in Figure 5.5, and can also be tied to fault architecture domains. The proto-breccia is found in the proximal damage zone, typically represented by intense joint networks (Figure 5.5x). Further, the intermediate breccia relates to damage zone/core transition, where grain

fragmentation is resulted by intragranular extension fractures (Figure 5.5y) and, subordinately, chipping and shearing. The end-member, mature breccia, reflects fault core breccia/gouge. At this stage, most large grains are fragmented by preceding cataclastic processes, and results in the development of micro/cryptocrystalline matrix. This allows for remaining grains to rotate and slide more freely during slip displacement, resulting in a high degree of abrasive chipping (Figure 5.5z) and, occasionally, shear fracturing.

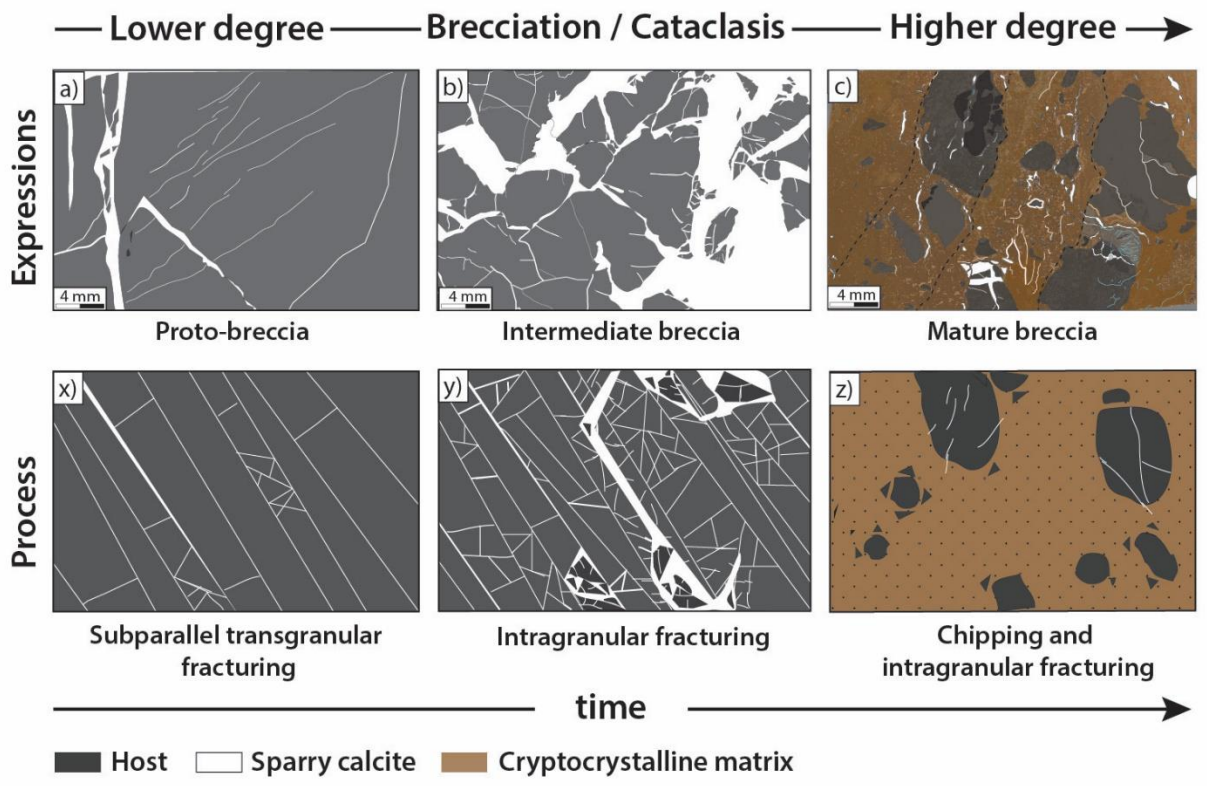

Figure 5.5 – Schematic diagram showing the proposed evolutionary model of carbonate core formation. Note that a-c) shows expressions of the fabrics, whereas x-z) illustrates corresponding principal cataclastic processes. a) Proto-breccia of predominantly subparallel, transgranular joints and minor intragranular fractures, as illustrated by the corresponding x). b) Intermediate breccia, grain comminution dominated by intragranular extension fracturing and, occasionally chipping. c) Mature breccia. At this stage most large grains are already fragmented by intragranular fracturing. This allows for remaining grains to slide and rotate, causing chipping, and possible shear fracturing. Figures x-z) are adapted from Billi (2010).

Analogue scenarios were presented by Billi (2010) in his study of carbonate fault rocks, deformed at similar pressure/temperature conditions to this study. He speculates that late-stage shear fracturing is accommodated by the abundant matrix, which allows for tectonic stress to propagate through a greater number of contact points among grains. A problem with the proposed model, however, is that it does not account for possible allocthonous clay material. Since the clay-rich Fahdene Fm. participates in the down-faulted hangingwall, as decribed in Chapter 0; section 4.3.2, chances are that clay material has been incorporated into

the fault breccia. Accordingly, one may overestimate the degree of fragmentation by assuming the matrix is entirely derived from cataclasis.

Rare expressions of pressure solution, primarily as grain contacts, appear to have a limited effect on the grain size reduction relative to the cataclastic processes. Conversely, some damage zone fabrics show a substantial amount of irregular solution seams (Figure 4.22c-d). Observations indicate that lithofacies controls the distribution of solution seams: bioclastic packstone textures (Serdj Fm.) of the footwall damage zone are clearly favoured over wackstone textures (Aleg Fm.) of the hangingwall damage zone. Railsback (1993) suggested, similarly, that well-developed stylolites are more common in pack-/gainstone textures. However, he emphasises that the development is controlled by the heterogeneities in rock fabrics, i.e. pressure-resistant grains mixed with less resistant micrite matrix. By comparison, this fits well with observed bioclastic fabrics of the Serdj Fm. The scarcity of solution seams in the core domain, couple with seam fabrics overprinted by cataclasis, suggest that most seams are inherited, pre-faulting features related to burial diagenesis or earlier tectonism. As proposed by several studies, (Alvarez et al., 1978; Peacock and Sanderson, 1995; Billi et al., 2003; Graham et al., 2003), precursory solutions seams may have a significant role in terms of fault development in carbonate rocks, as they represent preferential surfaces for subsequent shearing. One may, therefore, speculate that the solution seams may influence of fault nucleation here as well. Potential expressions of sheared stylolites (Figure 4.24e) lends support to this suggestion.

Although of less importance in terms of core-formation, observed calcite twinning represents crystal-plastic deformation by dislocations, and may, based on morphology, infer the deformation regime (Ferrill, 1991; Burkhard, 1993). The core samples show predominantly Type I twin fabrics; thin and densely spaced. According to Burkhard's classification (1993), Type I suggests deformation temperatures below 200 ºC, which correlates with the conditions in the study area, as indicated by vitrinite and fluid inclusion data (section 4.2.1). The occasional expressions of Type II and III, i.e. wider and curved, indicate temperatures between c. 150-300 ºC. These discrepancies are difficult to explain, but they may reflect local maximum deformation temperatures, resulted by faulting activity and hydrothermal fluids.

PETROPHYSICAL PROPERTIES

Studies have shown a relation between petrophysical properties, i.e. porosity and permeability, and fault architecture (e.g. Micarelli et al., 2006; Agosta et al., 2007; Agosta, 2008; Jeanne et al., 2012). Faulting of porous media is associated with porosity- and

permeability reduction by pore collapse, grain rotation, pressure solution and, locally, development of deformation bands (e.g. Aydin et al., 2006; Jeanne et al., 2012). Conversely, tight media behave more brittle. Thus, strain is preferably accommodated by fracturing rather than grain rotation, leading to increased porosity and permeability (Agosta et al., 2012).

A portable air permeameter was applied to estimate the permeability of rock matrix and fractures on outcrops. Due to technical issues, unfortunately, this approach failed to provide sufficient data points. Still, porosity data from thin-section analyses, combined with connectivity estimates from topological scanlines, may indicate the permeability structure. In general, the porosity analysis (Figure 4.23) shows, a considerable increase in porosity for both fault core and damage zone samples, relative to host rocks. The faulted rocks show porosities ranging up to 20 times higher than the host rock. Although these number are not representative for bulk porosity, they provide significant information in terms of the tectonic impact on host rocks in the study area. Additionally, data from the fracture-, and connectivity profiles in the Alpha Fault (Figure 4.15, Figure 4.16a), may suggest a fracture-induced, high permeable zone, 3-4 meters wide, in the proximal footwall damage zone.

IMPLICATIONS FOR FLUID FLOW

The presented evolutionary model for cataclasis and core development has implications for the permeability structure. It is reasonable to infer that early grain comminution, by intragranular fracturing, could develop fracture connectivity and, therefore, increase porosity and permeability properties in tight carbonate rocks. As the cataclasis evolves, a fine-grained matrix develops from the fragmentation, which seals pores and passages. This implies that fault breccia, depending on the degree of cataclasis, could, at least transiently, represent permeable zones, juxtaposed to sealing fault gouge (e.g. Sibson, 1986, 2000; Woodcock et al., 2007).

Certain studies (Billi et al., 2003; Billi, 2010) reports a significant contrast in the distribution of dissolution structures and solution seams between fault core and damage zones. Billi et al. (2003) suggest this demonstrates, effectively, the conduit-barrier structure of fault zones: fault cores lack dissolution structure due to their low permeable nature, which impedes fluid circulation and mass transfer. By way of contrast, some of the analysed core samples show clear signs of dissolution/precipitation, e.g. fiberous cement (Figure 4.21*i*) within fractures that either coeval with or postdating the cataclasis. Sibson (2000) reported potential fluid pathways within fault cores, formed by the development of internal dilation fractures/jogs and high pore fluid pressures during faulting. One may speculate that similar processes have

opened transient fluid pathway in the Alpha fault core, supported by the microscopic dissolution structures, and the intra-core blocky calcite veins at outcrop-scale. As emphasised by Agosta (2008), these pathways are eventually sealed by diagenetic fluids. However, as the rocks are uplifted and exposed to the surface, fluids may dissolve and, partially, reopen the dilational fractures. The porosity analyses may support this model, as the high porosity data, in general, relate to solution-enhanced fractures (Figure 4.23).

All things considered, the presented data and interpretations infer an evolving permeability structure (Figure 5.6a-b), controlled by the fault architecture and associated deformation mechanisms and processes. The proposed scenario for the Alpha Fault includes:

1) Initial faulting and fracturing, as illustrated in Figure 5.6a, resulting in overall increased flow properties in the fault zone
2) Displacement accumulation, causing increased fracturing and onset of cataclasis. Development of fault gouge fabrics may, locally, limit fault transverse fluid flow. The Beta Fault represents an analogue for this stage.
3) Progressive displacement, development of well-defined fault core, which results in a conduit-barrier system for fluid flow. Damage zones and, transiently, fault breccia accommodate along-fault conduits, whereas fault gouge inhibits across-fault flow.
4) Development of dilational fractures and fault jogs during displacement, leading to temporary fluid flow pathways within the fault core. Subsequently, fluid precipitations seal open voids and coat slip surfaces, similar to present outcrop-state.

These steps summarise the envisaged evolution of the fault architecture and associated permeability structure, as illustrated in the block diagram below (Figure 5.6). The presented model represents, however, a simplified version based on homogenous carbonate rocks, which does not take into account certain elements: (i) lithology and competence variations may invoke additional mechanisms, such as clay-smearing, which affects both fault architecture and permeability structure (e.g. Aydin and Eyal, 2002), and (ii) faulting of folded units results in lateral differences in terms of juxtaposed formations across a fault (see Figure 4.9). Nevertheless, a simplified model may better elucidated the effects of faulting on both the petrophysical properties of studied carbonate rocks, and the associated fluid flow pattern.

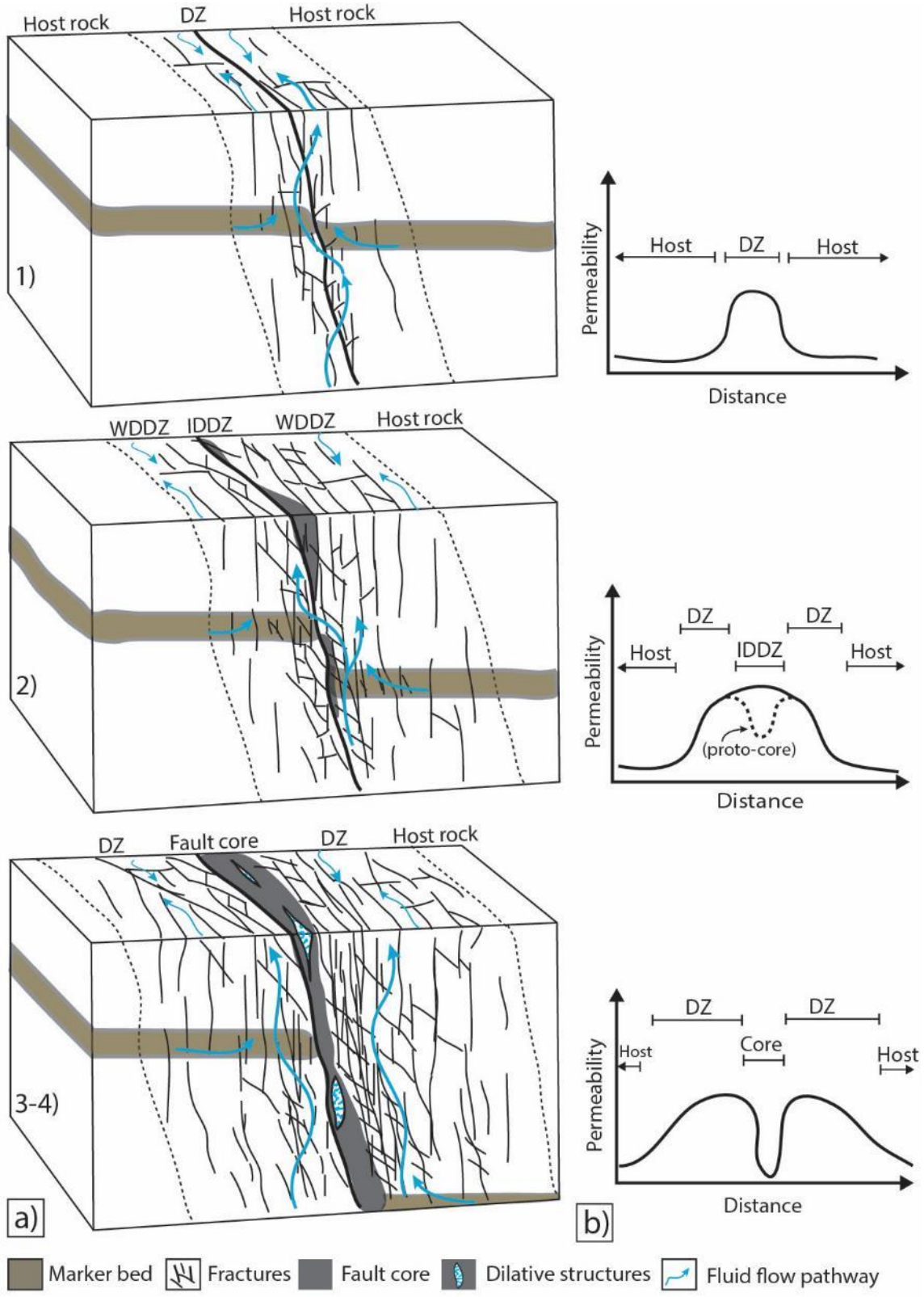

Figure 5.6 – Simplified, conceptual model of the fault architecture evolution. a) Block diagram illustrating the temporal evolution of the fault architecture and associated fluid flow. Notice the (i) lack of core, and likewise, fluid barriers at stage 1) and partly stage 2), (ii) damage zone widths expand with displacement, (iii) developed core and across-fault fluid flow barrier at stage 3-4), and (iv) potential, temporary fluid flow pathways, formed by dilational fractures within the core during slip displacement. b) Envisaged fault zone permeability profiles. DZ, Damage zone; IDDZ, Intensely deformed damage zone; WDDZ, Weakly deformed damage zone. Nomenclature from Caine et al. (1996) and Micarelli et al. (2006).

6. CONCLUSIONS AND FURTHER WORKS

Integrating macro- and microstructural analyses, this study has attempted to describe and characterise the structural evolution of the Jebel Fadeloun (JF) anticline and to investigate how tectonic deformation affected the host rocks. Based on collected data, combined with field-, and seismic observations, the following conclusions are drawn:

- The JF anticline is characterised by a symmetric and open fold geometry, with a NE-SW trend and four-way dip closure. Seismic data shows that the JF anticline corresponds to a buried structure, formed- and aligned parallel with the Tunisian Atlas structures in Late Miocene-Pliocene. Its proposed origin is contractional ramp-related folding, which accounts for folding by contractional movement up a ramp structure, and could potentially involve inherited listric normal faults. Alternatively, one may speculate in a break-thrust fold, by thrusting of a preceding detachment fold.
- Studied faults show primarily normal sense of displacement. It is suggested that these developed contemporaneous with the folding; however, there are compelling arguments for post-folding faults as well.
- The fault analyses reveal that fracture frequency and fault rocks are heterogeneously distributed in the fault zones. Denser fracture networks in the proximal damage zones are concluded to represent conduits for fluid flow, whereas fault gouge developed in the core represent barriers.
- Microstructural analyses show a clear increase in the degree of brecciation towards the fault core. It is suggested that the brecciation evolves by three processes: (I) transgranular fracturing, (II) intragranular tension fracturing, and (III) chipping. Amongst these three, the intragranular fracturing is considered the most significant process, in terms of grain comminution. Alternatively, it is speculated that some of the cryptocrystalline matrix is incorporated from the faulted, clay-rich Fahdene Fm., rather than form evolved fragmentation.
- The image analyses of deformed rocks, i.e. damage zone and fault breccia, show generally an increase in porosity, ranging up to 20 times higher than the host rock. The porosity is chiefly formed by fracturing, and occasionally enhanced by dissolution. Conversely, the fault gouge in centre of the core, is inferred to possess low porosity and permeability properties, due to high matrix content. It is thus concluded that the faulting has greatly impacted the carbonate fluid flow properties.

Significance and wider Implications of the study

This findings of this structural analysis has several practical applications for the oil and gas industry. Firstly, the study offers a specific analogue for hydrocarbon traps in fold and thrust belt settings. In particular, the structural analysis contributes to improved knowledge by characterizing trap (fold) geometry and mechanism, as well as internal deformations (faults, fractures). These results may have major applications for future exploration wells in the region. Secondly, this study demonstrates how tectonic deformation results in potential reservoir properties of the Aptian Serdj Fm. In addition, trends from the fracture characterisation, e.g. orientation and distribution, should be taken into account for in future well projects, as it may optimise well paths and enhance the sweep efficiency of reservoirs.

Limitations and suggestions for further work

The present study contributes to the existing knowledge of the Jebel Fadeloun anticline by providing an extensive structural analysis. However, the limited amount of subsurface data represents a weakness in this study. Specifically, more seismic lines, of higher quality, would improve characterisations of the fold and would likely help shed more light on folding mechanism. Also, the fracture characterisation could benefit from additional data points, with respect to both fault zones and fold curvature, and may improve knowledge of the spatiotemporal relationships.

As the study was focused on the core of the fold, further research might explore the external parts. For instance, it would be very interesting to investigate the potential relationship between the Eocene formations, and overlaying Miocene that according to the seismic data participates in folding. This may help constrain the timing of folding. Likewise, by mapping external formations, one may improve the knowledge of the fold shape, and thus provide valuable information in terms of folding mechanism. An issue that was not addressed in this study was the apparent thickness contrast between the western and eastern fold limbs, notably in the Abiod Fm. of Campanian-Maastrichtian age. Studies (Khomsi et al., 2009; Bey et al., 2012) have reported coeval synsedimentary normal faults, as well as slumping structures believed to be induced by tectonism. Thus, it could be fruitful to investigate the thickness variances and unconformities, as there may be an important tectono-sedimentary link.

There is an apparent lack of published outcrop studies concerning fold-related faulting in carbonates. As folds are typical hydrocarbon trap forming structures (e.g. McClay, 2004), and faults have a fundamental control on the fluid flow properties, more studies should be focusing on this relationship.

Agosta, F., 2008, Fluid flow properties of basin-bounding normal faults in platform carbonates, Fucino Basin, central Italy: Geological Society, London, Special Publications, v. 299, no. 1, p. 277-291.

Agosta, F., Alessandroni, M., Antonellini, M., Tondi, E., and Giorgioni, M., 2010, From fractures to flow: a field-based quantitative analysis of an outcropping carbonate reservoir: Tectonophysics, v. 490, no. 3, p. 197-213.

Agosta, F., and Aydin, A., 2006, Architecture and deformation mechanism of a basin-bounding normal fault in Mesozoic platform carbonates, central Italy: Journal of Structural Geology, v. 28, no. 8, p. 1445-1467.

Agosta, F., Prasad, M., and Aydin, A., 2007, Physical properties of carbonate fault rocks, fucino basin (Central Italy): implications for fault seal in platform carbonates: Geofluids, v. 7, no. 1, p. 19-32.

Agosta, F., Ruano, P., Rustichelli, A., Tondi, E., Galindo-Zaldívar, J., and Sanz de Galdeano, C., 2012, Inner structure and deformation mechanisms of normal faults in conglomerates and carbonate grainstones (Granada Basin, Betic Cordillera, Spain): Inferences on fault permeability: Journal of Structural Geology, v. 45, p. 4-20.

Akbar, M., Vissapragada, B., Alghamdi, A. H., Allen, D., Herron, M., Carnegie, A., Dutta, D., Olesen, J.-R., Chourasiya, R., and Logan, D., 2000, A snapshot of carbonate reservoir evaluation: Oilfield Review, v. 12, no. 4, p. 20-21.

Alaei, B., and Pajchel, J., 2006, Single arrival Kirchhoff prestack depth migration of complex faulted folds from the Zagros mountains, Iran: CSEG Recorder, v. 31, no. 1, p. 41-48.

Alvarez, W., Engelder, T., and Geiser, P. A., 1978, Classification of solution cleavage in pelagic limestones: Geology, v. 6, no. 5, p. 263-266.

Anderson, E. M., 1951, The dynamics of faulting and dyke formation with applications to Britain, Edinburgh: Oliver and Boyd.

Anderson, J. E., 1996, The Neogene structural evolution of the western margin of the Pelagian Platform, central Tunisia: Journal of structural geology, v. 18, no. 6, p. 819-833.

Antonellini, M., Petracchini, L., Billi, A., and Scrocca, D., 2014, First reported occurrence of deformation bands in a platform limestone, the Jurassic Calcare Massiccio Fm., northern Apennines, Italy: Tectonophysics, v. 628, p. 85-104.

Argnani, A., 1990, The Strait of Sicily rift zone: foreland deformation related to the evolution of a back-arc basin: Journal of Geodynamics, v. 12, no. 2, p. 311-331.

Aydin, A., 2015, ISRM suggested method for determination of the Schmidt hammer rebound hardness: revised version, The ISRM Suggested Methods for Rock Characterization, Testing and Monitoring: 2007-2014, Springer, p. 25-33.

Aydin, A., and Basu, A., 2005, The Schmidt hammer in rock material characterization: Engineering Geology, v. 81, no. 1, p. 1-14.

Aydin, A., Borja, R. I., and Eichhubl, P., 2006, Geological and mathematical framework for failure modes in granular rock: Journal of Structural Geology, v. 28, no. 1, p. 83-98.

Aydin, A., and Eyal, Y., 2002, Anatomy of a normal fault with shale smear: Implications for fault seal: AAPG bulletin, v. 86, no. 8.

Ben Ayed, N., 1980, Le rôle des décrochements EW dans l'évolution structurale de l'Atlas tunisien: CR somm. Soc. geol. France, v. 1, p. 29-32.

Bense, V. F., Gleeson, T., Loveless, S. E., Bour, O., and Scibek, J., 2013, Fault zone hydrogeology: Earth-Science Reviews, v. 127, p. 171-192.

Bey, S., Kuss, J., Premoli Silva, I., Hedi Negra, M., and Gardin, S., 2012, Fault-controlled stratigraphy of the Late Cretaceous Abiod Formation at Ain Medheker (Northeast Tunisia): Cretaceous Research, v. 34, p. 10-25.

Billi, A., 2010, Microtectonics of low-P low-T carbonate fault rocks: Journal of Structural Geology, v. 32, no. 9, p. 1392-1402.

Billi, A., Salvini, F., and Storti, F., 2003, The damage zone-fault core transition in carbonate rocks: implications for fault growth, structure and permeability: Journal of Structural Geology, v. 25, no. 11, p. 1779-1794.

Bishop, W. F., 1975, Geology of Tunisia and adjacent parts of Algeria and Libya: AAPG bulletin, v. 59, no. 3, p. 413-450.

Bishop, W. F., 1988, Petroleum geology of east-central Tunisia: AAPG Bulletin, v. 72, no. 9, p. 1033-1058.

Boccaletti, M., Cello, G., and Tortorici, L., 1990, First order kinematic elements in Tunisia and the Pelagian block: Tectonophysics, v. 176, no. 1, p. 215-228.

Bonini, M., Sani, F., and Antonielli, B., 2012, Basin inversion and contractional reactivation of inherited normal faults: A review based on previous and new experimental models: Tectonophysics, v. 522, p. 55-88.

Bonson, C. G., Childs, C., Walsh, J. J., Schöpfer, M. P., and Carboni, V., 2007, Geometric and kinematic controls on the internal structure of a large normal fault in massive limestones: the Maghlaq Fault, Malta: Journal of Structural Geology, v. 29, no. 2, p. 336-354.

Bouaziz, S., Barrier, E., Soussi, M., Turki, M. M., and Zouari, H., 2002, Tectonic evolution of the northern African margin in Tunisia from paleostress data and sedimentary record: Tectonophysics, v. 357, no. 1, p. 227-253.

Boyer, S. E., and Elliott, D., 1982, Thrust systems: AAPG Bulletin, v. 66, no. 9, p. 1196-1230.

Bratton, T., Canh, D. V., Van Que, N., Duc, N. V., Gillespie, P., Hunt, D., Li, B., Marcinew, R., Ray, S., and Montaron, B., 2006, The nature of naturally fractured reservoirs: Oilfield Review, v. 18, no. 2, p. 4-23.

Burkhard, M., 1993, Calcite twins, their geometry, appearance and significance as stress-strain markers and indicators of tectonic regime: a review: Journal of Structural Geology, v. 15, no. 3, p. 351-368.

Burollet, P., 1991, Structures and tectonics of Tunisia: Tectonophysics, v. 195, no. 2, p. 359-369.

Burollet, P., Mugniot, J., and Sweeney, P., 1978, The geology of the Pelagian Block: The margins and basins off southern Tunisia and Tripolitania, The ocean basins and margins, Springer, p. 331-359.

Caine, J. S., Evans, J. P., and Forster, C. B., 1996, Fault zone architecture and permeability structure: Geology, v. 24, no. 11, p. 1025-1028.

Cavailhes, T., 2015, Fkirine license exploration, Tunisia: summary for structural geology field work.

Chester, F., and Logan, J., 1986, Implications for mechanical properties of brittle faults from observations of the Punchbowl fault zone, California: Pure and Applied Geophysics, v. 124, no. 1-2, p. 79-106.

Chihi, L., and Philip, H., 1998, Les fossés de l'extrémité orientale du Maghreb (Tunisie et Algérie orientale): tectonique mio-plio-quaternaire et implication dans l'évolution géodynamique récente de la Méditerranée occidentale: Notes Serv Géol Tunis, v. 64, p. 103-116.

Childs, C., Manzocchi, T., Walsh, J. J., Bonson, C. G., Nicol, A., and Schöpfer, M. P., 2009, A geometric model of fault zone and fault rock thickness variations: Journal of Structural Geology, v. 31, no. 2, p. 117-127.

Cooke, M. L., Simo, J., Underwood, C. A., and Rijken, P., 2006, Mechanical stratigraphic controls on fracture patterns within carbonates and implications for groundwater flow: Sedimentary Geology, v. 184, no. 3, p. 225-239.

Costa, E., and Vendeville, B., 2002, Experimental insights on the geometry and kinematics of fold-and-thrust belts above weak, viscous evaporitic décollement: Journal of Structural Geology, v. 24, no. 11, p. 1729-1739.

Coward, M., Gillcrist, R., and Trudgill, B., 1991, Extensional structures and their tectonic inversion in the Western Alps: Geological Society, London, Special Publications, v. 56, no. 1, p. 93-112.

Dahlstrom, C. D., 1970, Structural geology in the eastern margin of the Canadian Rocky Mountains: Bulletin of Canadian Petroleum Geology, v. 18, no. 3, p. 332-406.

De Paola, N., Collettini, C., Faulkner, D. R., and Trippetta, F., 2008, Fault zone architecture and deformation processes within evaporitic rocks in the upper crust: Tectonics, v. 27, no. 4.

Dhahri, F., and Boukadi, N., 2010, The evolution of pre-existing structures during the tectonic inversion process of the Atlas chain of Tunisia: Journal of African Earth Sciences, v. 56, no. 4-5, p. 139-149.

Dhia, H. B., 1987, The geothermal gradient map of central Tunisia: comparison with structural, gravimetric and petroleum data: Tectonophysics, v. 142, no. 1, p. 99-109.

Dunham, R. J., 1962, Classification of carbonate rocks according to depositional textures, Classification of Carbonate rocks, Volume 1, AAPG Mem., p. 108-121.

Embry III, A. F., and Klovan, J. E., 1971, A Late Devonian reef tract on northeastern Banks Island, NWT: Bulletin of Canadian Petroleum Geology, v. 19, no. 4, p. 730-781.

ETAP. 2001. Tunisian stratigraphic chart [Online]. Available: http://www.sigetap.tn/globalmap/com/others/stratigraphic.pdf [Accessed 2 May 2015].

Faulkner, D., Jackson, C., Lunn, R., Schlische, R., Shipton, Z., Wibberley, C., and Withjack, M., 2010, A review of recent developments concerning the structure, mechanics and fluid flow properties of fault zones: Journal of Structural Geology, v. 32, no. 11, p. 1557-1575.

Ferrill, D. A., 1991, Calcite twin widths and intensities as metamorphic indicators in natural low-temperature deformation of limestone: Journal of Structural Geology, v. 13, no. 6, p. 667-675.

Ferrill, D. A., and Morris, A. P., 2008, Fault zone deformation controlled by carbonate mechanical stratigraphy, Balcones fault system, Texas: AAPG Bulletin, v. 92, no. 3, p. 359-380.

Fischer, M., Woodward, N., and Mitchell, M., 1992, The kinematics of break-thrust folds: Journal of Structural Geology, v. 14, no. 4, p. 451-460.

Fischer, M. P., and Wilkerson, M. S., 2000, Predicting the orientation of joints from fold shape: Results of pseudo–three-dimensional modeling and curvature analysis: Geology, v. 28, no. 1, p. 15-18.

Fossen, H., Tikoff, B., and Teyssier, C., 1994, Strain modeling of transpressional and transtensional deformation: Norsk Geologisk Tidsskrift, v. 74, no. 3, p. 134-145.

Færseth, R. B., 2006, Shale smear along large faults: continuity of smear and the fault seal capacity: Journal of the Geological Society, v. 163, no. 5, p. 741-751.

Ghiasi-Freez, J., Soleimanpour, I., Kadkhodaie-Ilkhchi, A., Ziaii, M., Sedighi, M., and Hatampour, A., 2012, Semi-automated porosity identification from thin section images using image analysis and intelligent discriminant classifiers: Computers & Geosciences, v. 45, p. 36-45.

Graham, B., Antonellini, M., and Aydin, A., 2003, Formation and growth of normal faults in carbonates within a compressive environment: Geology, v. 31, no. 1, p. 11-14.

Groshong, R., 2006, 3-D Structural geology: a practical guide to quantitative surface and surface map interpretation, Springer-Verlag Berlin, Heidelberg.

Grove, C., and Jerram, D. A., 2011, jPOR: An ImageJ macro to quantify total optical porosity from blue-stained thin sections: Computers & Geosciences, v. 37, no. 11, p. 1850-1859.

Hancock, P., 1985, Brittle microtectonics: principles and practice: Journal of structural geology, v. 7, no. 3, p. 437-457.

Hanks, C., Wallace, W., Brinton, P. A. J., Bui, T., Jensen, J., and Lorenz, J., 2004, Character, relative age and implications of fractures and other mesoscopic structures associated with detachment folds: an example from the Lisburne Group of the northeastern Brooks Range, Alaska: Bulletin of canadian petroleum geology, v. 52, no. 2, p. 121-138.

Hardy, S., and Finch, E., 2005, Discrete-element modelling of detachment folding: Basin Research, v. 17, no. 4, p. 507-520.

Heilbronner, R., and Keulen, N., 2006, Grain size and grain shape analysis of fault rocks: Tectonophysics, v. 427, no. 1, p. 199-216.

Heldt, M., Lehmann, J., Bachmann, M., Negra, H., and Kuss, J., 2010, Increased terrigenous influx but no drowning: palaeoenvironmental evolution of the Tunisian carbonate platform margin during the Late Aptian: Sedimentology, v. 57, no. 2, p. 695-719.

Hezzi, I., Aïfa, T., Khemiri, F., and Ghanmi, M., 2015, Seismic and well log post-Cretaceous reservoir correlations in the Sahel, east Tunisia: Arabian Journal of Geosciences, p. 1-33.

Hlaiem, A., 1999, Halokinesis and structural evolution of the major features in eastern and southern Tunisian Atlas: Tectonophysics, v. 306, no. 1, p. 79-95.

Hudec, M. R., and Jackson, M. P., 2007, Terra infirma: understanding salt tectonics: Earth-Science Reviews, v. 82, no. 1, p. 1-28.

Huiqi, L., McClay, K., and Powell, D., 1992, Physical models of thrust wedges, Thrust tectonics, Springer, p. 71-81.

Jackson, M., and Talbot, C. J., 1991, A glossary of salt tectonics, Bureau of Economic Geology, University of Texas at Austin.

Jallouli, C., and Mickus, K., 2000, Regional gravity analysis of the crustal structure of Tunisia: Journal of African Earth Sciences, v. 30, no. 1, p. 63-78.

Jamison, W. R., 1987, Geometric analysis of fold development in overthrust terranes: Journal of Structural Geology, v. 9, no. 2, p. 207-219.

Jeanne, P., Guglielmi, Y., Lamarche, J., Cappa, F., and Marié, L., 2012, Architectural characteristics and petrophysical properties evolution of a strike-slip fault zone in a fractured porous carbonate reservoir: Journal of Structural Geology, v. 44, p. 93-109.

Jongsma, D., Woodside, J., King, G., and Van Hinte, J., 1987, The Medina Wrench: a key to the kinematics of the central and eastern Mediterranean over the past 5 Ma: Earth and planetary science letters, v. 82, no. 1, p. 87-106.

Katz, O., Reches, Z., and Roegiers, J.-C., 2000, Evaluation of mechanical rock properties using a Schmidt Hammer: International Journal of Rock Mechanics and Mining Sciences, v. 37, no. 4, p. 723-728.

Khomsi, S., Bédir, M., Soussi, M., Ben Jemia, M. G., and Ben Ismail-Lattrache, K., 2006, Mise en évidence en subsurface d'événements compressifs Éocène moyen–supérieur en Tunisie orientale (Sahel): généralité de la phase atlasique en Afrique du Nord: Comptes Rendus Geoscience, v. 338, no. 1, p. 41-49.

Khomsi, S., Ben Jemia, M. G., de Lamotte, D. F., Maherssi, C., Echihi, O., and Mezni, R., 2009, An overview of the Late Cretaceous–Eocene positive inversions and Oligo-Miocene subsidence events in the foreland of the Tunisian Atlas: Structural style and implications for the tectonic agenda of the Maghrebian Atlas system: Tectonophysics, v. 475, no. 1, p. 38-58.

Khomsi, S., Echihi, O., and Slimani, N., 2012, Structural control on the deep hydrogeological and geothermal aquifers related to the fractured Campanian-Miocene reservoirs of north-eastern Tunisia foreland constrained by subsurface data: Comptes Rendus Geoscience, v. 344, no. 3, p. 247-265.

Klett, T. R., 2001, Total Petroleum Systems of the Pelagian Province, Tunisia, Libya, Italy, and Malta--the Bou Dabbous-Tertiary and Jurassic-Cretaceous Composite, US Department of the Interior, US Geological Survey.

Knipe, R., Fisher, Q., Jones, G., Clennell, M., Farmer, A., Harrison, A., Kidd, B., McAllister, E., Porter, J., and White, E., 1997, Fault seal analysis: successful methodologies, application and future directions: Norwegian Petroleum Society Special Publications, v. 7, p. 15-38.

Law, R. D., Eriksson, K., and Davisson, C., 2001, Formation, evolution, and inversion of the middle Tertiary Diligencia basin, Orocopia Mountains, southern California: Geological Society of America Bulletin, v. 113, no. 2, p. 196-221.

Lønøy, B., 2015, Reservoir characterization of Aptian carbonates; Jebel Fadeloun and Jebel Garci, Tunisia: M. Sc. Thesis, University of Bergen, Bergen.

McClay, K., 1995, The geometries and kinematics of inverted fault systems: a review of analogue model studies: Geological Society, London, Special Publications, v. 88, no. 1, p. 97-118.

McClay, K., 2011, Introduction to thrust fault-related folding, *in* McClay, K., Shaw, J.H.,, and Suppe, J., eds., Thrust-fault Related Folding, Volume 94, AAPG Mem, p. 1-19.

McClay, K., Whitehouse, P., Dooley, T., and Richards, M., 2004, 3D evolution of fold and thrust belts formed by oblique convergence: Marine and Petroleum Geology, v. 21, no. 7, p. 857-877.

McClay, K. R., 1992, Thrust tectonics, London, Chapman & Hall.

McClay, K. R., 2004, Thrust Tectonics and Hydrocarbon Systems: AAPG Memoir 82, AAPG, v. 82.

Mejri, F., Burollet, P., and Ben Ferjani, A., 2006, Petroleum geology of Tunisia, a renewed synthesis: Entrep Tunis Activ Petrol, Mem, no. 22, p. 233.

Micarelli, L., Benedicto, A., and Wibberley, C. A. J., 2006, Structural evolution and permeability of normal fault zones in highly porous carbonate rocks: Journal of Structural Geology, v. 28, no. 7, p. 1214-1227.

Mitra, S., 1986, Duplex structures and imbricate thrust systems: geometry, structural position, and hydrocarbon potential: AAPG Bulletin, v. 70, no. 9, p. 1087-1112.

Mitra, S., 1990, Fault-propagation folds: geometry, kinematic evolution, and hydrocarbon Traps (1): AAPG Bulletin, v. 74, no. 6, p. 921-945.

Mitra, S., 2002, Structural models of faulted detachment folds: AAPG bulletin, v. 86, no. 9, p. 1673-1694.

Mitra, S., 2003, A unified kinematic model for the evolution of detachment folds: Journal of Structural Geology, v. 25, no. 10, p. 1659-1673.

Morris, A. P., Ferrill, D. A., and McGinnis, R. N., 2009, Mechanical stratigraphy and faulting in Cretaceous carbonates: AAPG bulletin, v. 93, no. 11, p. 1459-1470.

Moustafa, A. R., 2013, Fold-related faults in the Syrian Arc belt of northern Egypt: Marine and Petroleum Geology, v. 48, no. 0, p. 441-454.

Nixon, C. W., 2013, Analysis of fault networks and conjugate systems: Ph. D. Thesis, University of southampton.

Patriat, M., Ellouz, N., Dey, Z., Gaulier, J.-M., and Kilani, H. B., 2003, The Hammamet, Gabes and Chotts basins (Tunisia): a review of the subsidence history: Sedimentary geology, v. 156, no. 1, p. 241-262.

Peacock, D., and Sanderson, D., 1995, Pull-aparts, shear fractures and pressure solution: Tectonophysics, v. 241, no. 1, p. 1-13.

Poblet, J., and Lisle, R. J., 2011, Kinematic evolution and structural styles of fold-and-thrust belts: Geological Society, London, Special Publications, v. 349, no. 1, p. 1-24.

Pollard, D. D., and Aydin, A., 1988, Progress in understanding jointing over the past century: Geological Society of America Bulletin, v. 100, no. 8, p. 1181-1204.

Price, N. J., 1966, *in* Price, N. J., ed., Fault and Joint Development in Brittle and Semi-Brittle Rock, Pergamon, p. 1-56.

Price, N. J., and Cosgrove, J. W., 1990, Analysis of geological structures, Cambridge University Press.

Rabhi, M. a. M., R., 2003, Sidi Bou Ali: Service Géologique de Tunisie, scale 1:50000.

Railsback, L. B., 1993, Lithologic controls on morphology of pressure-dissolution surfaces (stylolites and dissolution seams) in Paleozoic carbonate rocks from the mideastern United States: Journal of Sedimentary Research, v. 63, no. 3.

Ramsay, J. G., and Huber, M. I., 1987, The Techniques of Modern Structural Geology: Folds and fractures, Academic Press.

Rowan, M. G., 1997, Three-dimensional geometry and evolution of a segmented detachment fold, Mississippi Fan foldbelt, Gulf of Mexico: Journal of Structural Geology, v. 19, no. 3, p. 463-480.

Saadi, J., 1990, Exemple de sédimentation syntectonique au Crétacé inférieur le long d'une zone de décrochement NS.: les structures d'Enfidha (Tunisie nord-orientale): Géodynamique, v. 5, no. 1, p. 17-33.

Salomon-Mora, L. E., Aranda-Garcia, M., and Roman-Ramos, J. R., 2009, Contractional growth faulting in the Mexican Ridges, Gulf of Mexico, *in* Bartolini, C., Román Ramos, J.R. , ed., Petroleum Systems in the Southern Gulf of Mexico, AAPG Mem., p. 93-115.

Sanderson, D. J., and Nixon, C. W., 2015, The use of topology in fracture network characterization: Journal of Structural Geology, v. 72, p. 55-66.

Schlumberger. 2007. Carbonate Reservoirs - Meeting unique challenges to maximize recovery [Online]. Available: http://www.slb.com/~/media/Files/industry_challenges/carbonates/brochures/cb_carbonate_reservoirs_07os003.pdf [Accessed 5 March 2015].

Scisciani, V., 2009, Styles of positive inversion tectonics in the Central Apennines and in the Adriatic foreland: Implications for the evolution of the Apennine chain (Italy): Journal of Structural Geology, v. 31, no. 11, p. 1276-1294.

Shipton, Z., and Cowie, P., 2001, Damage zone and slip-surface evolution over μm to km scales in high-porosity Navajo sandstone, Utah: Journal of Structural Geology, v. 23, no. 12, p. 1825-1844.

Sibson, R., 1977, Fault rocks and fault mechanisms: Journal of the Geological Society, v. 133, no. 3, p. 191-213.

Sibson, R. H., 1986, Brecciation processes in fault zones: inferences from earthquake rupturing: Pure and Applied Geophysics, v. 124, no. 1-2, p. 159-175.

Sibson, R. H., 2000, Fluid involvement in normal faulting: Journal of Geodynamics, v. 29, no. 3, p. 469-499.

Suppe, J., 1983, Geometry and kinematics of fault-bend folding: American Journal of science, no. 283, p. 684-721.

Suppe, J., and Medwedeff, D. A., 1990, Geometry and kinematics of fault-propagation folding: Eclogae Geologicae Helvetiae, v. 83, no. 3, p. 409-454.

Turner, J. P., and Williams, G. A., 2004, Sedimentary basin inversion and intra-plate shortening: Earth-Science Reviews, v. 65, no. 3, p. 277-304.

Underwood, C. A., Cooke, M. L., Simo, J. A., and Muldoon, M. A., 2003, Stratigraphic controls on vertical fracture patterns in Silurian dolomite, northeastern Wisconsin: AAPG bulletin, v. 87, no. 1, p. 121-142.

Van der Pluijm, B. A., and Marshak, S., 2004, Earth structure: an introduction to structural geology and tectonics, New York: WW Norton; 2nd ed.

Wennberg, O., Azizzadeh, M., Aqrawi, A., Blanc, E., Brockbank, P., Lyslo, K., Pickard, N., Salem, L., and Svana, T., 2007, The Khaviz Anticline: an outcrop analogue to giant fractured Asmari Formation reservoirs in SW Iran, *in* Lonergan, L., Jolly, R.J.H., Sanderson, D.J. & Rawnsley, K. , ed., Fractured Reservoirs, Geological Society of London.

Wennberg, O., Svånå, T., Azizzadeh, M., Aqrawi, A., Brockbank, P., Lyslo, K., and Ogilvie, S., 2006, Fracture intensity vs. mechanical stratigraphy in platform top carbonates: the Aquitanian of the Asmari Formation, Khaviz Anticline, Zagros, SW Iran: Petroleum Geoscience, v. 12, no. 3, p. 235-246.

Wibberley, C. A., and Shipton, Z. K., 2010, Fault zones: A complex issue: Journal of Structural Geology, v. 32, no. 11, p. 1554-1556.

Wilcox, R. E., Harding, T. t., and Seely, D., 1973, Basic wrench tectonics: AAPG Bulletin, v. 57, no. 1, p. 74-96.

Williams, G., Powell, C., and Cooper, M., 1989, Geometry and kinematics of inversion tectonics: Geological Society, London, Special Publications, v. 44, no. 1, p. 3-15.

Woodcock, N., Dickson, J., and Tarasewicz, J., 2007, Transient permeability and reseal hardening in fault zones: evidence from dilation breccia textures: Geological Society, London, Special Publications, v. 270, no. 1, p. 43-53.

Woodcock, N., and Schubert, C., 1994, Continental strike-slip tectonics, *in* Hancock, P. L., ed., Continental deformation: Oxford, Pergamon Press, p. 251-263.

Woodcock, N. H., and Fischer, M., 1986, Strike-slip duplexes: Journal of structural geology, v. 8, no. 7, p. 725-735.

Woodcock, N. H., and Rickards, B., 2003, Transpressive duplex and flower structure: Dent fault system, NW England: Journal of Structural Geology, v. 25, no. 12, p. 1981-1992.

Wright, V., 1992, A revised classification of limestones: Sedimentary Geology, v. 76, no. 3, p. 177-185.

Yamaji, A., Tomita, S., and Otsubo, M., 2005, Bedding tilt test for paleostress analysis: Journal of structural geology, v. 27, no. 1, p. 161-170.

Zouaghi, T., Zargouni, F., Lazzez, M., Youssef, M. B., Inoubli, M. H., Bédir, M., and Guellala, R., 2011, The Chotts fold belt of Southern Tunisia, North African margin: structural pattern, evolution, and regional geodynamic implications, *in* Schattner, U., ed., New Frontiers in Tectonic Research—At the Midst of Plate Convergence, INTECH Open Access Publisher.

APPENDIX

Appendix I: Seismic section (Line 12.15)

Appendix II: Thin section images

Appendix III: Fracture data

Appendix I

Seismic section (Line 12.15):

UTM coordinates (Zone 32 S):

Start: 594044E 399321N

End: 615825E 399217N

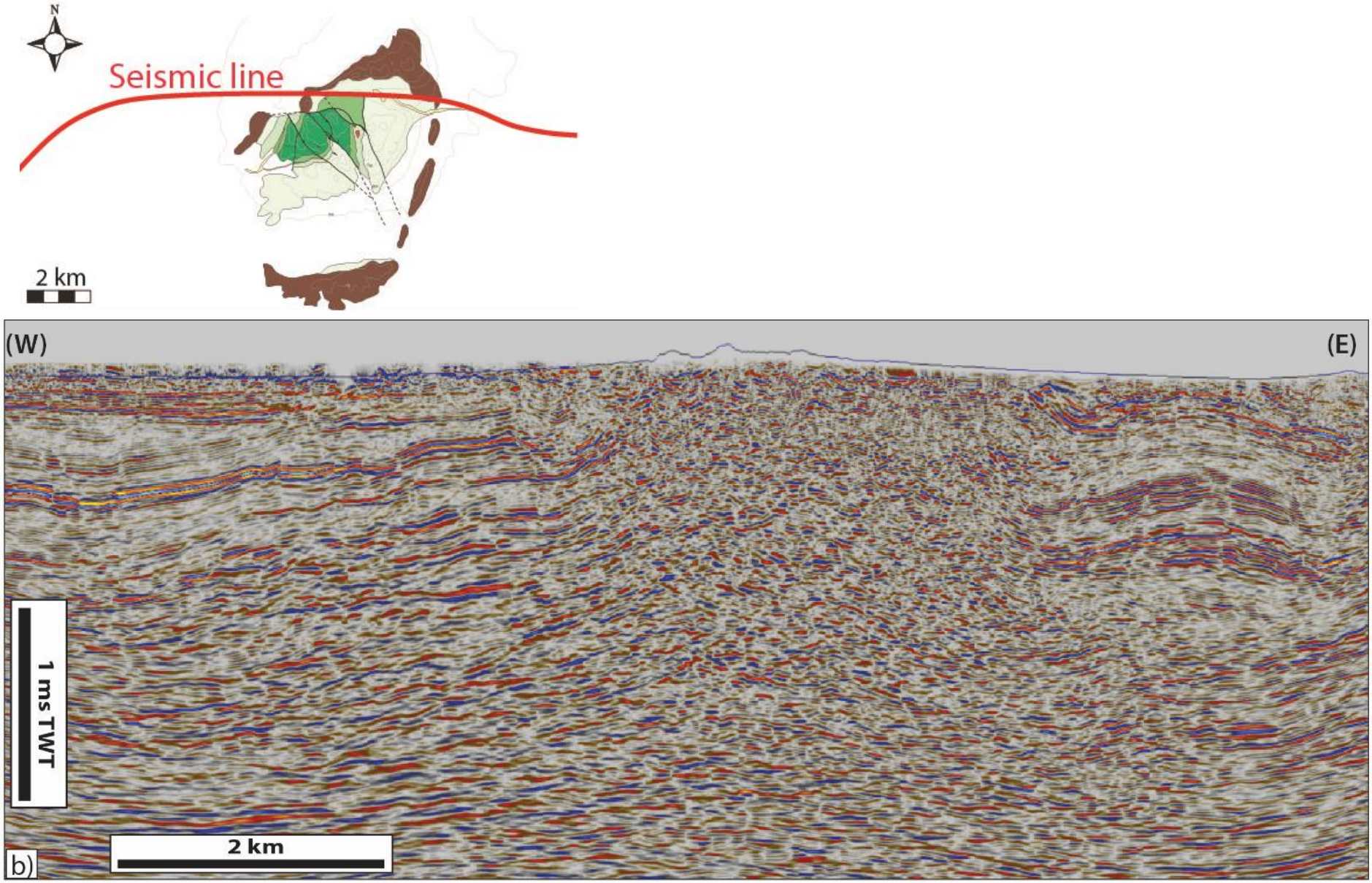
N
Seismic line
2 km
(W)
(E)
1 ms TWT
2 km
b)

Appendix II

Thin section images of fault rocks:

A1.1 - Core - Proto breccia

A1.2 - Core - Breccia

A1.3 - Core - Protobreccia

A1.6 - Core - Fault Vein / Breccia

A1.4a - Footwall Damage Zone - Stylobreccia

A1.7 - Footwall Damage Zone - Hydraulic breccia

A1.8 - Footwall Damage Zone - Hydr. Host rock

A1.4b - Footwall Host Rock - Undeformed

A1.5a - Hangingwall Damage Zone - Protobreccia

A1.5b - Hangingwall Host Rock - Undeformed

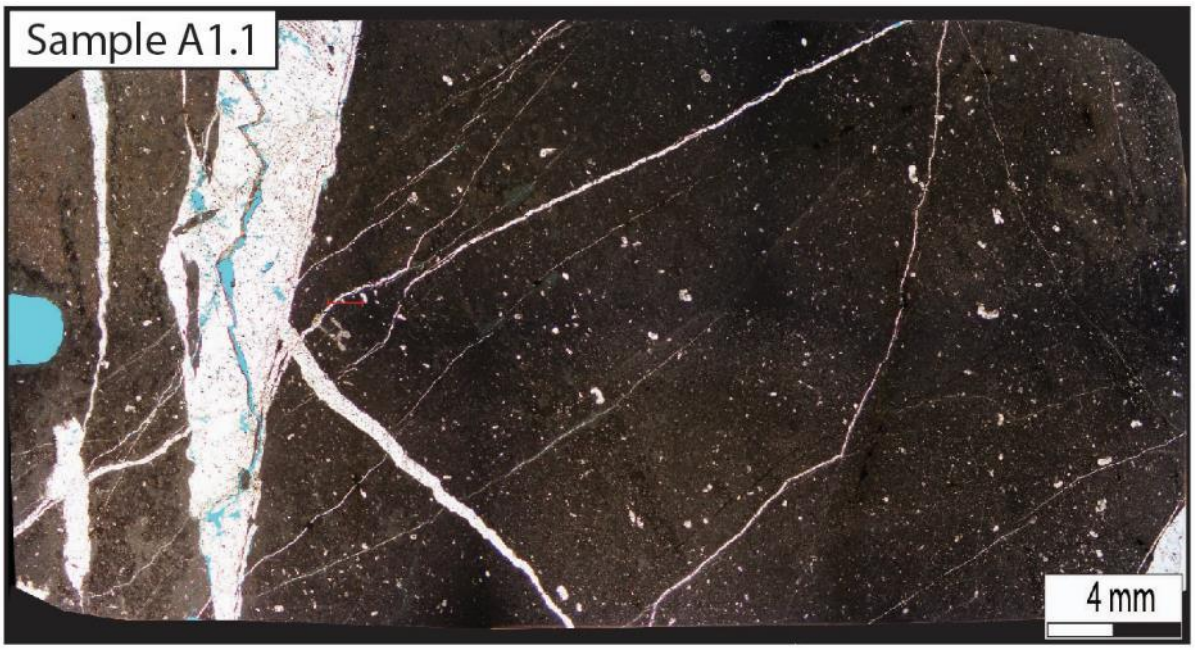
Sample A1.1
4 mm

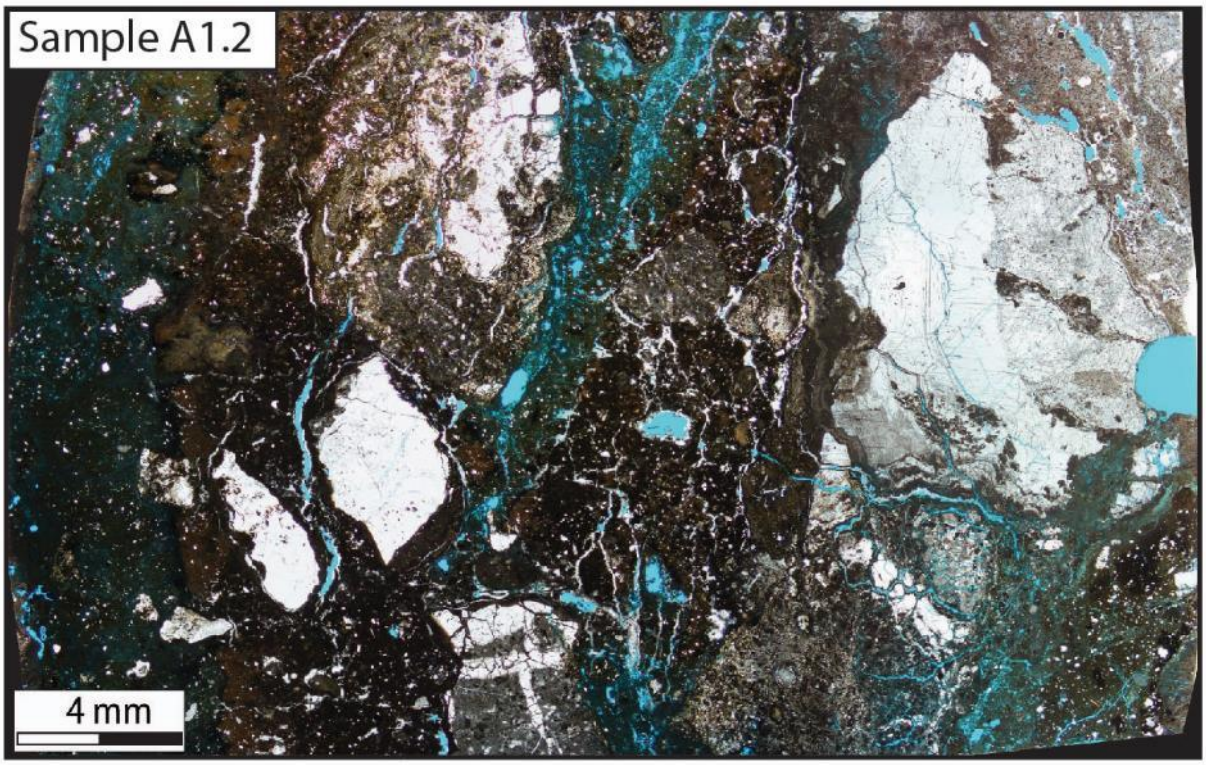
Sample A1.2
4 mm

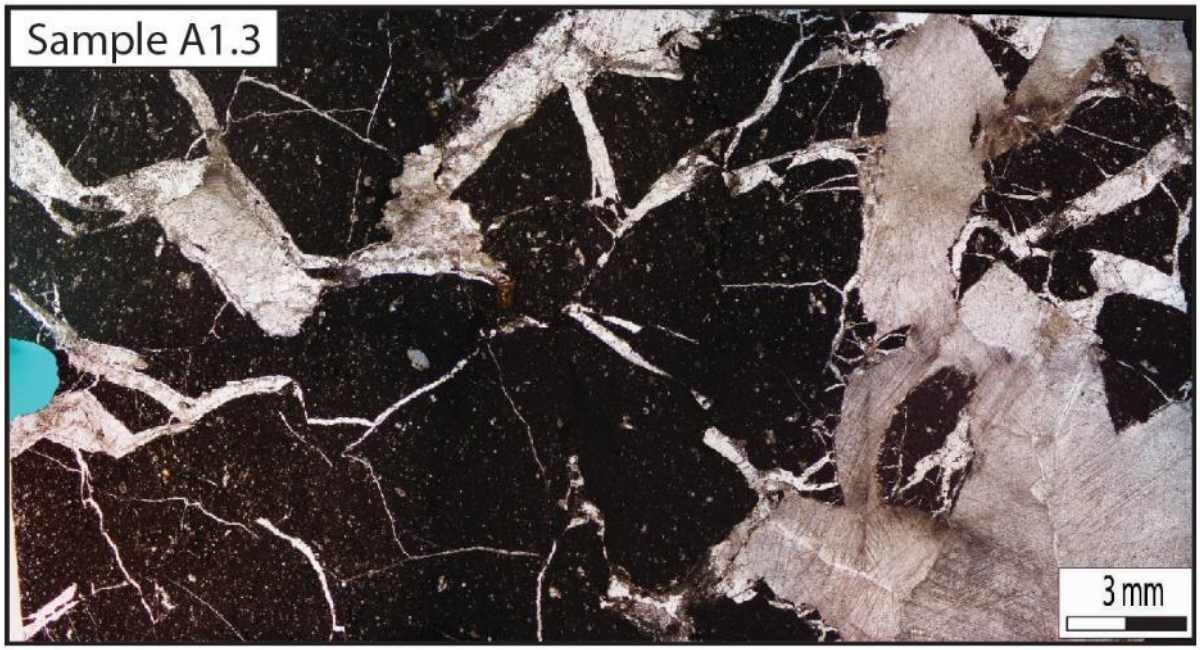
Sample A1.3
3 mm

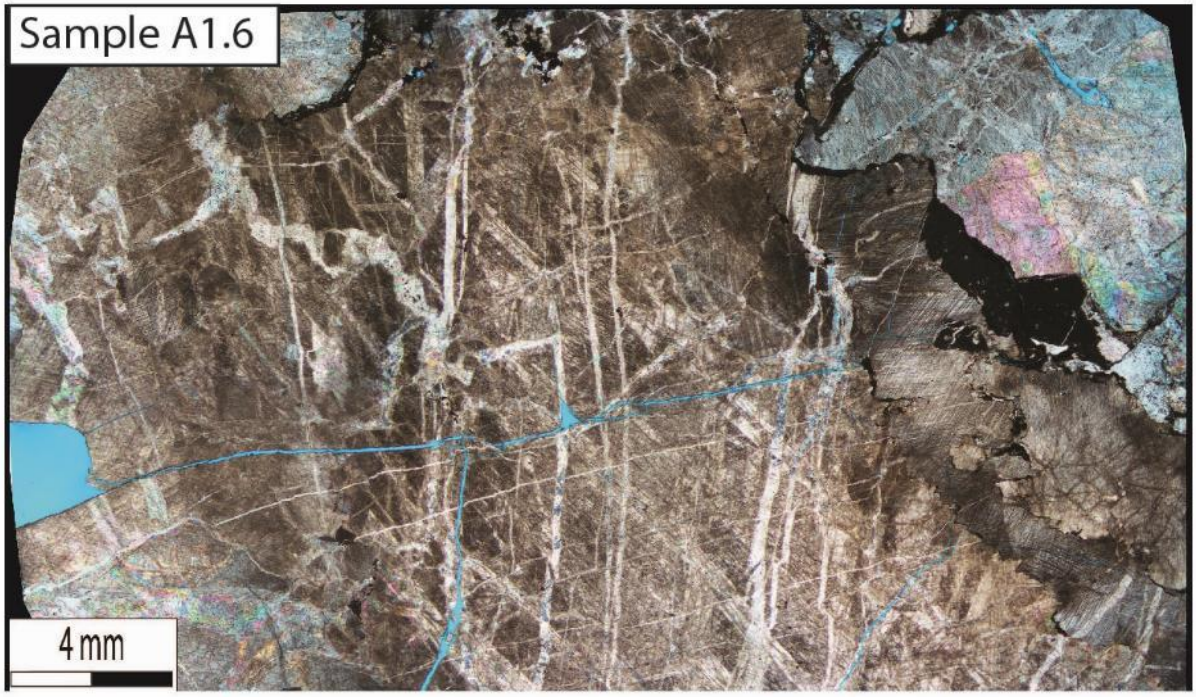
Sample A1.6
4 mm

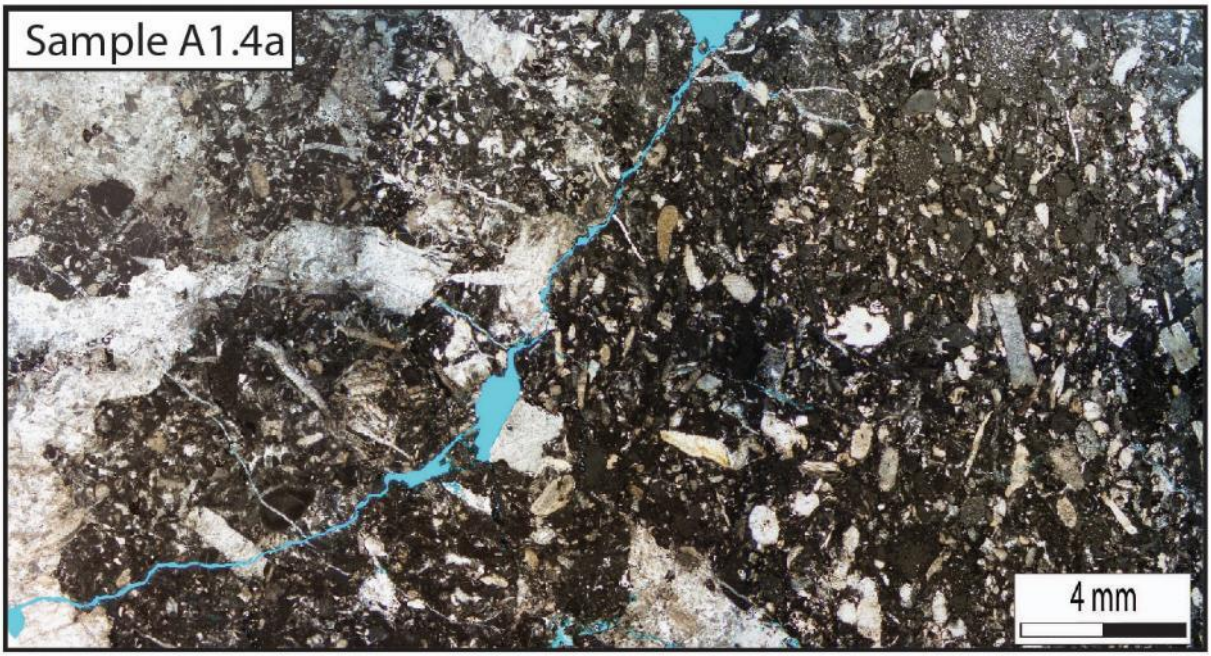
Sample A1.4a
4 mm

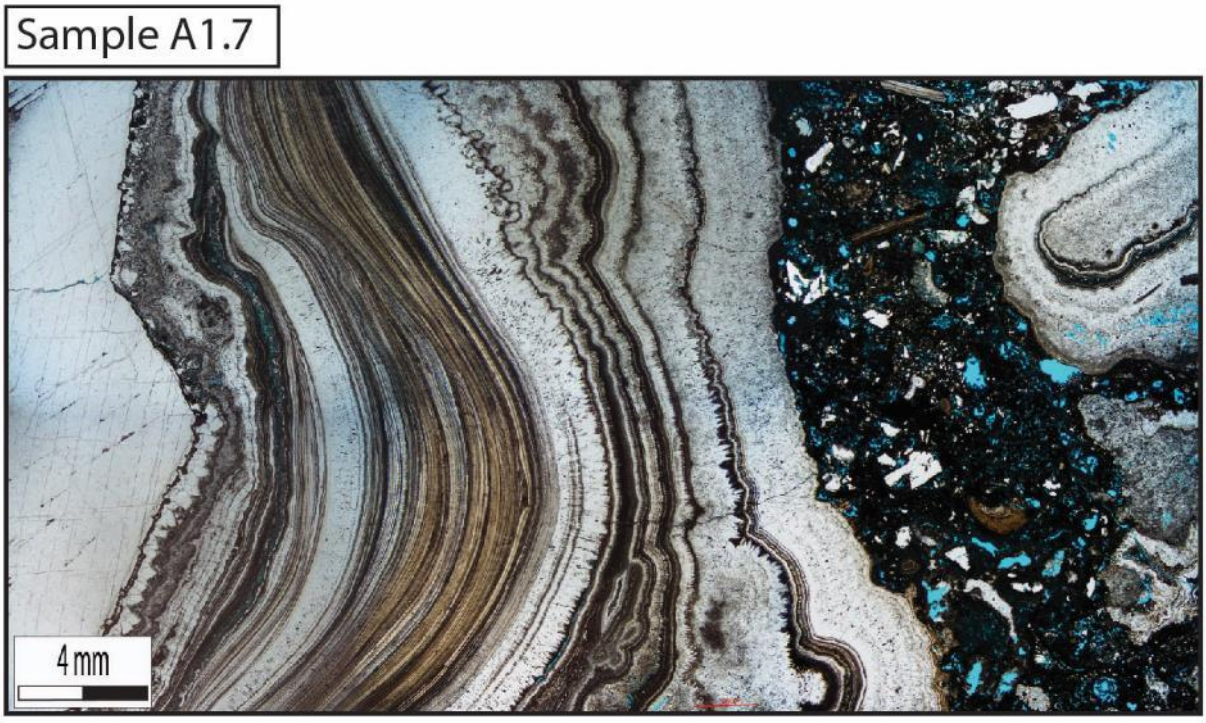
Sample A1.7
4 mm

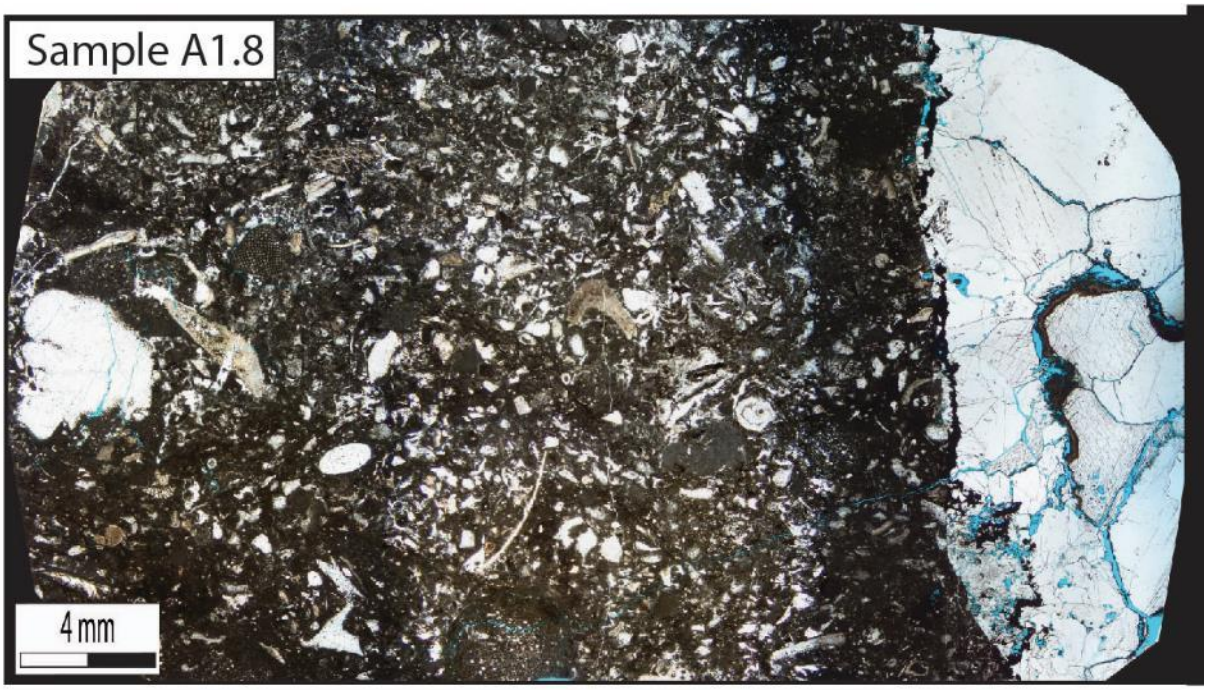
Sample A1.8
4 mm

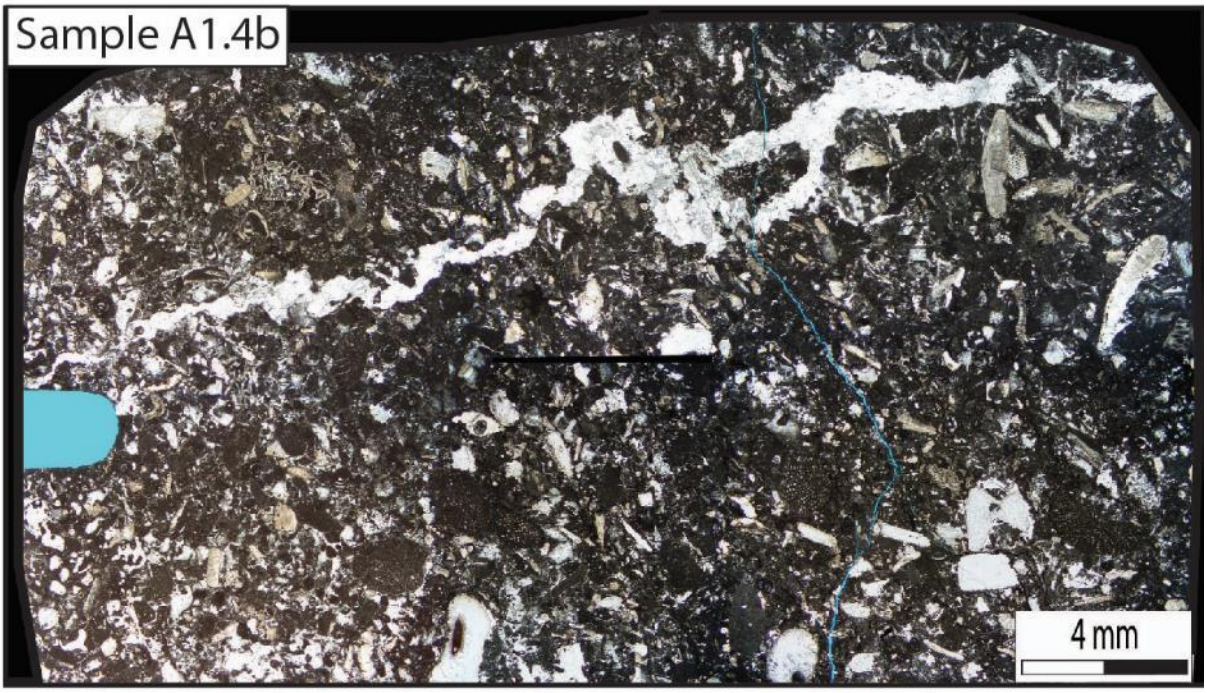
Sample A1.4b
4 mm

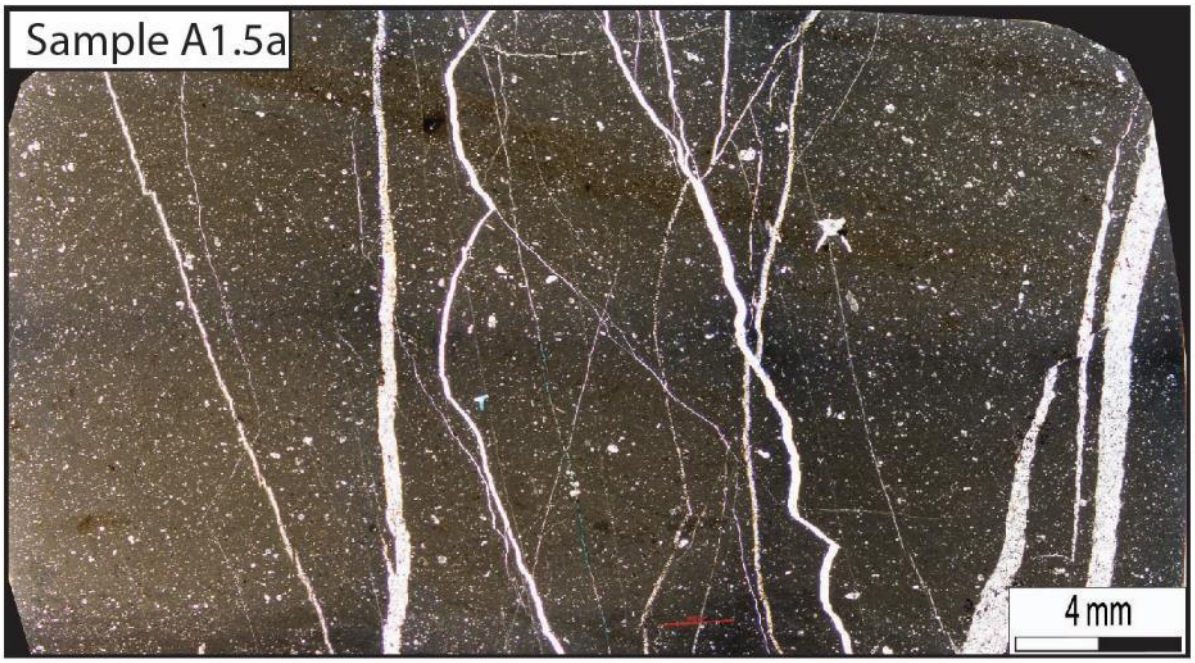
Sample A1.5a
4 mm

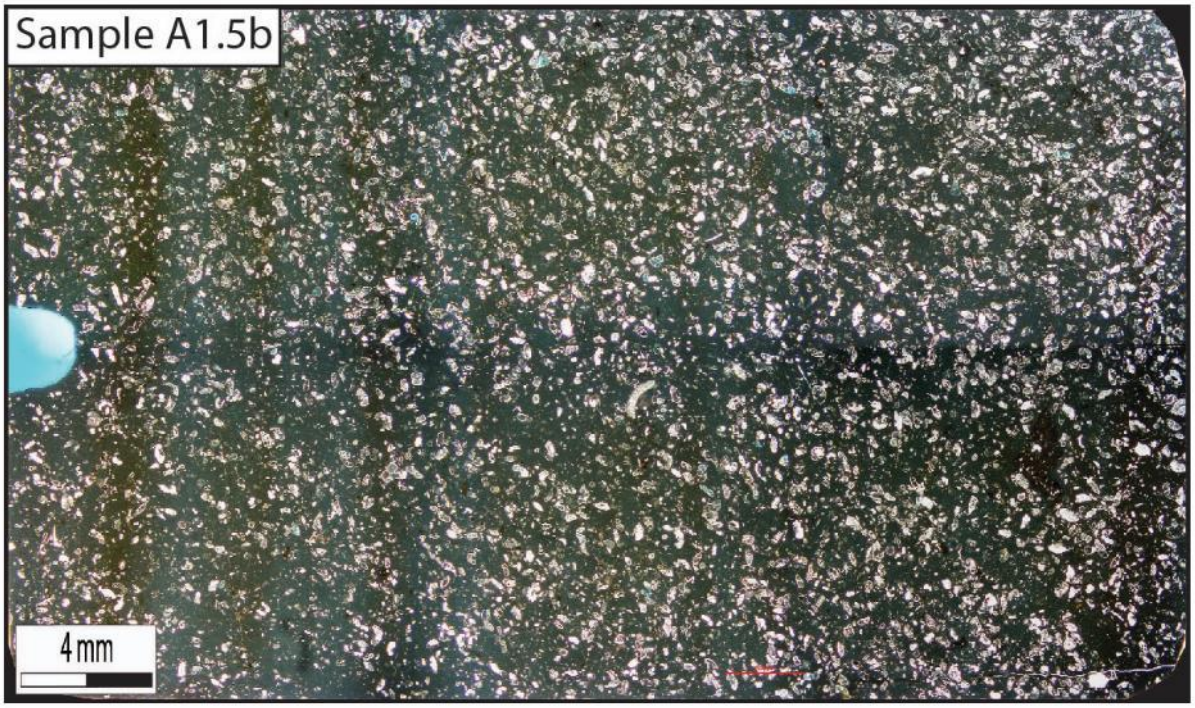
Sample A1.5b
4 mm

Appendix III

Fracture data:

Table A - Fracture data from locality Charlie (mechanical layering)

Table B.1-2 - Fracture data from locality Delta (backgr. fracturing)

Table C - Microfracture data from thin section analyses

Table A - Summary of fracture data from scanlines C1 to C9 at locality "Charlie"

Scanline	Texture	Thickness (cm)	Fracture intensity	Fracture frequency	Bed bound	Internal	Cross cutting	Fracture aperture (mm) Max	Fracture aperture (mm) Min	Fracture length (cm) Max	Fracture length (cm) Min	Dominating orientation (trend/dip) 1.	Dominating orientation (trend/dip) 2.
C1	Mud	42	21	5	8	9	4	8	1	42	7	NW-SE/73	NE-SW/86
C2	Wack	25	15	4	5	1	8	8	1	>100	3	N-S/78	NW-SE/70
C3	Wack	83	31	8	8	17	5	20	2	36	4	NW-SE/83	NE-SW/80
C4	Wack	40	19	5	13	1	4	40	1	>100	4	NE-SW/70	NW-SE/90
C5	Wack	41	27	7	7	16	4	20	1	40	7	NW-SE/70	N-S/86
C6	Wack	30	19	5	8	4	7	30	4	>100	14	NW-SE/80	N-S/82
C7	Mud	47	20	5	8	8	4	15	1	>100	8	N-S/86	E-W/80
C8	Wack	73	36	9	17	15	4	22	2	40	5	N-S/82	NE-SW/80
C9	Pack	167	12	3	0	9	3	10	1	>100	20	N-S/78	NW-SE/90

Table B.1 - Fracture data from scanline D1 at locality "Delta"

Fracture set	Distance along scanline (cm)	Orienation (trend/dip)	Fracture spacing (cm)	Fracture aperture (cm)	Fracture length (cm)
S1	0	316/84	104	9	95
S1	104	326/82	120	20	>>100
S1	224	150/78	30	6	80
S1	254	138/80	18	7	85
S1	272	334/70	240	8	>>100
S1	512	319/85	80	10	>>100
S1	592	134/75	120	2	46

Table B.2 - Fracture data from scanline D2 at locality "Delta"

Fracture set	Distance along scanline (cm)	Orienation (trend/dip)	Fracture spacing (cm)	Fracture aperture (cm)	Fracture length (cm)
S2	0	048/86	90	14	>100
S2	90	010/70	70	11	>100
S2	160	046/90	250	16	68
S2	410	064/90	76	5	73
S2	486	052/82	24	8	30
S2	510	063/86	151	25	>>100
S2	661	062/88	18	22	>100
S2	679	052/76	88	30	>100
S2	767	020/90	80	34	>>100
S2	847	034/80	45	5	62

Table C - Thin section analyses - fracture characterization

Sample	Structural domain	Fracture types	Fracture morphology	Fracture orientations	Fracture generations	Fracture frequency (per 10 mm)	Fill properties
A1.1	Fault core	Shear and tension fractures. Pressure solution seams	Straigth to curved fractures, overstepping and branching, sharp-edged (cutting particles) fractures. Solution enlarged and reduced fractures. Irregular seams (stylolites)	Sub-perpendicular fractures, sub-parallel microfactures,	≥2	6.8	Fill variations (sparite and micrite), crystal twinning
A1.2	Fault core	Shear and tension fractures.	Largely curved and branching fractures, crumbly (breaking around objects) to sharp-edged. Intraclast veins. Solution enlarged and reduced voids	Scattered orientations	≥3	5.6	Fill variations (sparite and micrite), fibrous cement-growth along fracture margins, local layered infill, cryptocrystalline zones, abundant recrystallization, twinning
A1.3	Fault core	Shear and tensile fracture. Pressure solution seams	Straight to curved fractures with kinks. Branching microfractures. Irregular stylolitic seams associated with grain boundaries	Scattered orientations	≥2	12.2	Fill variations (hematite, sparite and micrite), calcite twinning,
A1.6	Fault core	Shear and tensile fractures. Pressure solution seams	Complex and intense fracture network. Predominantly, straight and sharp-edged fractures and microfractures. Intraclast veins. Stylolitic seams around crystal margins	Sub-orthogonal to oblique	≥3	7.5	90 % of sample consists of coarse and deformed sparite crystals. Twinning and rhombohedral cleavage
B2.3	Intensely deformed damage zone	Shear and tensile fractures. Pressure solution seams	Kinked to curved, solution enlarged fractures with inclusions. Branching microfractures. Irregular stylolitic seams associated with fragment boundaries	Sub-parallel, oblique to irregular	≥2	4.5	Sparite and micrite fill
A1.4a	Footwall damage zone	Shear and tensile fracture. Pressure solution seams	Large, irregular vein. Straigth to curved, sharp-edged microfractures. Intraclast veins. Zones of stylolite-bound fragments	Sub-parallel	≥3	2.8	Sparite (fractures) and micrite (stylolites)
A1.5a	Hanging wall damage zone	Shear and tensile	Straigth, curved and kinked fractures. Branching, sharp-edged and en échelon arranged microfractures.	Sub-parallel to conjugative, rare orthogonal intersections	≥2	7.6	Sparite, locally contaminated with black stains
B2.1	Footwall damage zone	Shear and tensile fractures. Pressure solution seams	Straight to curved microfractures, zone irregular microfractures and associated grain-size reduction. Zone of stylolite-bound fragments	Sub-parallel to irregular	≥1	2.9	Sparite and micrite fill
A1.7	Footwall damage zone	Shear fracture	Isolated and sharp-edged microfractures	N/A	≥1	1.0	Laminated to fiberous calcite, sparite and micrite. Cryptocrystalline "breccia" matrix
A1.8	Footwall damage zone	Shear and tensile fractures. Pressure solution seams	Kinked to curved microfractures. Solution enlarged and reduced fractures. Zones of stylolite-bound fragments	Sub-parallel to irregular	≥2	2.7	Sparite and micrite fill. crystal twinning
A1.4b	Footwall host rock	Tensile	Single, solution-enlarged fracture with irregular shape. Single, curved and sharp-edged microfracture. Stylolitic seams around grains	N/A	≥2	1.5	Sparite (fractures) and micrite (stylolites)
A1.5b	Hanging wall host rock	Tensile. Pressure solution seams	Two isolated microfractures, sharp-edged. Rare stylolitic seams	Sub-orthogonal	≥1	0.5	Sparite and micritic matrix